DEEP WATER EXCHANGE IN FORTUNE BAY, NEWFOUNDLAND

CENTRE FOR NEWFOUNDLAND STUDIES

TOTAL OF 10 PAGES ONLY
MAY BE XEROXED

(Without Author's Permission)

BRADLEY STEPHEN DE YOUNG

C07651


CENTRE FOR NFLD. STUDIES
NOV 8 1986
MEMORIAL UNIVERSITY
OF NEWFOUNDLAND


MEMORIAL UNIVERSITY
PERIODICALS
NOV 6 1986
DIVISION
OF NEWFOUNDLAND

DEEP WATER EXCHANGE IN FORTUNE BAY, NEWFOUNDLAND

by

© Bradley de Young, B.Sc.

A Thesis submitted in partial fulfillment

of the requirements for the degree of

Master of Science

Department of Physics

Memorial University of Newfoundland

September 1983

St. John's Newfoundland

ABSTRACT

Temperature, salinity and density data are presented showing a seasonal cycle in the deep water in Fortune Bay, Newfoundland. Cold Labrador Current Water flows in from Saint-Pierre Channel, an extension of the Avalon Channel, in the summer. Warm Modified Slope Water flows in from Hermitage Channel in the winter.

A description of the water structure in the Fortune Bay area for 1981 and 1982 is presented. The transport of the Labrador Current in the Saint-Pierre Channel is determined to be 6.4×10^4 m^3 s^{-1}. Cold water exchange in the summer is found to be correlated with a seasonal variation in the Labrador Current flow. Direct current meter measurements of this density current inflow are provided with an analytical discussion of the interaction between the flow and the tide.

Warm water exchange in the winter is found to be correlated with a seasonal shift in the wind stress. Light southwesterly summer winds are replaced in winter by strong northeasterly winds. Two possible mechanisms by which the wind can generate the Modified Slope Water inflow are put forward: a time-dependent upwelling model and a steady-state upwelling model.

ACKNOWLEDGEMENTS

Many people contributed to this work and it is a pleasure to acknowledge their contribution. I would like to thank my supervisor Dr. A.E. Hay for his effort and guidance throughout this project. E. Dalley of the Northwest Atlantic Fisheries Center generously provided BT and CTD data for analysis. The captains and crews of the following vessels contributed to the completion of this work: CSS DAWSON, CGS SHAMOOK, CGS MARINUS and CGS PANDORA II. A large number of people were involved in the collection of the data and provided generously of their time; Dr. W.W. Denner, J. Foley, Dr. G. Gardner. Dr. R. Haedrich, Dr. A.E. Hay, D. Kinsella and A. Walsh. D. Alteen, J. Dodge and J. Foley wrote most of the software for the CTD analysis. S. Akenhead assisted in analysing the bottle data and data from Station 27. Drs. C. Garrett and R. Fournier provided useful discussions. M. Angel, R. Guest and G. Campbell assisted in the drafting of the figures. Garfield and Angel were of great assistance in typing this work. The study was funded by NSERC Operating Grant A8446 and a Fisheries and Oceans Subvention grant to Dr. A.E. Hay.

TABLE OF CONTENTS

ABSTRACT	ii
ACKNOWLEDGEMENTS	iii
TABLE OF CONTENTS	iv
LIST OF FIGURES	vi
LIST OF TABLES	viii
CHAPTER 1 INTRODUCTION	
1.1 Prologue	1
1.2 Deep water exchange in fjords	1
1.3 Study area	4
1.4 Freshwater runoff	7
1.5 Regional oceanography	8
1.6 Oceanography of the Fortune Bay area	10
CHAPTER 2 FIELD PROGRAM AND DATA ANALYSIS	
2.1 Station plan	14
2.2 BT and CTD data	15
2.3 Current meter moorings	17
2.4 Dissolved oxygen and nutrients	22
2.5 Data reduction and analysis	22
CHAPTER 3 LONG TERM DATA	
3.1 Channels adjacent to Fortune Bay	24
3.2 Seasonal variations in Fortune Bay	26
3.3 Seasonal variations in the wind field	28
CHAPTER 4 OCEANOGRAPHY OF FORTUNE BAY AND ADJACENT CHANNELS	
4.1 Circulation in Hermitage Channel	35
4.2 Saint-Pierre Channel	39
4.3 Fortune Bay	40
CHAPTER 5 DENSITY CURRENT INFLOW	
5.1 Review	70
5.2 Observations	71
5.3 Theory	79
5.4 Entrainment	85
5.5 Comparison of theory and observation	86
5.6 Labrador Current transport	88
CHAPTER 6 MIQUELON SILL FLOW	
6.1 Moorings	91
6.2 Thermistor chain and current meter data	91
CHAPTER 7 UPWELLING IN HERMITAGE CHANNEL	
7.1 Introduction	98
7.2 Time-dependent upwelling	98
7.3 Steady state upwelling	102
7.4 Application to Hermitage Channel	104

CHAPTER 8 SUMMARY AND CONCLUSIONS 107

REFERENCES 109
APPENDIX I 112
APPENDIX II 116
APPENDIX III 144

LIST OF FIGURES

1.1	Location map showing the south coast area	2
1.2	Detailed map of the area	5
1.3	Area map with station locations	11
1.4	Transect in Fortune Bay, December 1981	13
2.1	Current meter mooring M1	19
2.2	Current meter mooring M2	20
2.3	Current meter mooring M3	21
3.1	Long term temperature in the bay	27
3.2	Offshore and longshore pressure differences	31
3.3	Offshore and longshore wind stress	33
4.1	Transect in Laurentian and Hermitage channels, May 1982	48
4.2	Transect in mouth of Hermitage Channel, May 1982	49
4.3	Transect in Hermitage Channel, stations 39-42, May 1982	50
4.4	Dynamic height in Hermitage Channel, May 1982	51
4.5	Transect across Saint-Pierre Channel, May 1982	52
4.6	Transect along Saint-Pierre Channel, May 1982	53
4.7	Transect from Saint-Pierre to Hermitage Channel, December 1981	54
4.8	Transect across Sagona sill, December 1981	55
4.9	Transect across Miquelon sill, February 1982	56
4.10	Transect from Saint-Pierre to Hermitage Channel, May 1982	57
4.11	Transect along Fortune Bay, May 1982	58
4.12	Transect across Sagona sill, May 1982	59
4.13	Nutrient transect from Saint-Pierre to Hermitage Channel, May 1982	60
4.14	Nutrient transects in Hermitage Channel and Fortune Bay, May 1982	61
4.15	Transect along Fortune Bay, June 1982	62
4.16	Transect from Saint-Pierre to Hermitage Channel, June 1982	63
4.17	Transect across T1 looking up the bay, 7 June 1982	64
4.18	Transect across T1 looking up the bay, 14 June 1982	65
4.19	Transect along Fortune Bay, 12 July 1982	66
4.20	Transect from Saint-Pierre to Hermitage Channel, November 1982	67
4.21	Transect along Fortune Bay, November 1982	68
4.22	Transect across Sagona sill, November 1982	69
5.1	Current meter data from mooring 3, 5-13 June 1982	72
5.2	Rotated current meter data from mooring 3, 5-13 June 1982	74
5.3	CTD plot at station 9 on 9 June 1982	75
5.4	Transect along T2 looking into the bay, 5 June 1982	77
5.5	Transect along T2 looking into the bay, 9 June 1982	78
5.6	Density current inflow schematic	81
5.7	T-S plot of inflow, bay and resultant water	89
6.1	Thermistor chain contour plots for moorings 1 and 2, 6-12 May 1982	92
6.2	Stick diagrams for moorings 1 and 2, 6-12 May 1982	94
6.3	Wind at Saint-Pierre, 6-12 May 1982	97
7.1	Schematic and coordinate system for upwelling analysis	106
A2.1	Salinity from Saint-Pierre to Hermitage Channel, December 1981	117
A2.2	Salinity across Sagona sill, December 1981	118
A2.3	Salinity across Miquelon sill, February 1982	119
A2.4	Salinity along Hermitage Channel, May 1982	120
A2.5	Cross Hermitage Channel stations 47-53, May 1982	121
A2.6	Cross Hermitage Channel stations 43-46, May 1982	122
A2.7	Salinity along Fortune Bay, May 1982	123

A2.8 Salinity across Sagona sill, May 1982 124
A2.9 Salinity from Saint-Pierre to Hermitage Channel, May 1982 125
A2.10 Salinity in Saint-Pierre cross section, May 1982 126
A2.11 Salinity along transect T2, 13 May 1982 127
A2.12 Salinity across mouth of Hermitage Channel, May 1982 128
A2.13 Salinity cross Hermitage Channel stations 34-20, May 1982 129
A2.14 Salinity along Saint-Pierre Channel, May 1982 130
A2.15 Salinity along transect T3, 13 May 1982 131
A2.16 Temperature and density along T2, 13 May 1982 132
A2.17 Salinity from Saint-Pierre to Hermitage Channel, June 1982 133
A2.18 Salinity along T1 looking up the bay, 7 June 1982 134
A2.19 Salinity along T1 looking up the bay, 14 June 1982 135
A2.20 Salinity along Fortune Bay, June 1982 136
A2.21 Temperature and density along T2, 9 June 1982 137
A2.22 Salinity along T2, 9 June 1982 138
A2.23 Salinity along Fortune Bay, June 1982 139
A2.24 Salinity from Saint-Pierre to Hermitage Channel, November 1982 140
A2.25 Salinity across Sagona sill, November 1982 141
A2.26 Temperature difference, May minus June 1982 142
A2.27 Temperature and density difference, November minus June 1982 143

LIST OF TABLES

1.1 Water bodies in the Fortune Bay area 6
2.1 Cruises 14
2.2 Neil Brown MK IIIB specifications 16
2.3 CTD calibration results 17
2.4 Current meter and thermistor chain specifications 18
3.1 Long term temperature and salinity data 24
3.2 Wind stress from Saunders (1977) 29
6.1 Progressive vector plot data 95
7.1 Hermitage Channel data 104

Chapter 1 Introduction

1.1 Prologue

This thesis is a study of deep water exchange in Fortune Bay, a three sill fjord, located on the south coast of Newfoundland (Figures 1.1 and 1.2). Bounded by the Burin Peninsula to the east, Saint-Pierre and Miquelon to the southwest and Hermitage Channel to the west, Fortune Bay is particularly interesting because of its unusual geometry. Very few of the fjords which have been studied have had more than one sill permitting access to the fjord. It is not uncommon to have sills landward of the main mouth of the fjord thereby breaking the fjord up into partially separated basins but in Fortune Bay the situation is much different. Two of the sills on the northwestern side of the bay give access to Hermitage Channel (see Figure 1.2) while the third sill to the southwest gives access to the Saint-Pierre Channel. This unusual geometry and the different water masses carried into the region via these channel systems allow the study of a number of interesting physical problems.

1.2 Deep Water Exchange in Fjords

Exchange of deep water in fjords can occur over a variety of time scales and may be regular or intermittent. Exchange occurs when water of sufficient density arrives at the sill to displace water at the bottom of the fjord. The renewal may be partial or complete depending upon the transport and duration of the inflow and the nature of the system. A good review of the process of deep water exchange in fjords is given by Gade and Edwards (1980). A more up to date and complete review of the general dynamics of fjord oceanography can be found in Farmer and

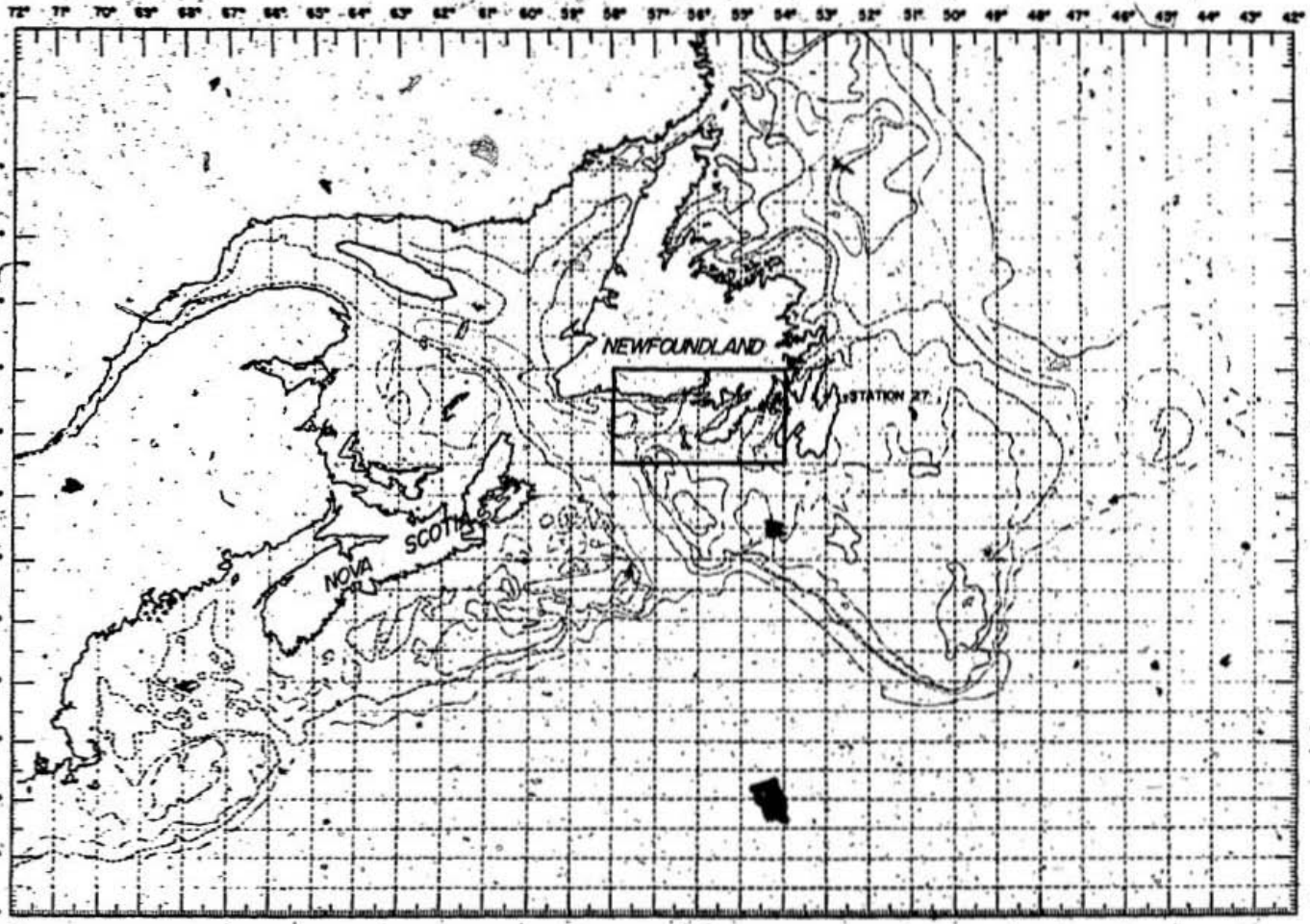


Figure 1.1 Location map showing the study area, located within the box.

Freeland (1983).

Forcing may come from within the fjord itself or more commonly in the coastal waters beyond the sill. Helle (1978), for example, studied changes in the water structure outside Byfjord, Norway as a result of variations in the coastal wind field. Replacement of deep water was observed to take place during the summer as a result of a longshore northerly wind. The exchange process was intermittent but well correlated with 2 to 7 day variations in the longshore wind stress. Reggie and Burrell (1981) describe exchange in an Alaskan fjord in which renewal is related to seasonal variations in the density of the continental shelf source water. Deep water renewal was observed to occur in the summer as a result of relaxation of a winter coastal downwelling condition.

The renewal may also be controlled by intra-fjordic events. In Howe Sound, Bell (1973) observed renewal to occur at times of maximum freshwater runoff and to be augmented by a down-fjord wind. Edwards and Edelsten (1977) show that renewal in Loch Etive is caused by low freshwater runoff. The inflow is described in terms of a density current inflow down a fairly steep slope of 6°. Matthews (1981) has also shown the effect of freshwater runoff in an Alaskan fjord where mixing in the fjord is caused by tidally induced internal waves.

Sill length, coupled with the tides, can also exert a controlling influence on deep water renewal. Where the sill is long, with respect to the tidal excursion, renewal is expected during neap tides. This is because the reduced energy available for mixing during neap tide periods leads to reduced mixing as dense water from outside passes over the sill. The density of the water entering the fjord will, therefore, be at a maximum and thus more likely to lead to deep water renewal. Geyer and Cannon (1982) invoke this explanation in their discussion of deep water

renewal in Puget Sound. For a sill which is short, with respect to the tidal excursion, the effect of mixing over the sill will not be as important and exchange is more likely during spring tides. Stucchi and Farmer (1976) provide evidence for this in their study of Rupert Holberg Inlet. There the sill is short with respect to the tidal excursion and spring tide transients are observed.

Exchange of deep water in a fjord will occur via a density current inflow, a phenomenon well described both theoretically (Smith, 1975; Bo Pedersen, 1980) and in the laboratory (Ellison and Turner, 1959). The oceanic analogue has been studied in different situations, most notably by Bo Pederson (1980) and by Smith (1975) who both analysed the dense water overflow in the Denmark Strait. Geyer and Cannon (1982) and Edwards and Edlesten (1977), applying the theoretical and laboratory work of Ellison and Turner, each describe in some detail the nature of density current inflow into a fjord.

Although it is well known that density current inflow is generated during deep water exchange and has been identified as a regular feature of many fjords this has often been inferred from density field plots produced from CTD surveys. Rarely has the density current inflow been studied directly. As a result, there is but a poor understanding of many aspects of the inflow, in particular the nature of the bottom and interfacial stresses.

1.3 Study Area

The study area is shown in Figures 1.1 and 1.2 with Fortune Bay in the center, Hermitage Channel to the west and the extension of the Avalon Channel through the Saint-Pierre Channel west to the Hermitage Channel. All of these channels contain fairly large bodies of water whose

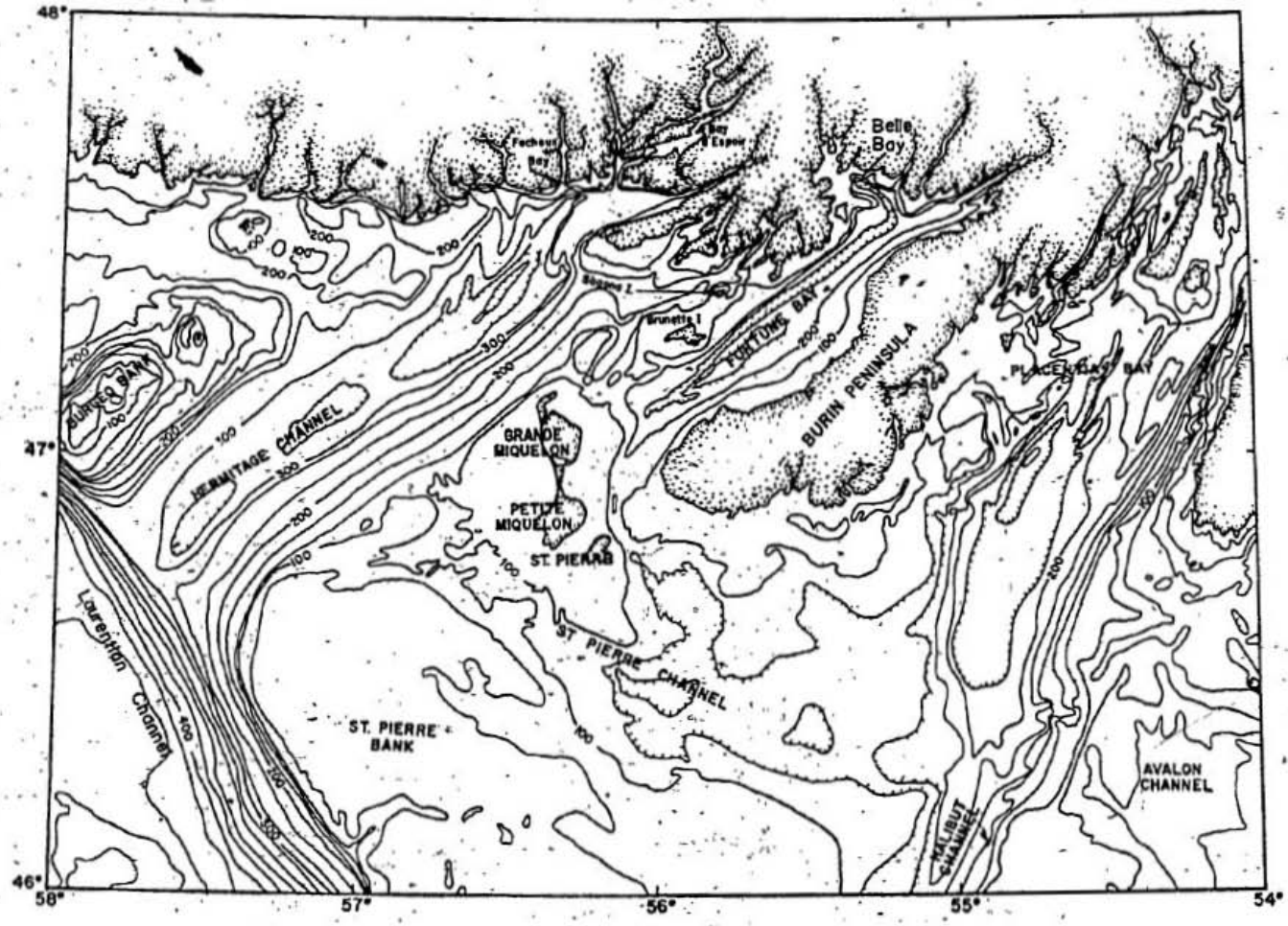


Figure 1.2 Detailed map of the study area. The contour depths are in meters.

dimensions and subsurface volumes, using the 100 meter contour as the boundary, are given in Table 1.1.

Table 1.1 WATER BODIES IN THE FORTUNE BAY AREA

Area	Length (km)	Width (km)	Mean Depth (m)	Volume (m^3)
St. Pierre	275	45	120	1.5×10^{12}
Fortune Bay	128	22	120	4.0×10^{11}
Hermitage Channel	137	40	200	1.1×10^{12}

The largest volume of water is contained in the Saint-Pierre Channel (as far east as 53° 30' W) with the least, down by a factor of four, in Fortune Bay itself.

Fortune Bay is oriented along a SW-NE line with a number of small bays along its shore towards the head of the bay. The maximum depth of the bay is 526 meters in Belle Bay, separated from the rest of the bay by a sill 195 meters deep. The mean depth of Fortune Bay is 120 meters, the maximum depth in the main part of the bay is 420 meters. In the center of the bay is a bank 15 kilometers long and about 180 meters deep with an area of 8×10^7 m^2. On either side of this bank are two channels: one on the northwestern side of the bay and the other on the southeastern side. The maximum depth in the northwestern channel is 360 meters, and that in the southeastern channel is 320 meters. The bay has three sills: one to the southwest and two to the northwest. These sills shall be called the Saint-Pierre, Miquelon and Sagona sills according to their geographic location. The limiting sill depths are 125, 115 and 100 meters respectively.

Very little is known of the geology of this area. In neighbouring Placentia Bay work has been done on both the geology and oceanography although very little of the latter has been published. The shores surrounding Fortune Bay and along the south coast are for the most

part fairly barren. In some places cliffs rise from the beaches to hundreds of feet in the air and are topped by tundra-like vegetation. The shores of the south coast area north of the Hermitage Channel have a mean elevation of about 500 to 1000 feet. The island of Miquelon is an exception to this in that it is surrounded by and composed of numerous sand banks. The Langlade, a sand bar joining the two major land masses of Miquelon, is a relatively recent geological feature having been formed at some time in the last century. The hydrographic charts of the area reveal that bottom types of the area range from sand to gravel, with clay predominating in many areas. In Fortune Bay itself the charts indicate many areas of gravel and gravel and sand mixtures.

Ice very rarely forms in Fortune Bay and does so only in the head of the bay. Local fishermen report that only a few times in the last twenty years has ice been observed anywhere in the bay. The small local harbours often freeze over by mid-February but this cover does not extend into the bay itself. Sea ice can exist in the Saint-Pierre and Hermitage channels. This ice is not locally produced but is advected from either the east or the west. In very heavy ice years, sea ice formed along the north coast of Newfoundland is carried by the wind and prevailing currents southwards eventually passing Cape Race where it can be carried as far west as Saint-Pierre. Likewise ice formed in the Gulf of St. Lawrence can be advected eastwards across Burgeo Bank and into Hermitage Channel. Ice would generally be observed in these areas in the late winter or the early spring and is almost always first year ice in very low concentrations.

1.4 Freshwater Runoff

The main source of freshwater is from the Bay du Nord River which

runs into Belle Bay in the northwest corner of the bay. The mean annual flow for this river is 39.7 $m^3 s^{-1}$ with two peak flow periods, one in the spring the other in the fall. No inflow data were obtainable for other rivers but it is estimated, based upon the work of Murray and Harmon (1969), that the average total freshwater input into the bay is about 100 $m^3 s^{-1}$. It is of interest to compare the relative freshwater inflow of this system with that of a more typical fjord. Helle (1978) presents data for Byfjord located on the west coast of Norway. This fjord has a total area of 55 x $10^6 m^2$ and a freshwater runoff of 320 $m^3 s^{-1}$ which gives a runoff to surface area ratio of 5.8 x 10^{-4} m s^{-1}. For comparison the total area of Fortune Bay is 3.3 x 10^9 m^2 which combined with runoff gives a ratio of 3.0 x 10^{-8} m s^{-1}.

One can also look at the total yearly freshwater flow into the bay which, expressed as a percentage of the volume of the bay, is 0.6%. We found no evidence that this inflow had any controlling influence on the dynamics of exchange in Fortune Bay. Nonetheless, a total yearly inflow of 3 x 10^9 m^3 does have some effect upon the upper waters of the bay and this can be seen in some of the CTD (Conductivity-Temperature-Depth) transect lines.

1.5 Regional Oceanography

Akenhead et al. (1981) analysed 9 years of monthly adjusted sea level data from two coastal stations and monthly steric height anomalies at station 27 (Figure 1.1) and showed that fresh water run-off from northern regions gives rise to a freshwater pulse which travels along the Labrador and Newfoundland coasts. Sea level was found to rise near Station 27 in May, and to peak in October. This analysis agrees well with the seasonal variations at Station 27 as documented by Keeley (1981) and Huyer and Verney (1975).

The Labrador Current Water mass has a temperature range of -1.7 to 3°C and a salinity range of 32 to 33 x 10^{-3}. (Salinity will be expressed according to the SUN Report, IUGG Publication Office, Paris, 1979). Petrie and Anderson (1978) estimate the mean flow of this current westward through the Avalon Channel to be 1 x 10^5 m^3 s^{-1} with fluctuating flow speeds of 0.05 to 0.2 m s^{-1}.

THe flow of water within the Laurentian Channel has been studied by El-Sabh (1977), Trites (1971) and earlier by Lauzier and Trites (1958). Water in the strait between Nova Scotia and Newfoundland has a two-layer structure. The upper layer above 100 meters has a temperature range of -1.7 to 3°C in winter and -1.7 to 17°C in summer. The salinity range is between 30 and 33 x 10^{-3}. On the Nova Scotia side there is a concentrated outflow, with inflow along the Newfoundland side at intermediate depths and near the bottom. Maximum flows were observed to occur in June and August.

Some of the Russian survey work carried out along the east coast has extended up the Laurentian Channel to the mouth of the Hermitage Channel. Kudlo and Burmakin (1972) have computed the dynamic topography relative to 200 dbar which indicates inflow along the north side of the channel with outflow along the south side. They also show a closed circulation pattern within the channel; inflowing water crosses the channel and then flows outwards. Their data, however, do not appear to justify this conclusion. No evidence for such a circulation was found in the present study. Also shown in Kudlo and Burmakin is inflow of water up into Hermitage Channel. This is in agreement with our results. There appears to be an inflow of cold Labrador Current Water along the southeastern side of the Hermitage Channel in the upper layer of the water column.

1.6 Oceanography of the Fortune Bay Area

Figure 1.3 shows the stations occupied during the course of this study. The station numbers indicated in the figure will be referred to both in the text and on the plots of temperature, salinity and density. A list of the station positions and depths can be found in Appendix I together with the station numbers.

A single section running from outside the Saint-Pierre sill across Fortune Bay and then out into Hermitage Channel is presented in Figure 1.4 showing the temperature, salinity and density (sigma-t expressed in units of kg m^{-3}).

There are two distinct water masses present at or below sill depth outside Fortune Bay: warm (3 to 7°C), saline (34 to 35 x 10^{-3}) Modified Slope Water (McLellan, 1957) extending from the bottom to depths of 125 to 175 meters in Hermitage Channel and cold (-1 to 1°C), relatively fresh (32 to 33 x 10^{-3}) Labrador Current Water (Keeley, 1981) in the Avalon Channels. Two distinct, physically separated, water masses having simultaneous access to a single fjord across different sills is unusual and has important consequences for the deep water exchange process in Fortune Bay.

If the density of the water at sill depth is great enough then deep water renewal will occur. For example, if the dense water at the bottom of station 55, in Figure 1.4, were to be driven over the sill then it would displace the less dense water at the bottom of the bay. This process is possible at any of the three sills. Two things are required: water at the sill with a density greater than that of the deep water in the bay and a mechanism to drive the water over the sill.

A tongue of cold water can be seen in Figure 1.4 riding up over the Saint-Pierre sill and down into Fortune Bay. Although not as

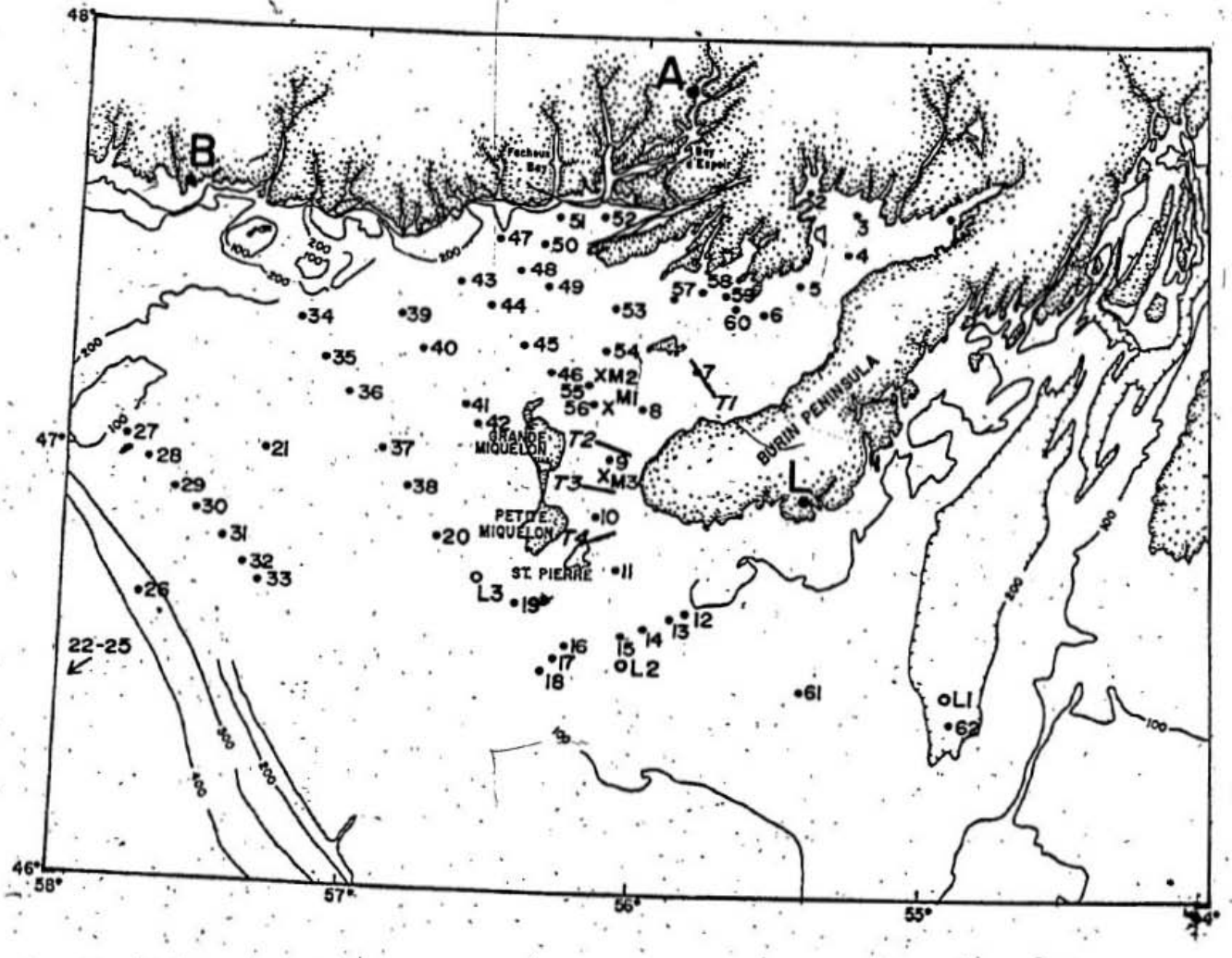


Figure 1.3 Detailed map of the study area showing the station locations. Stations 22-25 run along a line southwest across Laurentian Channel.

dramatic as inflows observed in later surveys, the cold water (less than 1°C) visible at mid-depths in the bay is a result of inflow of Labrador Current Water over the Saint-Pierre sill.

There is a strong density gradient separating both the Labrador Current and the Modified Slope Water from the overlying water outside the Saint-Pierre and Miquelon sills respectively. By contrast, the vertical density gradient is very much weaker throughout the water column in Fortune Bay. This suggests that intense vertical mixing accompanies the deep water exchange process (Pickard, 1963).

For the temperatures and salinity range of the waters observed here the density is primarily a function of the salinity. Thus, the salinity and the density plots contain essentially the same information. For this reason, and to conserve space, only the temperature and density plots will be discussed in the text. The salinity plots not in the text are in Appendix II.

In this work it will be shown that inflow over each of the sills is seasonal with the warm water inflow over the northwestern sills occurring in the winter period and cold water inflow over the Saint-Pierre sill in the summer period. A description of the field program and data analysis (Chapter 2) will be followed by a discussion of long term data for the Fortune Bay area in Chapter 3. A discussion of the temperature, salinity and density data for the area will then be given in Chapter 4. Density current inflow will then be reviewed in the context of these data, together with some theoretical analysis (Chapter 5). Mixing and flow over the Miquelon sill will be discussed in Chapter 6 followed, in Chapter 7, by an analysis of upwelling in Hermitage Channel as it relates to winter exchange over the northwestern sills. The eighth and final chapter will summarize the important results of this work.

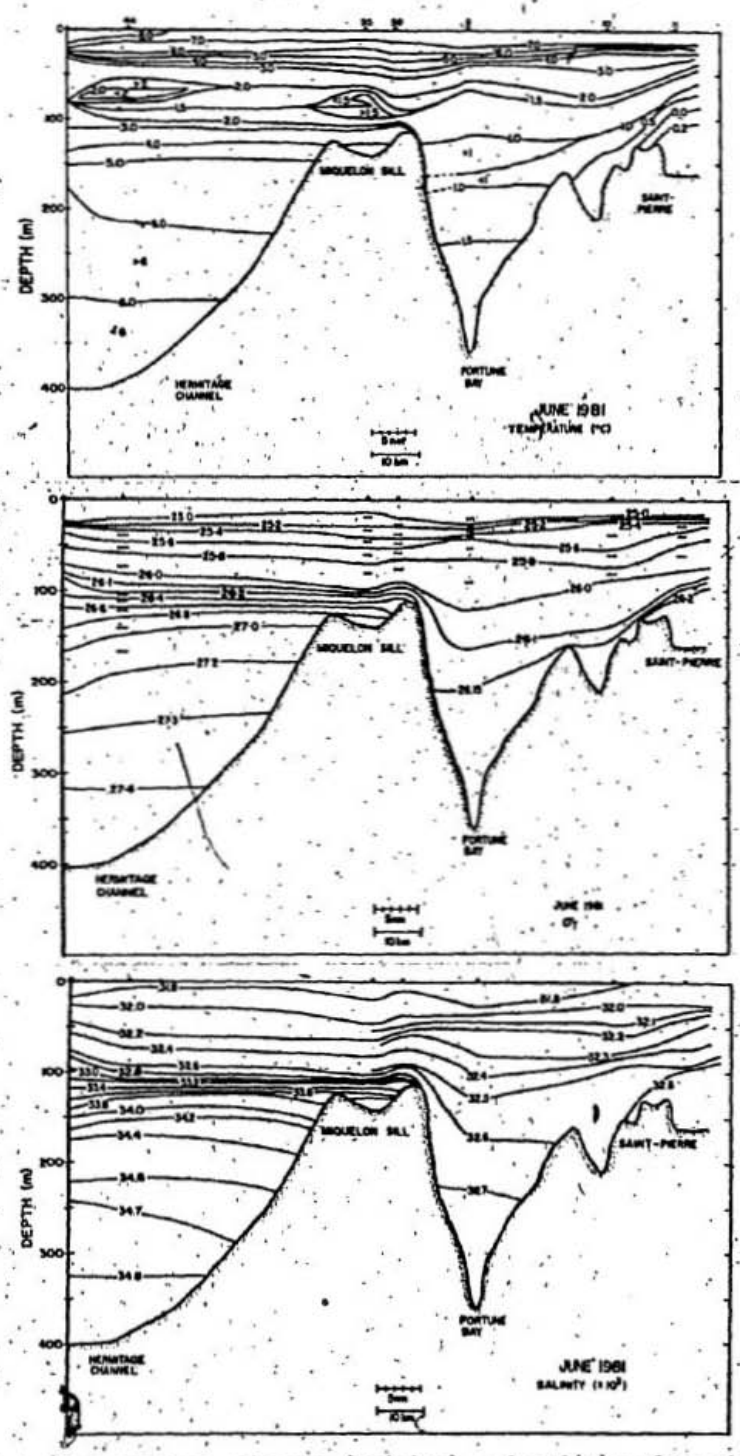


Figure 1.4 Temperature, sigma-t (density) and salinity from the Saint-Pierre Channel across Fortune Bay to Hermitage Channel. Station numbers are indicated along the top (1nm = 1.85km).

Chapter 2 Field Program and Data Analysis

2.1 Station Plan

The CTD and current meter data presented here were collected on cruises conducted by Memorial University. Bathythermograph data were collected by Northwest Atlantic Fisheries Center (NAFC) personnel on cruises conducted by them. Table 2.1 summarizes the cruises conducted from 1981 up until November 1982. In this chapter some of the techniques employed in collecting the data on these cruises will be described.

TABLE 2.1 CRUISES

CRUISE	SHIP	DATE	AREA
81-1	CSS PANDORA II	6-16 JUN 1981	G. Banks, Fortune Bay Area
81-4	CGS SHAMOOK	7-19 DEC 1981	Fortune Bay
82-1	CGS SHAMOOK	24 FEB, 2 MAR 1982	Fortune Bay
82-2	CGS DAWSON	4-14 JUN 1982	Fortune Bay Area
82-3	CGS SHAMOOK	2-14 JUN 1982	Fortune Bay Area
NAFC	CGS SHAMOOK	12-13 JUL 1982	Fortune Bay
82-8	CGS MARINUS	17-23 NOV 1982	Fortune Bay

Figure 1.3 shows most of the stations occupied in the south coast in the course of this study. The numbers beside each station will be referred to in the text and will also be found on the figures. Appendix I gives the latitude, longitude and depth for all the stations discussed.

Data from nineteen cruises will be presented. Twelve of these cruises were conducted by NAFC personnel as part of an ongoing larval herring and capelin survey of Fortune Bay undertaken by E. Dalley. The six Memorial University cruises were dedicated to a study of the physical

and biolgical oceanography of the region.

The station grid was designed to provide both general and specific coverage of the area. The stations in the Hermitage Channel were chosen both to look at the water structure in the channel and to permit the computation of the dynamic topography for determination of the circulation pattern. In Fortune Bay and the other channels most of the stations were placed along the axis of the channels and were appropriately spaced to provide good synoptic coverage. Within Fortune Bay and in the channel between the island of Saint-Pierre and the Burin Peninsula, closely spaced stations were placed across the axes of the channels. The transect line T1 was chosen to investigate the cross-bay differences and circulation within the bay while the lines T2, T3 and T4 were chosen to look at the detailed structure of the density current flow into Fortune Bay.

Three current meter moorings were deployed; M1, M2 and M3. The first two were placed on the Miquelon sill to look at the exchange and mixing there while the third, M3, was placed inside the Saint-Pierre sill to detect the dense water inflow over that sill.

2.2 BT and CTD Data

The main data set provided from the NAFC cruises was bathythermograph (BT) temperature data collected using Kahlsico bathythermographs. The maximum depth to which these probes could be lowered was 270 meters, this being a limitation of the pressure bellows. These BT's were calibrated on a regular basis. They are quoted by the manufacturer to be accurate to 0.1°C in temperature and 5 meters in depth.

Conductivity-Temperature-Depth (CTD) surveys were carried out by Memorial University personnel using a Neil Brown Instruments Systems

Mk IIIB CTD. Specifications for this instrument as quoted by the manufacturer are given in Table 2.2.

TABLE 2.2 NEIL BROWN MK IIIB CTD SPECIFICATIONS

SENSOR	RANGE	ACCURACY	RESOLUTION
Pressure	0-1600 x 10 kPa	1.6 x 10 kPa	0.024 x 10 kPa
Temperature	-32 to 32°C	0.005°C	0.0005°C
Conductivity	1 to 65 $k\Omega^{-1}$/cm	0.005 $k\Omega^{-1}$/cm	0.001 $k\Omega^{-1}$/cm

Field checks of this instrument were carried out using reversing thermometers and Niskin bottles on a General Oceanics model 1015-12 rosette to which the CTD was also attached. Water samples and temperatures were taken in regions with weak gradients of temperature and salinity at every third or fourth station. Water samples were analysed for salinity using a Guildline Model 8400 Autosal which was calibrated using standard sea water obtained from the Institute of Ocean Sciences in Wormley, England. The accuracy of this instrument is rated by the manufacturer to be 1 part per million. The reversing thermometers, made by Watanabe Keiki, are rated by the manufacturer to be accurate to 0.01°C, although in practise it is felt that an accuracy of 0.02°C is more realistic.

Table 2.3 presents the results of the calibration analysis for five cruises conducted during this study. In Table 2.3 $\overline{\Delta S}$ and $\overline{\Delta T}$ are the mean errors in salinity and temperature respectively. The standard deviation σ is also shown.

of Berteaux (1976) was referenced. Stainless steel shackles, stainless steel thrust bearing swivels and galvanized shackles at a limited number of points were used. Galvanized wire was used with Samson power braid to isolate components of the mooring. Mesotech 501-AR acoustic releases were used, singly in Moorings 1 and 2 and paired in Mooring 3. All of the moorings were deployed buoy first and because of the shallow water depth, by allowing the double train wheel anchors to free fall to the bottom.

The current meters used, Aanderaa RCM4's, were calibrated post cruise at the Bedford Institute of Oceanography. Calibrations were carried out for temperature, direction and conductivity. Table 2.4 gives the specifications supplied by the manufacturer for these instruments.

TABLE 2.4 CURRENT METER AND THERMISTOR CHAIN SPECIFICATIONS

SENSOR	RANGE	ACCURACY	RESOLUTION
RCM4 Speed	2.5 to 250 cm s^{-1}	2% or 1	Threshold 2.0
RCM4 Temp	-2.46 to 21.40°C	0.1	0.01
RCM4 Cond	0 to 77 $k\Omega^{-1}$/cm	0.2	0.07
RCM4 Dir	1-360°	5 to 7.5	0.3
RCM4 Pres	0-650 x 10 kPa	6.5	0.65
Therm Chain	-2.46 to 21.4°C	0.1	0.02

Problems with the compass measurements of Aanderaa current meters have been well documented by Keenan (1979,1981) and Forbes and Church (1980). Especial care was taken in using the meters to choose tapes with no remnant magnetic field and to isolate the meters from other magnetic components in the mooring.

The thermistor chains used, also of Aanderaa manufacture, were also calibrated post cruise at the Bedford Institute of Oceanography. The 63% response time of the instruments is rather slow at three minutes but adequate for the purposes of this study.

TABLE 2.3 CTD CALIBRATION RESULTS

Cruise	$\overline{\Delta S}$ ($\times 10^3$)	σ	$\overline{\Delta T}$°C	σ
81-1	0.0011	0.012	-0.008	0.023
81-4	0.0071	0.014	-0.023	0.046
82-2	-0.0092	0.024	0.0040	0.044
82-3	0.0080	0.011	-0.0037	0.018
82-8	0.0080	0.0080	-0.0040	0.026

These are not meant to be interpreted as strict calibrations but rather as checks to ensure that the instrument was in calibration. Based upon this table, we can say that the maximum errors in temperature and salinity would be 0.01°C and 0.01 x 10^{-3} respectively. The large values of the standard deviation are felt to be a result of the calibration technique itself and not instrumental error. In January of 1982 the CTD went through a partial calibration at the factory and was found to be very close to specifications in temperature and pressure. The maximum error in temperature was found to be ten millidegrees. At that time a newly calibrated conductivity sensor was installed because of damage done to an earlier one.

Data from the CTD were recorded at 31.25 Hz on a Sony TC-339 analog tape recorder and, on cruises where possible, on a MINC 11/03 twin floppy diskette drive minicomputer. Ultimately all CTD analysis was carried out using the MINC 11/03 system.

2.3 Current Meter Moorings

Diagrams for the three current meter moorings are shown on Figures 2.1, 2.2 and 2.3. Numbers immediately to the left of the mooring indicate the buoyancy in pounds (1 pound = 0.454 kilograms). No computer analysis was carried out in the design of these moorings although the work

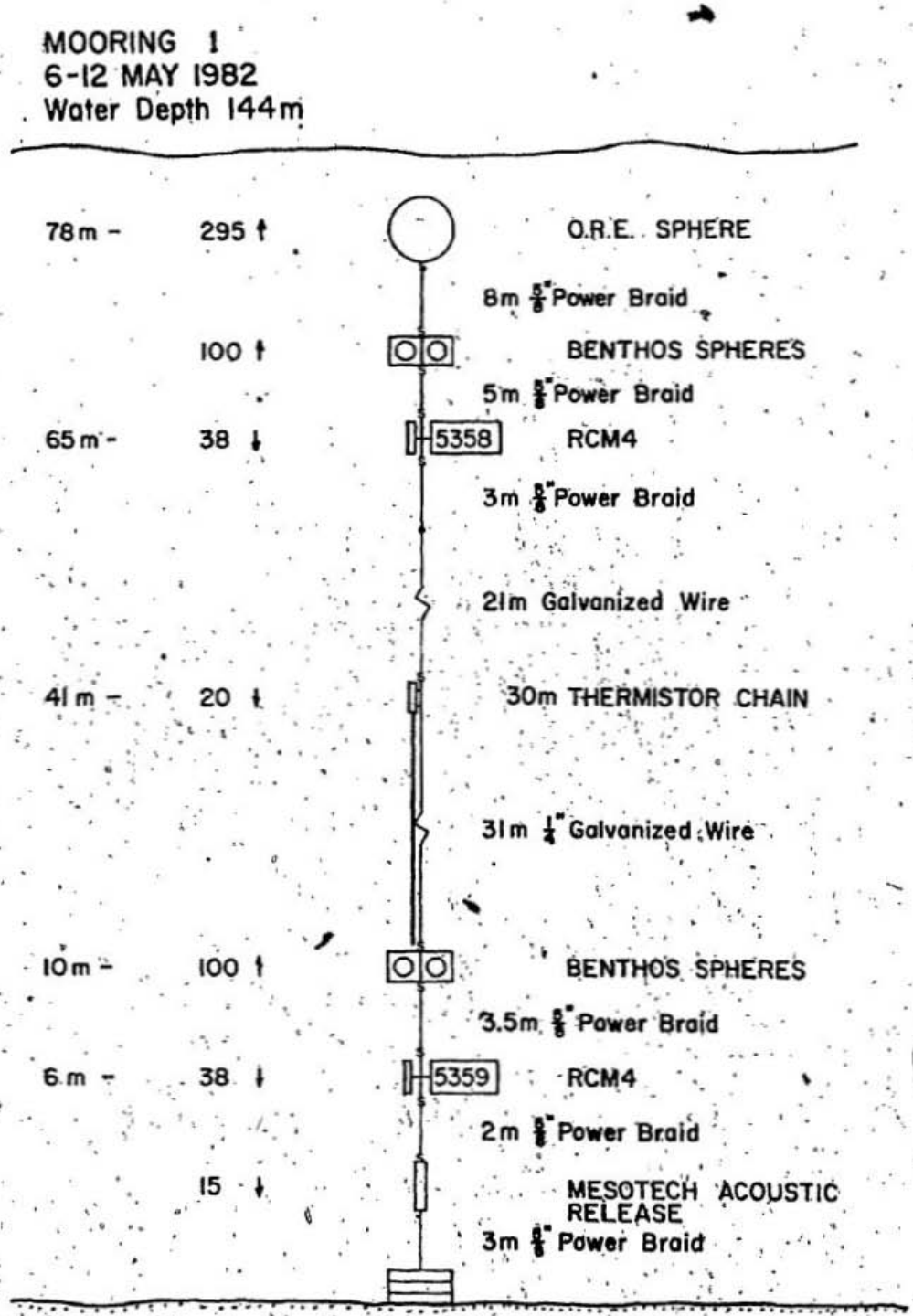


Figure 2.1 : Mooring 1. The measurements at the extreme left are heights above the bottom. Figures to the right of these heights give the buoyancy of each component in pounds (1 pound = 0.454kg).

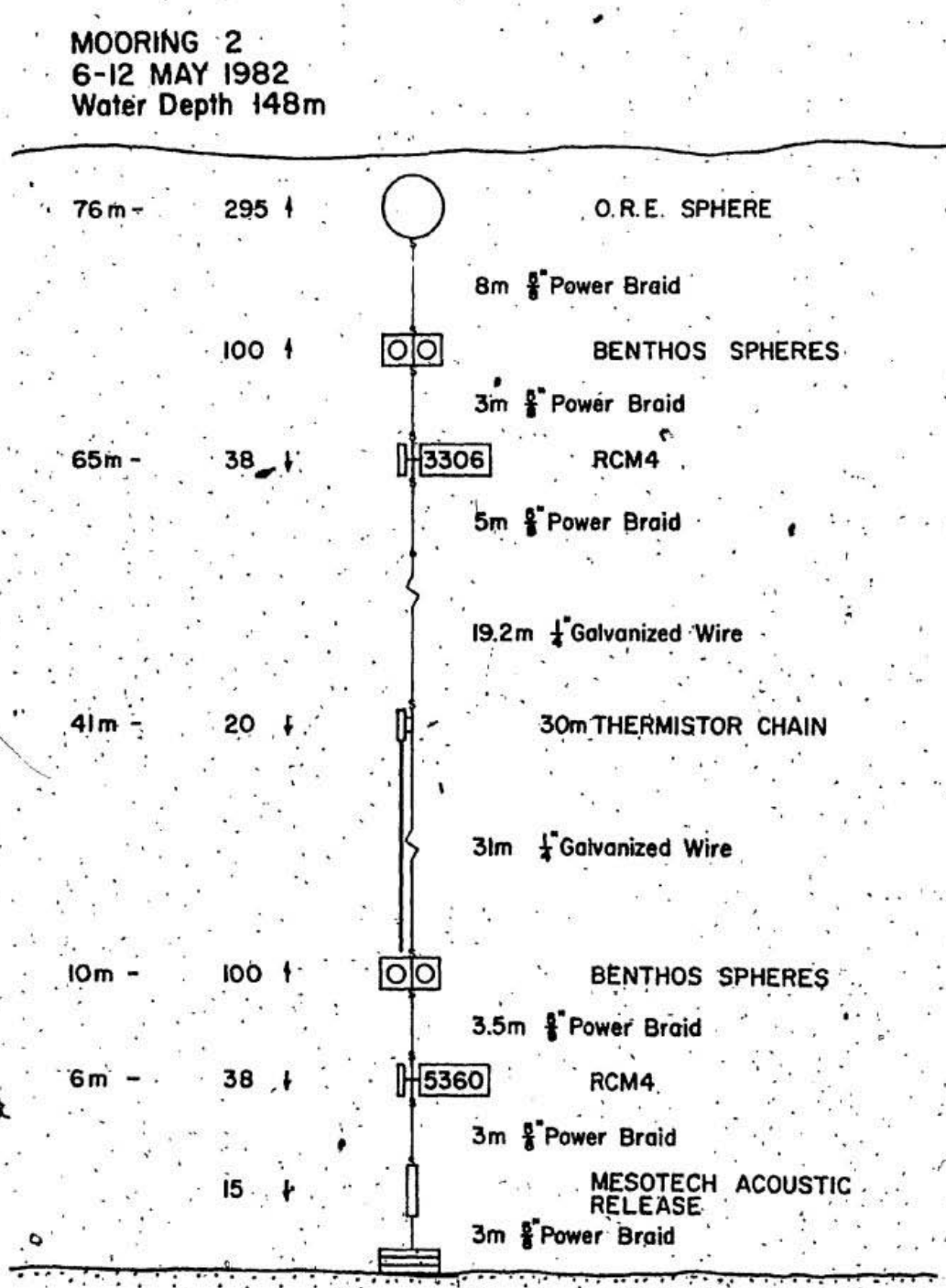


Figure 2.2 Mooring 2. The measurements at the extreme left are the heights above the bottom. Figures to the right of these heights give the buoyancy of each component in pounds (1 pound = 0.454kg).

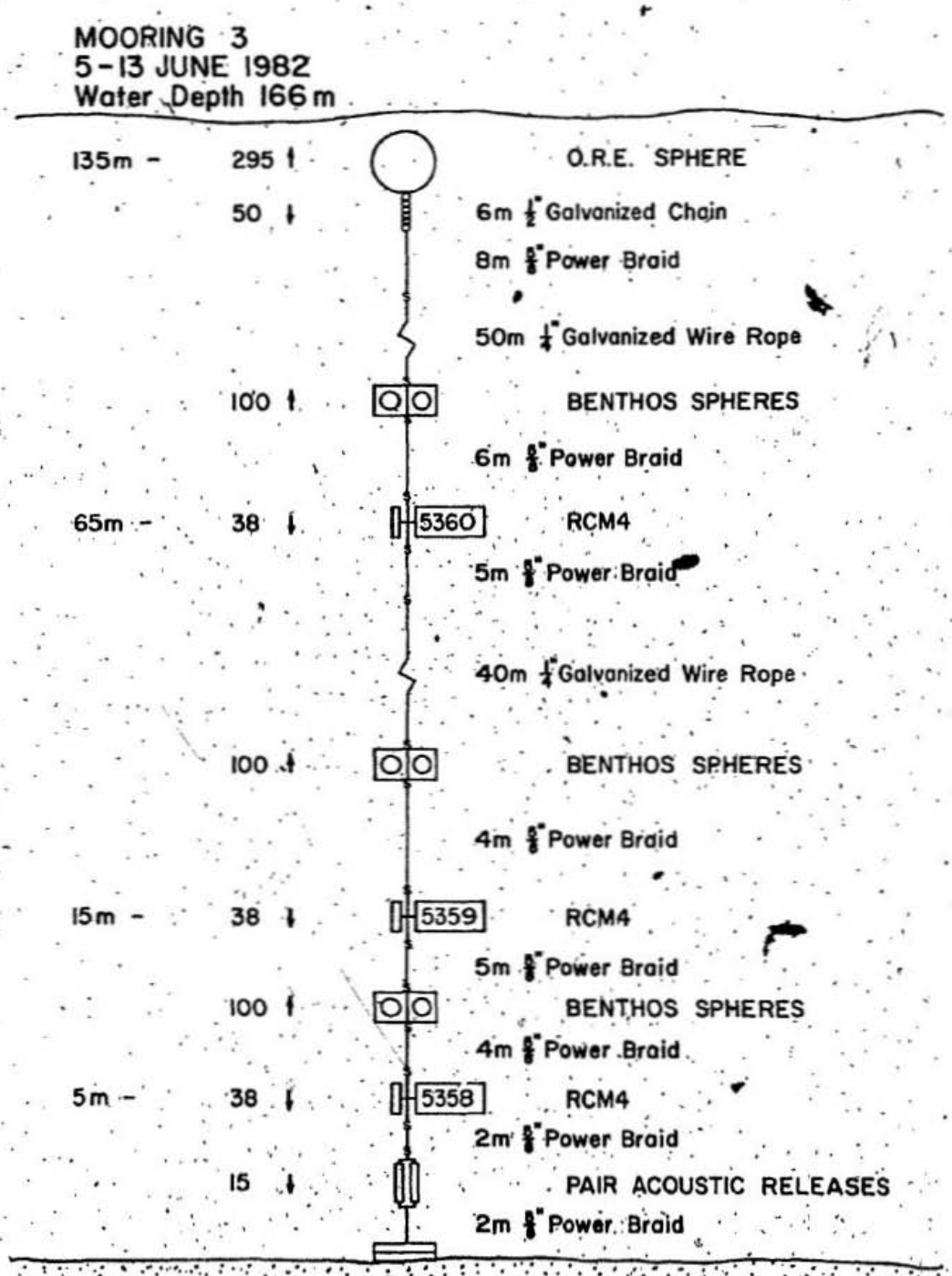


Figure 2.3 Mooring 3. The measurements at the extreme left give the height of each component above the bottom. Figures to the right of these heights give the buoyancy of each component in pounds (1 pound ≈ 0.454kg).

2.4 Dissolved Oxygen and Nutrients

Dissolved oxygen was determined at sea using the Winkler titration method as described in Strickland and Parsons (1972). This procedure is estimated to be accurate to ± 5% in dissolved oxygen concentration.

Nutrient samples, taken in 0.200 litre Nalgene bottles, were frozen at sea for later analysis in the laboratory. Analysis was done in the Water Analysis Facility of the Chemistry Department at Memorial University. The analysis was done on a Technicon Autoanalyzer to an accuracy of 0.014 mg/l for nitrogen, 0.002 mg/l for phosphorous and 0.01 mg/l for silicate.

2.5 Data Reduction and Analysis

CTD data was collected on audio magnetic tape and analysed using a MINC 11/03 microcomputer. All the data reduction and analysis were done on software written for this system in either BASIC or FORTRAN. Salinity and density were computed using the UNESCO 1978 practical salinity formula described by Millero and Poisson (1981). In the BASIC software density and salinity were computed from single values of pressure, temperature and conductivity. In FORTRAN these computations were made using pressure and temperature with an average of the previous five conductivities. This was done in an attempt to reduce the effect of salinity spiking caused by the mismatch between the time constants of the conductivity and temperature sensors. Plotting of the data was done using a Tektronix model 4662 digital plotter. Some of the BASIC software which was used is described in Dodge (1982). CTD data from NAFC was used for only one cruise. All contour plotting of the CTD data was done by hand.

The BT data were analysed by technicians from NAFC who read the slides using BT readers calibrated to the BT in use. The values were recorded on

log sheets, copies of which were then used for our analysis.

The data for the current meters and thermistor chains were recorded on 3 1/4 inch magnetic tapes which were translated at the Bedford Institute of Oceanography. Plots of the raw and filtered data were made on computer facilities at the Bedford Institute. Further analysis of the translated data was then done on the VAX 11/780 computer system at Memorial University. Contouring of the thermistor chain temperature data was done using the Surface II contouring package prepared by the U.S. Geological Survey and installed on the VAX 11/780 computer system.

Bottle data were obtained for the south coast area from the Marine Environmental Data Service (MEDS). The data were collected using Niskin and Nansen bottles with reversing thermometers. Most of the data were collected during the winter.

Weather data were obtained from the Atmospheric Environment Service for three stations on the south coast. The data were checked to ensure that the pressure data used were properly recorded by comparing with pressure charts kept at Nordco Ltd. in St. John's. The data were analysed using the VAX 11/780 computer system at Memorial University.

Wind data for Saint-Pierre were obtained directly from the weather charts kept at Nordco Ltd. in St. John's. Wind speed and direction were read directly from the surface pressure charts. This was done because it was not possible to obtain the data from any of the international weather services. The accuracy of the data taken from the weather charts is not considered to be high: 20 degrees in direction and 5 knots in speed.

Chapter 3 Long Term Data

3.1 Channels Adjacent to Fortune Bay

Several types of long term data exist for the Fortune Bay area. Bottle data for the period 1948-1973 were obtained from the Marine Environment Data Service (MEDS) for the entire south coast area shown in Figure 1.1. Unfortunately most of the data were taken outside Fortune Bay in the Saint-Pierre and Hermitage channels. In spite of this, the data obtained did provide some useful results concerning the Labrador Current Water in the Saint-Pierre Channel.

The data set consists of temperature and salinity data at a set of standard oceanographic depths for stations in the Saint-Pierre and Avalon channels. The positions of the four stations to be discussed (Station 27, L1, L2 and L3) are shown in Figures 1.1 and 1.3. The data are for three consecutive years; 1953, 1954 and 1955. These were the only three years for which data were available at each of the stations. Table 3.1 presents the temperature and salinity averages, together with their standard deviations, for March and August, again the only two months for which data were available at all the stations.

TABLE 3.1 LONG TERM TEMPERATURE AND SALINITY DATA.

Station Name	Temperature (°C)				Salinity ($\times 10^3$)			
	August		March		August		March	
	$\bar{T}$	σ	$\bar{T}$	σ	$\bar{S}$	σ	$\bar{S}$	σ
Station 27	-1.14	0.22	-.27	0.19	33.28	0.09	33.31	0.08
L1	-1.04	0.17	-.47	0.26	33.18	0.02	32.70	0.04
L2	-0.71	0.27	-.11	0.30	32.84	0.08	32.62	0.17
L3	-.26	0.30	0.73	0.53	32.70	0.06	32.43	0.08
L3-L1	0.78	0.19	1.21	0.64	-0.48	0.07	-0.27	0.07
L2-L1	0.33	0.11	0.36	0.06	-0.34	0.10	-0.08	0.13

From Table 3.1 it can be seen that the lowest temperatures and highest salinities, thus highest densities, are in August. The highest temperatures and lowest salinities, thus lowest densities, occur in March. Data obtained in two separate months of the year do not locate the maxima or minima but do show the difference between the spring and summer bottom water conditions outside the Saint-Pierre sill.

The observed seasonal signal corresponds well with that described in much greater detail for Station 27 by Huyer and Verney (1975) and Keeley (1981). Petrie and Andersen (1983) have described this seasonal variation as arising from the spring melting of the pack ice in the Labrador Sea and Baffin Bay. This melting causes a pulse of cold, relatively fresh water to move along the coast.

The data also show a horizontal gradient in temperature, and to a lesser extent salinity. Listed below the station means in Table 3.1 are the means of the differences between pairs of the stations. The bottom temperature increases to the west while the salinity appears to decrease. To some extent this may be a function of bottom depth (Station 27, L1, L2 and L3 are 176, 210, 160 and 100 meters deep respectively) although the stratification below 100 meters is weak. This horizontal gradient is intriguing though not definitively proven by these data.

This seasonal variation in water properties outside the Saint-Pierre sill will turn out to exert an important influence on the exchange of deep water in Fortune Bay. It is important that the maximum density and minimum temperature are observed outside the Saint-Pierre sill at some time in the summer although the seasonal data presented in Figure 3.1 cannot be used to define, more precisely, when the mimimum temperature will be observed. Observations to be presented indicate that this time is highly variable.

3.2 Seasonal Variations in Fortune Bay

Time series of temperature data for stations 4 and 8, in Fortune Bay, (Figure 1.3) are plotted in Figure 3.1. CTD data for the cruises listed in Table 2.1 and BT data for the other NAFC cruises were used. The maximum depth at which temperatures were recorded was 270 meters because of the previously mentioned limitation in the BT.

The maximum deep water temperatures at station 8 were observed in February 1980 (1.9°C), June 1981 (1.9°C) and February 1982. The minimum temperatures were observed in August 1980 (-.1°C), December 1982 (0.5°C) and June 1982 (-.25°C). Thus, the maxima are observed to occur in the first half of the year while the minima occur in the latter half.

Up until 1980 the visual correlation between stations 8 and 4 is strong. After this time station 4 was not occupied as regularly as station 8 making further comparison difficult. The timing of these minima and maxima are not exact because of the paucity of measurements and the irregularity at which they were made. They do nonetheless indicate a trend of warm deep water in the winter and cold deep water in the summer.

Some visual correlation exists between the temperature changes at 270 meters and 200 meters amd higher up. The visual correlation breaks down above 150 meters. This may be a result of advection of water over the sills which are all at a depth of between 100 and 125 meters.

Discussion of the salinity data will be reserved to a later point in this work once the CTD data have been presented in more detail. This is a reasonably acceptable procedure in that the temperature is well correlated with each water mass so that a low temperature will always

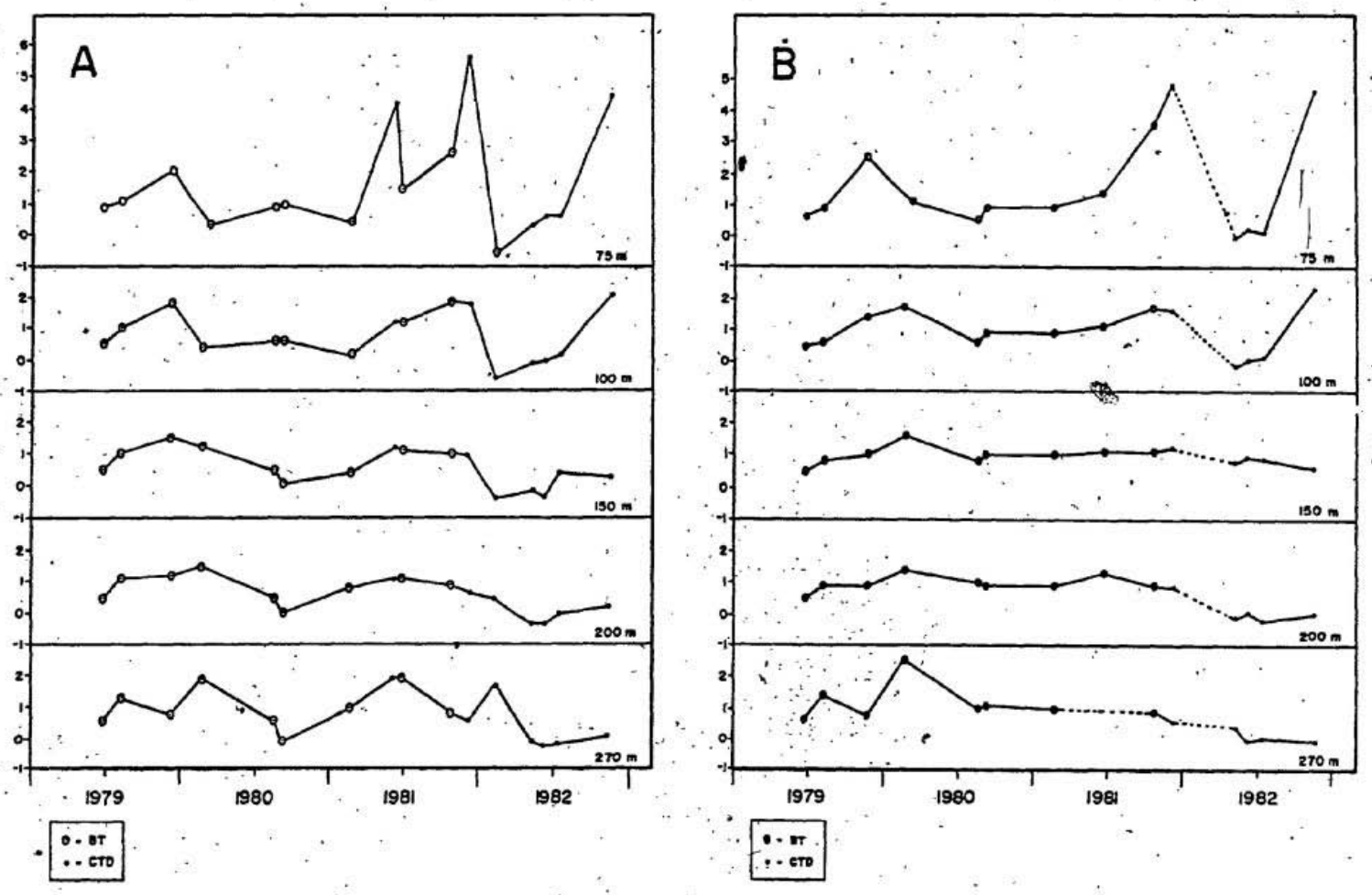


Figure 3.1A Temperature in °C at station 8.

Figure 3.1B Temperature in °C at station 4. The dashed lines indicate no data at station 4 when there were data at station 3.

be associated with the Labrador Current and a high temperature with the Modified Slope Water.

3.3 Seasonal Variations in the Wind Field

Having established this seasonal variation in the deep water temperatures it is logical to search for a driving force which can control it. The forcing function should drive warm water over the Miquelon sill in winter and cold water over the Saint-Pierre sill in summer. In Section 3.1 it was shown that bottom water outside the Saint-Pierre sill is colder and more dense in August than in March. This correlates well with the observed minimum deep water temperatures within the bay. A lack of data had made it impossible to look for seasonal variations in Hermitage Channel although some changes are expected (El-Sabh, 1977).

It is expected that changes in the wind field from summer to winter will exert a strong influence upon the system. Wind data (Canadian Normals, 1975) for the weather station at Grand Bank, located about one-third the way up the eastern shore of Fortune Bay show, a clear shift in the seasonal winds. In the summer, July-August-September, the winds are predominantly from the southwest (over 30%) while winter winds are from the northwest (28%) and northeast (18%). The mean wind speed increases from 10 mph (4.5 m s^{-1}) in the summer to 17 mph (7.6 m s^{-1}) in the winter.

The analysis of these wind data is in agreement with the earlier work of Saunders (1977) who analysed 31 years of wind data reported from ships along the Atlantic seabord. Mean wind stresses were computed in one degree square areas over four three-month periods corresponding to winter, spring, summer and fall. Saunders' results for a point just south of Saint-Pierre, a degree square centered at 46° 30' N 56° 30' W, are presented in Table 3.2. Wind direction is given as the direction from

which the wind is blowing.

TABLE 3.2 WIND STRESS FROM SAUNDERS (1977)

PERIOD	WIND STRESS N m^{-2}	WIND DIRECTION (degrees true)
DEC-JAN-FEB	0.136	276
MAR-APR-FEB	0.028	300
JUN-JUL-AUG	0.020	220
SEP-OCT-NOV	0.051	275

There is a clear seasonal trend with the greatest wind stresses occurring in the winter period when the wind direction is from the west. There is a summer shift to the southwest when the mean wind stress is significantly reduced.

Analysis of the wind field for three south coast stations was carried out using atmospheric pressure data reduced to sea level. The pressure data are accurate to 0.02 kPa. The three stations used were St. Lawrence, St. Alban's and Burgeo which are indicated in Figure 1.3 by L, A and B respectively. The wind data from these stations were not used because of prographic effects. The line between St. Alban's and St. Lawrence will be referred to as the offshore direction with that between St. Alban's and Burgeo as the longshore direction. The pressure differences will be computed as P_A minus P_L and P_A minus P_B so a positive offshore difference will mean that $P_A > P_L$.

No data were available for the night period at station A so only data from 06:00 until 18:00 local time were used at all three stations. The coordinate system used here has positive x directed inland and positive y directed westward along the coast. The wind velocity was calculated using the geostrophic equation written as:

$$\vec{U} = \frac{1}{\rho_a f}\left(\frac{\Delta Py}{\Delta y}\hat{i} + \frac{\Delta Px}{\Delta x}\hat{j}\right) \qquad (3.1)$$

where ΔP_x = offshore pressure difference $(P_A - P_L)$; ΔX = offshore distance; ΔP_y = longshore pressure difference $(P_A - P_B)$; ΔY = longshore distance and f is the Coriolis parameter equal to $2\Omega\sin\phi$ where Ω is the rotational speed of the earth and ϕ is the latitude. The data were used to compute the wind stress according to the quadratic drag law:

$$\vec{\tau}_a = \rho_a C_D |\vec{U}| \vec{U} \tag{3.2}$$

where $\vec{\tau}_a$ – wind stress

ρ_a – density of air

C_D – drag coefficient for a wind at 10 meters

Here C_D was taken to be 1.5×10^{-3} based upon the work of Pond (1975). Substitution of 3.1 into 3.2 yields:

$$\vec{\tau} = \frac{C_D}{\rho_a f^2}\left[\frac{\Delta P_x^2}{\Delta X^2} + \frac{\Delta P_y^2}{\Delta X^2}\right]^{1/2}\left(\frac{\Delta Py}{\Delta Y}\,\hat{i} + \frac{\Delta Px}{\Delta X}\,\hat{j}\right) \tag{3.3}$$

The offshore τ_{off} (the $\hat{i}$) and longshore τ_{long} (the $\hat{j}$) components of the wind stress computed using this equation were then filtered using three successive 10 day moving average type filters where the sampling period was one hour with 12 points in a day. This was done to remove any signal having periods shorter than 7 days. The real effect of this filtering on the data is difficult to deduce because of the uneven sampling frequency of the data. This filter was chosen to remove the effect of high frequency atmospheric events, since it is expected that the response of the ocean to variable winds will act like a low pass filter.

A plot of pressure smoothed using a 30 day moving average of the data is presented in Figure 3.2. This plot shows the seasonal variation in

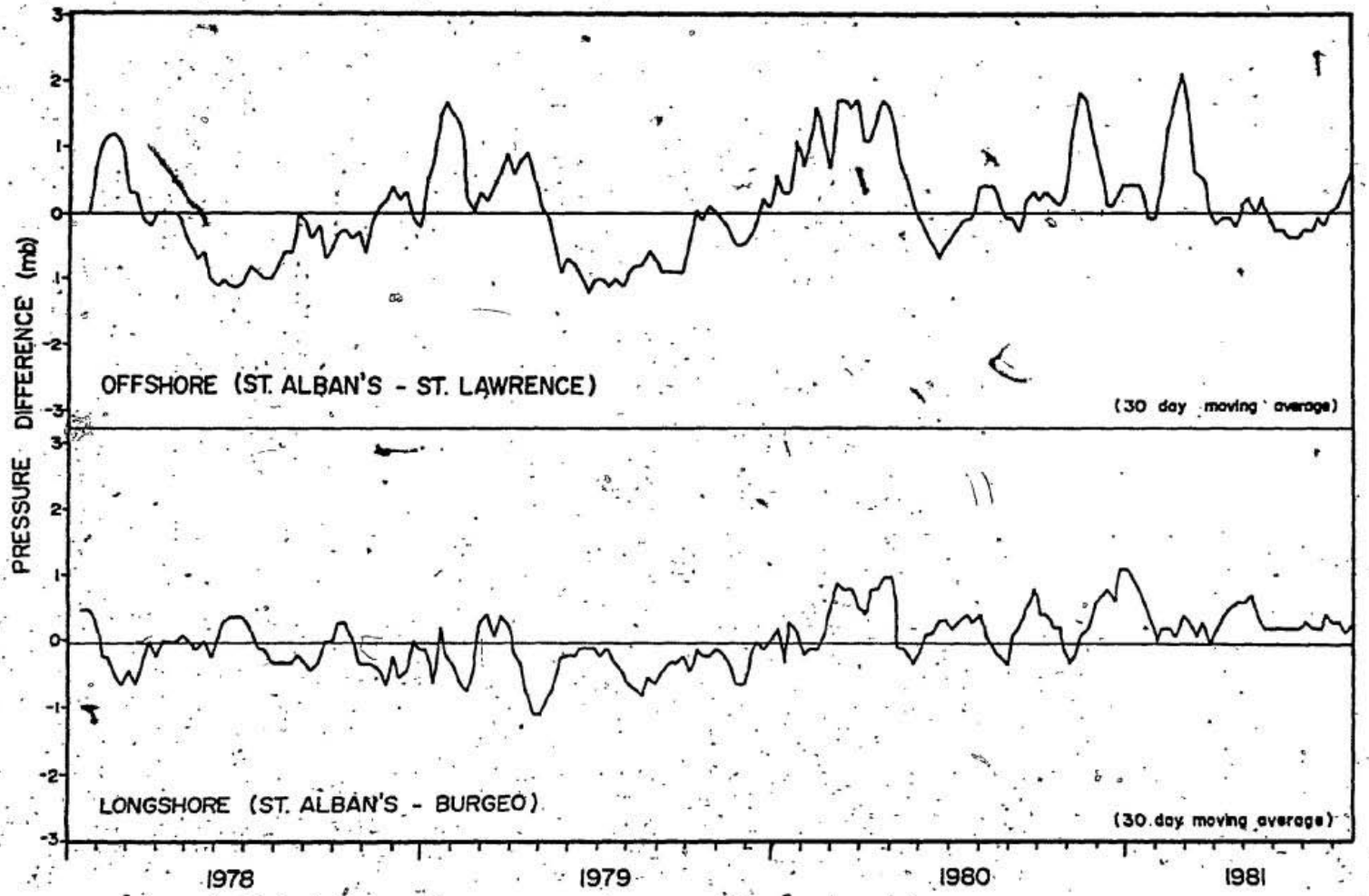


Figure 3.2 Offshore and longshore pressure difference. Large vertical bars on the horizontal axis indicate the beginning and end of each year (Note 1mb = 0.1kPa).

the offshore pressure signal with positive gradients observed in the winter and negative gradients observed in the summer. Figure 3.3 shows the computed wind stress which is filtered as described above and more clearly shows the seasonal variation in the wind stress in both direction and magnitude. (A pressure of 0.1 kPa (1 mb) between A and L corresponds to a geostrophic wind of 12 m/s). The maximum surface stress occurred in the early winter of 1980 with a value of 1.3 $N m^{-2}$ corresponding to a geostrophic wind of 25 m/s. Note that the wind speeds computed applying the geostrophic assumption will always be higher than the wind speed at 10 meters. A variety of factors such as stability, friction and weather system structure will effect the actual reduction to wind at 10 meters (Nelson, 1977). For simplicity we shall only discuss the geostrophic wind accepting that it is to high.

High wind stresses, greater than 1.0 $N m^{-2}$, are observed only in the winter and always correspond to positive longshore stresses. Such a wind stress combined with the onshore stress corresponds to a wind from the northeast. In the summer period there are no periods of high stress. For the first three years weak negative longshore and oscillating onshore wind stresses form a pattern which breaks down in 1981 when weak positive stresses are observed in the longshore and onshore directions. The most important point to note for the summer is that there do not appear to be any extended periods of strong winds.

From summer to winter there should be an increase in the surface wind relative to the geostrophic wind which can be explained using a stability argument. In the summer warm air from the southwest blows over cooler water so the air mass should be relatively stable. In the winter cold northerly air blows over warmer water making it unstable. These

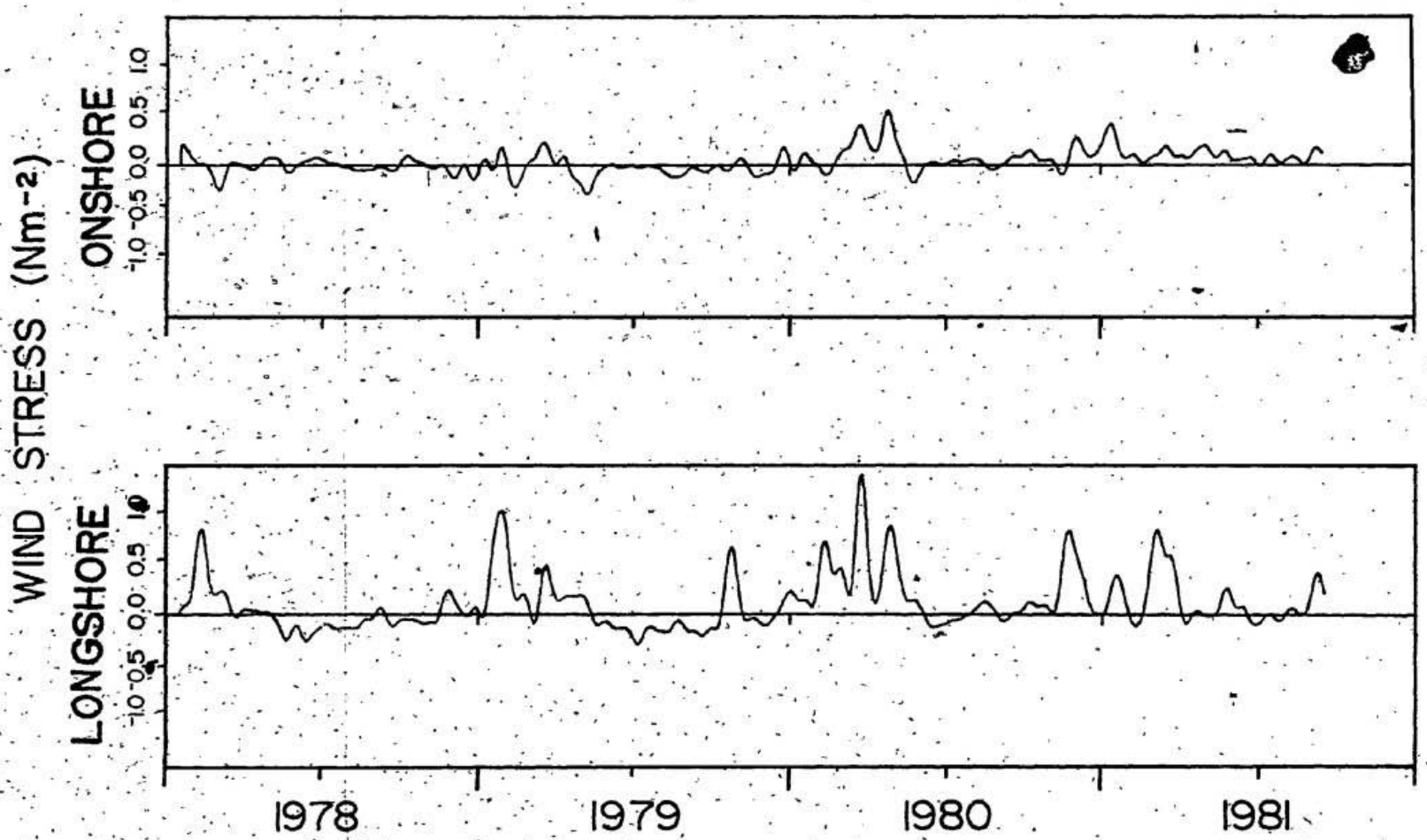


Figure 3.3 Onshore (top) and longshore (bottom) components of the wind stress. Large vertical bars on the horizontal axis indicate the beginning and end of each year.

effects will not be detectable in the pressure data but will mean that the real stress in the winter relative to the geostrophic wind is larger than in the summer.

The shift in the mean wind direction from the summer to the winter is interpreted to be a result of a shift in the main storm tracks. The change in intensity from summer to winter is a feature common to all the winds in the ares. It is the change in the wind direction that is particularly interesting. All of the reporting weather stations to the east of this area show the mean wind to be from the southwest for both the summer and the winter. All of these observations are in agreement with the Grand Bank data discussed earlier and the work of Saunders (1977).

Strong northeasterly and northwesterly winds, favourable to upwelling in Hermitage Channel, have been shown to occur in the winter. These winds have also been shown to coincide with the period when warm water is observed deep in Fortune Bay. This suggests that the northeasterly or northwesterly winds are at least partially responsible for the winter inflow of warm Modified Slope Water into Fortune Bay. In Chapter 7 an analytical argument will be made to show that northeasterly winds are indeed capable of generating an inflow.

Chapter 4 The Oceanography of Fortune Bay and Adjacent Channels

4.1 Circulation in Hermitage Channel

Temperature and density sections across Laurentian Channel and up Hermitage Channel in May 1982 are presented in Figure 4.1. The positions of the stations discussed in this section and all others within this chapter are shown in Figure 1.3 and listed in Appendix II. Apparent in Figure 4.1 is a strong outflow in the top 100 meters of the water on the southwest side of Laurentian Channel. This represents the spring outflow from the Gulf of St. Lawrence (El-Sabh, 1977).

The coldest water in the system (< -0.5°C) is on the south side of the channel but extends only to the centre. At the center station there in only a very thin section of water with temperature below zero degrees. The section of cold water on the north side of the channel appears to be flowing upchannel, consistent with the observations of Kudlo and Burmakin (1972) to the southeast and of El-Sabh (1977) to the northwest. Flow on the northwest of the channel is expected to be influenced by Hermitage Channel.

Stratification and flow below 200 meters are weak. The immediate source of the Modified Slope Water for Hermitage Channel is observed here. Temperature and salinity below 150 meters are 3.0 to 6.0°C and 34.0 to 35.0 x 10^{-3}. The maximum density observed within Laurentian Channel was just greater than 27.6.

In Hermitage Channel the water below 150 m is warm, greater than 3.0°C, and dense, greater than 27.0. There is a thick lens of cold water in the upper section of the water column which thins towards station 44. The slope of the isopycnals at this station indicates the

presence of current shear, horizontal, vertical or both. The isopycnals rise up from the left and then drop down to the right across the station.

Figure 4.2 shows a transect of temperature and density across Hermitage Channel near its mouth. The weak slope of the isopycnals downwards to the right between 100 and 200 meters provides some evidence for weak inflow in the lower layer on the southeast side and weak outflow on the northwest side of the channel. Figure 4.3 shows the temperature and density for a cross section just to the southwest of Miquelon. A strong northeasterly flow of the cold Labrador Current Water along the southeastern side of the channel in indicated. The core of this water at this point is between 50 and 150 meters with a temperature of less than -0.3°C. It would appear from other transect data (Appendix II) that this cold water is discharged from the mouth of the Saint-Pierre Channel and spreads out and decreases in velocity as it moves upchannel.

The flow of the Labrador Current into Hermitage Channel occurs as a buoyancy-driven flow similar to that observed by Hamblin and Carmack (1978) in Kamloops Lake in British Columbia. In that situation river water enters a lake entraining lake water thereby reaching a depth of neutral buoyancy. The Coriolis effect causes the flowing water to move to the right thereby hugging that side of the lake. The situation in Hermitage Channel is similar in that Labrador Current Water entering Hermitage Channel is much less dense than underlying Modified Slope Water and therefore overrides it and flows up the channel following the right hand side of the channel.

The dynamic topography of the 50 kPa surface was computed relative to 2000 kPa following Fomin (1964) and is shown in Figure 4.4. The upper level was chosen to eliminate the effects of the variable surface layer. The lower level was chosen to correspond to what appeared to be a level

of minimum cross channel slope in the isopycnal surfaces and to permit comparison with earlier work (Kudlo and Burmakin, 1972). Because the survey took two days to complete some aliasing might be expected in the data. The mean difference for four repeated stations (numbers 30,36,40 and 44) was 0.012 dynamic meters. The mean error of 0.012 dynamic meters is just over twice that of the contour interval, 0.005 dynamic meters. This suggests that aliasing is a significant problem, although, if one removes the difference observed at station 44 then the mean becomes 0.008 dynamic meters. Aliasing is clearly a problem, although it does not seem to obscure a general trend which is apparent in the dynamic topography plot of Figure 4.4.

The outflow of Labrador Current Water from the mouth of Saint-Pierre Channel is clearly evident in the dynamic topography. Interpreting the contours of dynamic height as streamlines, this outflow appears to be deflected to the northeast and spread laterally as it slows down. This agrees well with the observed water distribution in the transect plots. A thick core of cold water appears to spread out and become warmer in sections successively further up Hermitage Channel beyond the Saint-Pierre Channel outflow point (Figure 4.3 and Appendix II).

Flow in the region of the mouth of the channel is quite weak and, within the CTD grid used here, rather ill defined, although, the data do suggest inflow on the southwest side and outflow on the northwest side at the mouth. The flow in the region of the head of the channel is also rather difficult to interpret. Towards the head of the channel there are some aspects of the flow, particularly the question of the flow towards Fortune Bay, that the CTD grid does not resolve.

It is also possible to compute the transport of the Labrador Current in the channel with the use of the dynamic height data. The result will

be used later in comparison with the inflow of Labrador Current Water into Fortune Bay in an attempt to compute the total transport through Saint-Pierre Channel. We can use a simple formula to compute the flow speed between two stations across the Labrador Current Water in the channel. From Pond and Pickard (1978) we find:

$$(4.1) \qquad V\ (m\ s^{-1}) = \frac{10}{Lf}\ (D_1 - D_0)$$

where V is the speed, L the distance between stations, f the Coriolis parameter, D_1 and D_0 the dynamic height in dynamic meters at the two stations. Using equation (4.1) the velocity between stations 40 and 41 is 0.14 m s^{-1}. This gives the mean flow of the water between 5 and 200 meters. It probably represents an underestimate of the flow speed within the core of the cold water. The cross sectional area of the water within the -.3°C isotherm (Figure 4.3) is 3.7×10^5 m^2 which gives a transport of 5.2×10^4 m^3 s^{-1}. It was not possible to compute the velocity in the core directly using dynamic heights so it is expected that this estimate of the transport in the cold core will be low.

The use of the geostrophic method is often fraught with traps, particularly so when it is applied on or near shelves. Several different approaches to this problem have been suggested (Reid and Mantyla, 1976; Csanady, 1979) none of which have proved entirely satisfactory. In this situation, for example, it may be possible to argue that some of the slope of the isopycnals evident in Figure 4.3 is a result of negatively buoyant flow and not geostrophic flow. This would mean a reduction in the transport calculation given above should be made.

The June 1983 survey showed quite a different picture with no clear pattern at all in the 50 to 2000 kPa dynamic height plot. The outflow of Labrador Current Water into the channel was greatly

reduced with no water < 0.0°C being observed. This corresponds with the observation outside the Saint-Pierre sill where the minimum water temperature was found to be about -.2°C. The inflow into Fortune Bay of cold dense water at the Saint-Pierre sill was also very much reduced. The conclusion is that the transport of Labrador Current Water through Saint-Pierre Channel was much lower than that for the previous year.

4.2 Saint-Pierre Channel

Saint-Pierre Channel is an extension of Avalon Channel to which access is somewhat restricted by a shallow sill just east of Placentia Bay (Figure 1.2). Figures 4.5 and 4.6 show the water structure in the channel in cross section and along its axis. The stations shown in these two figures are plotted in Figure 1.3. Looking at Figure 4.5 it can be seen that there is cold Labrador Current Water in both the north sub-channel, which leads into Fortune Bay, and in the south one, which leads across to Hermitage Channel. The slope of the isopycnals in the northern channel indicates westward flow into Fortune Bay. Flow in the southern channel is more complex; the slope of the isopycnals downwards to the left on the south side of this section between 30 and 60 meters indicates eastward flow of warm water. On the north side of the southern channel there appears to be westward flow of cold water between 60 and meters.

The longitudinal plot(Figure 4.6) shows the outflow of cold Labrador Current Water into Hermitage Channel. It is intriguing to note the increase in temperature towards the bottom at station 62. The slope of the isopycnals indicates strong upchannel flow of this water. The field bathymetric chart obtained from the Canadian Hydrographic

Service indicates the possible presence of a sill depth of 90 meters. In drawing in the bottom and making this analysis we have ignored the possible presence of this sill.

4.3 Fortune Bay

June 1981

Figure 1.4, discussed in Chapter 1, shows the results of the June 1981 cruise. The effect of the cold water outside the Saint-Pierre sill on Fortune Bay can be seen in the cold mid-depth layer within the bay where temperatures are less than 1°C. Water deep in the bay is warm (> 1.5°C) and quite dense, 26.15. The density of the water at the Miquelon sill and rising of the isopycnals between stations 55 and 56 indicate the possibility of inflow over that sill. There is some evidence in Hermitage Channel for cold Labrador Current Water outflow from Saint-Pierre Channel although it is somewhat ambiguous. No water <0.0°C was observed in Hermitage Channel, the only evidence of cold water being the lens of < 2°C around station 44.

December 1981

Figure 4.7 shows temperature and density from Saint-Pierre across to Hermitage Channel. Conditions inside the bay have changed since June 1981. The bottom water is colder by 1°C while the density has increased by 0.05. Water outside the Saint-Pierre sill is similar to that observed there in June. A lens of cold water can be seen in Hermitage Channel between 100 and 200 meters depth. There is a well developed mixed layer with intense stratification between 50 and 200 meters in Hermitage Channel. As in June, Fortune Bay once again exhibits weak stratification below 150 meters.

Figure 4.8 shows the transect across the Sagona sill in December

1981. This is the shallowest of the three sills having a limiting depth of only 100 meters. The difference in stratification between the bay water and that across the sill is strong. Water dense enough to displace the bottom water is present only 30 meters below sill depth. In spite of this there has been no direct evidence that dense water inflow occurred at this sill. If there were inflow, a significant amount of mixing would be expected since the slope inside this sill is β^{o} which is about twice that of the Miquelon sill and five times that of the Saint-Pierre sill. (This will be discussed in more detail in Chapter 5). The water in the bay from the mouth up to station 7 appeared uniformly warm to the bottom. No cross or long bay transects were run at this time.

February 1982

Temperature and density over the Miquelon sill are plotted in Figure 4.9 for the February 1982 cruise. The temperature of the deep water was higher than in December 1981. The bottom temperature was > 1.°C, with a density of 26.38. Warm and very dense water was observed near the bottom at station 55 on the Miquelon sill. The water there was 4.1°C with a density of 26.88. The depression of the 27.0 isopycnal and 5°C isotherm on the Hermitage Channel side of the sill suggest that the influx of warm water into the central depression on the sill had occurred earlier. An extra station was inserted between the sill and station 8 in the bay to see if a density current flow could be detected. In spite of the fact that no warm water inflow was observed directly it was apparent that such an inflow had just occurred.

May 1982

Figure 4.10 shows the density and temperature transects across the Saint-Pierre and Miquelon sills. The bottom water towards the mouth of

the bay was now -0.27°C with a density of 26.23, 0.15 kg m^{-3} less than that observed in February. The slope of the isotherms and isopycnals leading into the bay and over the Saint-Pierre sill indicate that cold water inflow was occurring. There is still comparatively warm water in the depression on top of the Miquelon sill with temperatures greater than 1°C and densities greater than 26.5. Even at this time when strong cold water inflow is occurring at the Saint-Pierre sill there is water at the Miquelon sill dense enough to replace the bottom water in the bay.

Figure 4.11 shows the temperature and density along the bay in May 1982. The water towards the head of the bay is remnant warm water left over from the winter exchange. It has a maximum temperature of 2.46°C and density of 26.4. Even the water deep inside Belle Bay over the 193 meter sill is warm and dense, though the temperature does decrease towards the bottom. The rising of the 0°C isotherm towards the back of the bay is consistent with the presence of the cold water inflow. Cold water enters the bay over the Saint-Pierre sill and then rides up over the denser warm bottom water, which is gradually eroded and eventually replaced.

Figure 4.12 shows temperature and density across the Sagona sill. The weak stratification of the bay water compared with that outside is once again apparent. Warm dense water capable of replacing the bottom water of the bay is present just below sill depth.

Analysis for nutrients at selected depths was carried out in May 1982. Figures 4.13 and 4.14 show the results of this work together with that of some work done in June 1982 for dissolved oxygen. Dissolved oxygen was not done earlier because a kit for doing the analysis was not available before June. For simplicity we will discuss the results of both surveys together.

The nutrient analysis shows the Modified Slope Water to be high in total nitrogen, silicate and phosphate. The maximum values observed in the Modified Slope Water are about twice those observed for the Labrador Current Water. At each level the two water masses show fairly constant nutrient concentrations. Local stations do show anomalous nutrient values for example, the high nitrate and silicate values observed at 50 meters depth at station 36.

The results of the dissolved oxygen survey show that not even the surface water reaches saturation level. The levels are presented in ml/l^{-1} but the highest values represent a saturation of about 70% (Strickland and Parsons 1972, Table XIV). Three stations were observed to have low oxygen concentrations at the bottom, stations 53, 51 and 3. The concentration at these stations was 5.50, 4.46 and 5.92 ml/l respectively. It appears that the low oxygen concentrations are associated with the Modified Slope Water. No stations were found to be anoxic. Oxygen levels of the inflowing Labrador Current Water over the Saint-Pierre sill were found to be uniformly high, greater than 8 ml/l.

The low oxygen level at station 3 can be used as a qualitative measure of the residence time of the warm water found there. It will later be shown that the inflowing Modified Slope Water mixes 40/60 with the bay water so that when it reaches the bottom of the bay it should have an oxygen concentration of about 7 ml/l. From its time of entry the bottom water has thus decreased in oxygen by about 1 ml/l.

June 1982

A transect run in June 1982 along the axis of the bay is shown in Figure 4.15. Cold water observed in May 1982 was observed to advance

further up the bay. Dense water inflow was still occurring and was observed with a current meter mooring placed just inside the Saint-Pierre sill. Data from the mooring will be discussed in Chapter 5.

Near-surface waters in the bay have increased in temperature. The maximum temperature observed was greater than 7°C compared to 5°C in May 1982. In this transect the conditions outside the Saint-Pierre sill appear unchanged. Station 11, occupied one week earlier, showed quite different conditions: the bottom temperature was -.48°C with a density of 26.26. This indicates the short term variability in the bottom waters at station 9. The thickness and position of this lens is unchanged from May 1982.

Comparing the density plots (4.11)and (4.15) there is less stratification in the bay water in June as a direct result of the inflow of Labrador Current Water. This inflow has also decreased the bottom water temperatures at station 3 outside Belle Bay by about 0.5°C. The density there has decreased by 0.06 kg m^{-3}. These changes over a period of about three weeks are quite significant and indicate how quickly the dense water at the head of the bay can be eroded.

The warming of the near-surface water mentioned earlier has extended to 100 meters. This is most easily seen by looking at the depression of the 0°C isotherm. This represents heating of the winter cooled surface water of the bay. Winter cooling and wind mixing of the water in the bay were unusually severe in 1982. Advection of cold water into the bay over the Saint-Pierre sill in the winter is another source of the cold water observed in the upper 150 meters of the bay in February 1982.

Figure 4.16 shows the temperature and density profile from the Saint-Pierre sill across to Hermitage Channel. The temperatures at the Miquelon sill were not noticeably lower than in May (Figure 4.9). Cold

to override the warmer and denser water. Figure 4.17 shows the 26.22 isopycnal sloping upwards to the right and the 26.24 isopycnal sloping upwards to the left indicating the movement of the cold water in this mid-depth layer is also towards the head. By 14 June the warm bottom water has been replaced by the headward flowing cold water.

The inflow thus drives a net flow of cold water up the bay. The preferential path for the cold water flow is through the southeastern channel because of the influence of the Coriolis force; or through the northwestern channel during conditions of strong inflow, because it is deeper.

July 1982

A short survey of the bay was conducted in July 1982 by NAFC personnel on our behalf. Temperature is the same as for June. Cold water inflow is still taking place as shown by the very cold dense water observed at station 9.

The 0°C isotherm has advanced still further up the bay, now extending as far as station 7. The warm bottom water at station 6 has cooled considerably to -0.2°C. The indirect effects of solar heating and wind mixing are evident in the further depression of the 0°C isotherm to below 150 meters and the warming of the surface water to 11 to 12°C. Very cold dense water is still present outside the Saint-Pierre sill.

November 1982

The last survey to be discussed was carried out in early November 1982. Figure 4.20 shows the temperature and density plotted from outside the Saint-Pierre sill to Hermitage Channel. Conditions outside in the Saint-Pierre Channel have changed greatly since the summer; the water temperature at or below sill depth being some 0.5°C with a density of 26.43. The water in the depression on the Miquelon sill, although

water appears at this point to be running over the Miquelon sill and mixing away the warm water which was in the central depression on the sill. Water below 0°C was observed at stations 56 and 55. In spite of this outflow of cold water, warm water at the bottom of station 55 is still sufficiently dense to replace deep water in Fortune Bay. In Hermitage Channel the 27.0 isopycnal and the 5.0°C isotherm are depressed below their February (Figure 4.9) and May (Figure 4.10) 1982 positions. Cold water between stations 53 and 49, in the depth range 50 to 175 meters, is probably a result of discharge from the Saint-Pierre Channel.

Transects run along the bay such as that shown in Figure 4.15 illustrate the complexity and inhomogeneity of the deep water within the bay. Cross bay transects further illustrate the water structure in the bay by showing the differences between the two channels on either side of the central bank (see Figure 1.2). Figure 4.17 shows the results of a survey conducted on 7 June 1982. The bottom temperature in the northwestern channel was greater than zero while that in the eastern channel is below zero. The density in the northwestern channel was greater than that in the other by 0.04. Figure 4.8 shows the results of a survey conducted one week later on 14 June 1982. The temperature and density in the southeastern channel remained relatively unchanged, but the northwestern channel now contained much colder and less dense bottom water. The water on the top of Brunette Bank at 180 meters is also colder, by some 0.2°C.

The slope of the isopycnals in the northeastern channel indicate flow towards the head. The flow in this side of the bay is similar for both the 7 and 14 June, although the actual densities do change. In the northwestern channel the less dense cold water is initally forced

still comparatively warm, is less dense than the bottom water in the bay. The position of the 27.0 isopycnal and the 5.0°C isotherm below 200 meters in Hermitage Channel appear similar to that observed in June. Only a thin section of cold water, with temperatures less than 1°C, is apparent at station 49. None of the very cold water observed there in June is present.

The plot of temperature and density in Figure 4.21 shows the distribution of warm water inside the bay. The range of bottom water temperatures inside the bay is now very low, about 0.2°C. The coldest water is found at the head of the bay at station 3. The 0°C isotherm now divides the bay in much the same way as it had in the summer, except now in the opposite sense. The cold water is near the head while the warm water is found near the mouth. The cold water has even extended over the sill into Belle Bay displacing the warm water which had been observed there in May 1982. The temperature at the bottom has decreased by about 1.0°C, although the density has changed by only 0.1. It appears from this plot that the warm water which entered the bay between June and November did so over the Miquelon sill. No > 0°C bottom water in the bay was observed beyond station 6.

From Figures 4.21 and 4.22 it can be seen that the surface mixed layer is warmest (7°C) at the head of Fortune Bay. Along the axis of the bay, the mixed layer thins towards the Saint-Pierre sill (Figure 4.21). Across the Sagona sill, it initially deepens to near 100 meters and then thins, cooling towards the southwest out of the bay. This shows the effect of freshwater addition to the bay and the effect of open access to the west and southwest beyond the Sagona sill.

Figure 4.22 shows the temperature and density across the Sagona Isle sill. Water of sufficient density to displace bottom water in the bay is still present at about 50 meters below sill depth on the Hermitage Channel side.

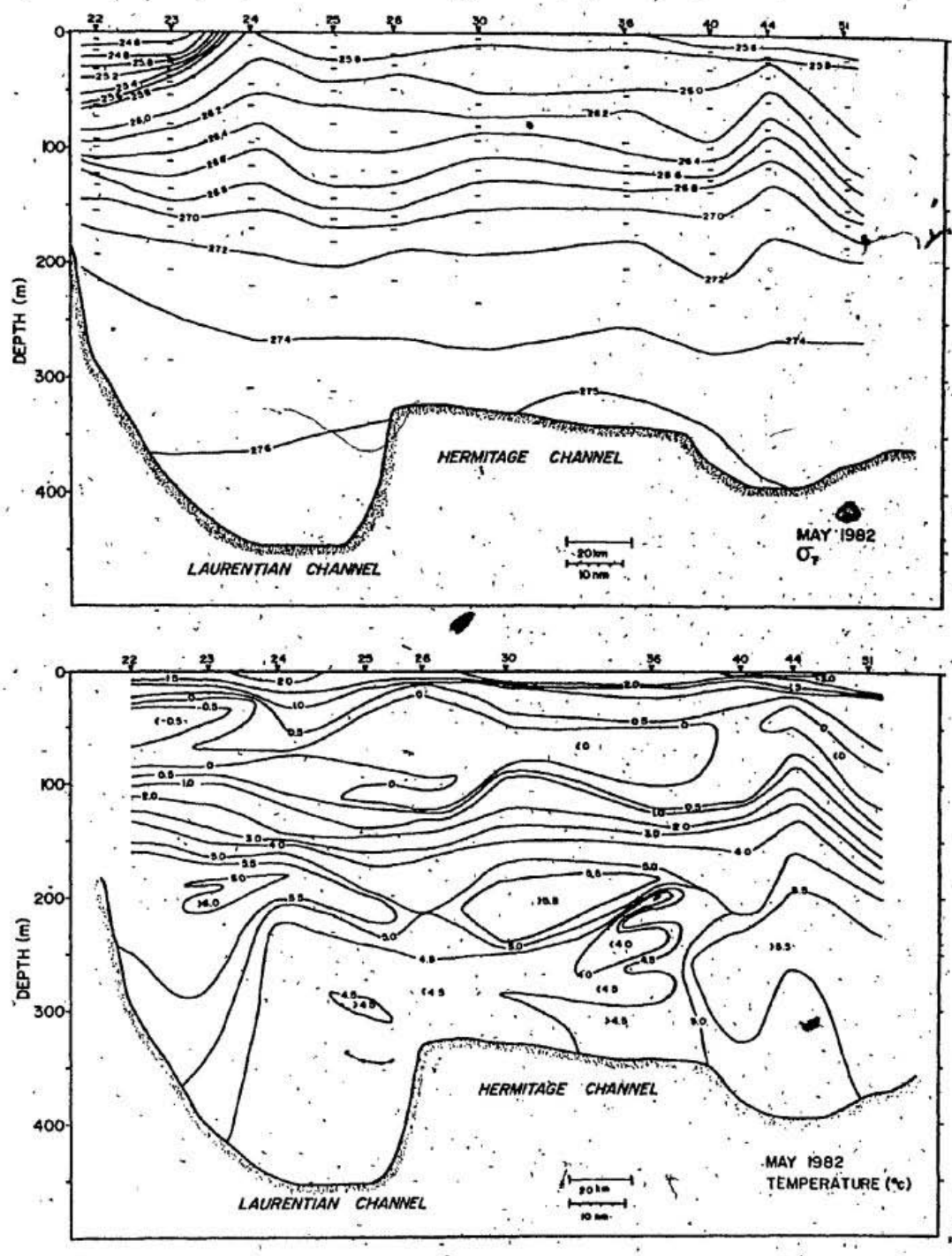


Figure 4.1 Sigma-t (density) and temperature across the Laurentian Channel and up Hermitage Channel in May 1982. Note the station numbers which are indicated along the top (1nm = 1.85km).

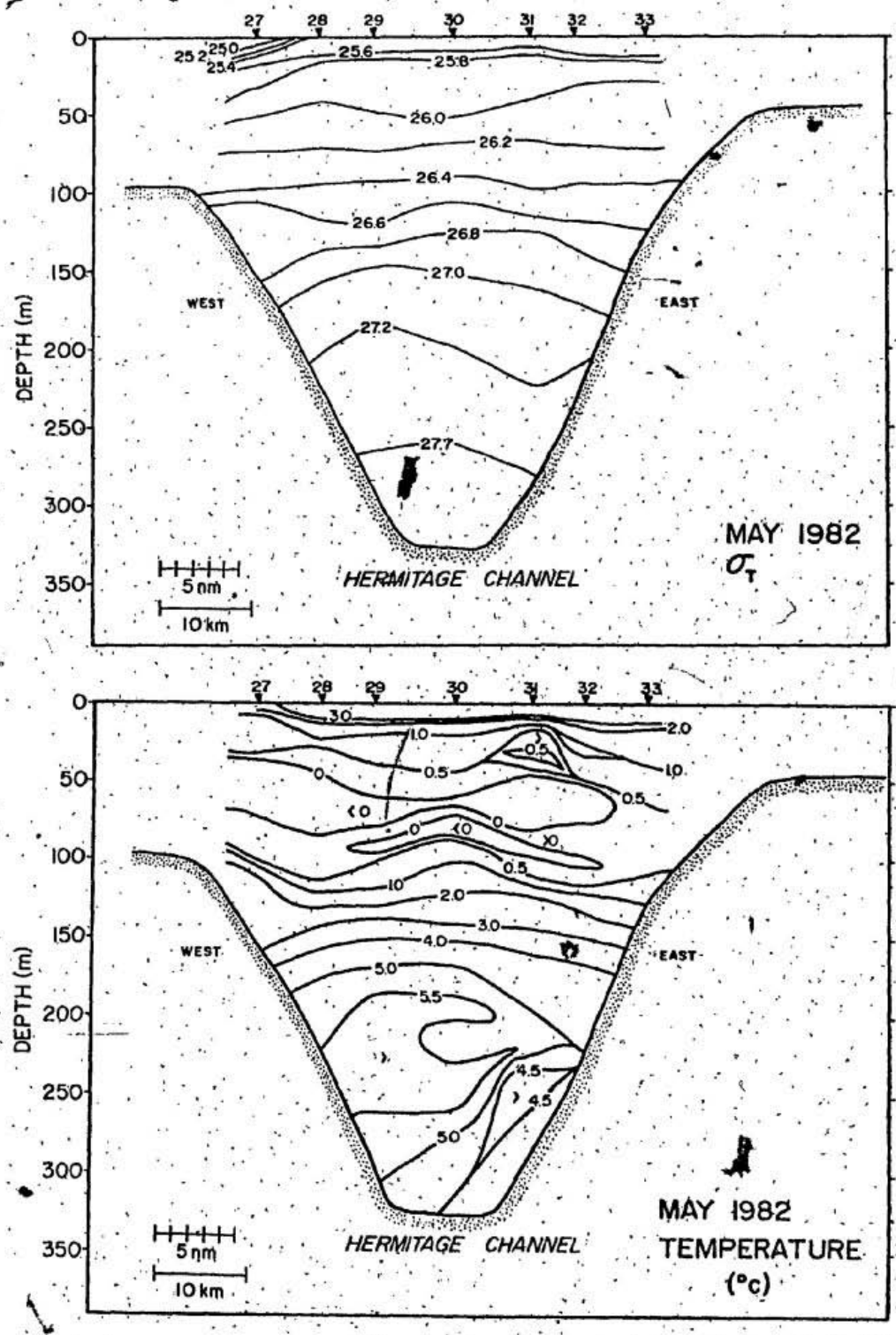


Figure 4.2 Sigma-t and temperature across Hermitage Channel, looking up the channel, in May 1982.

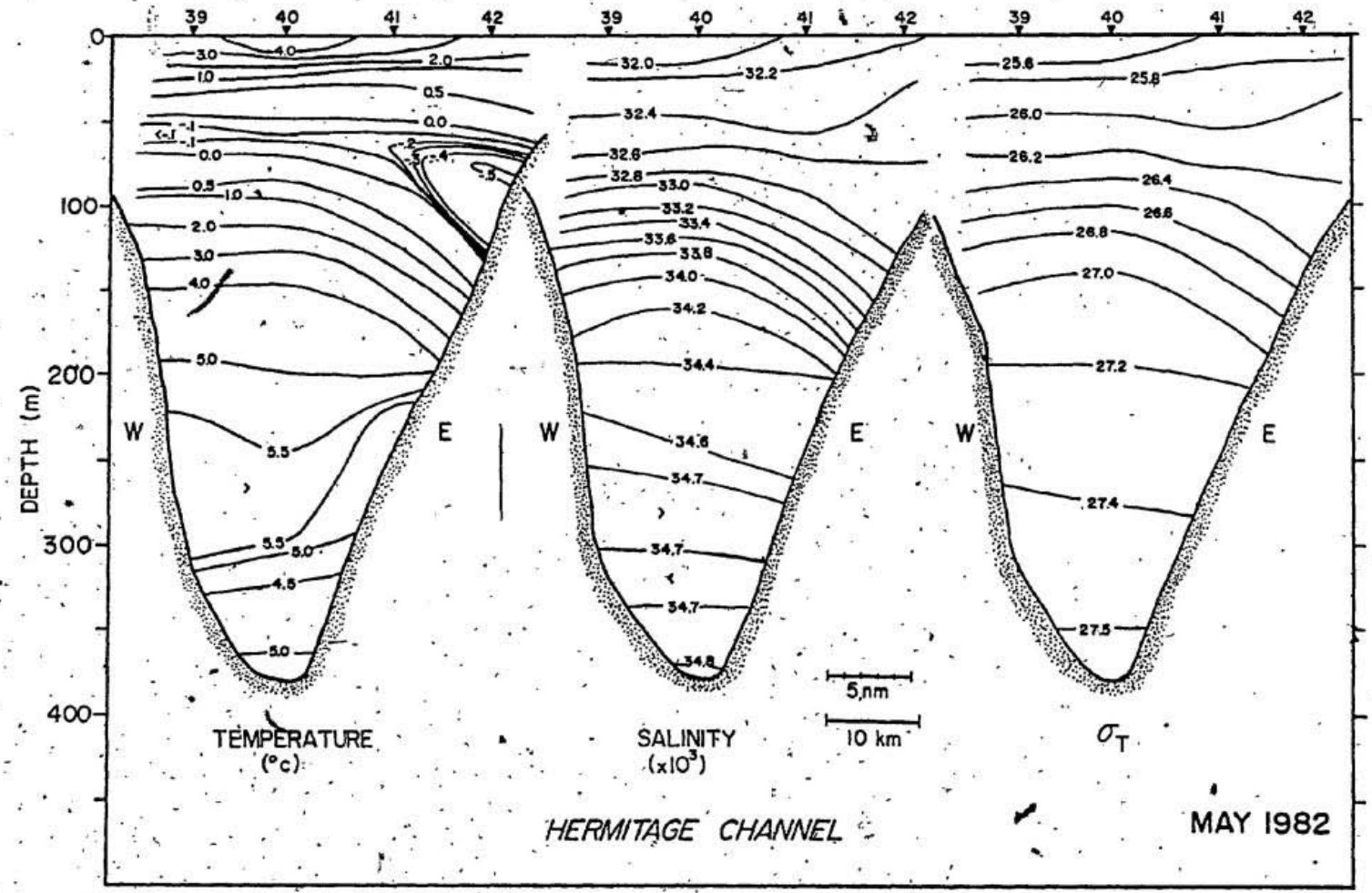


Figure 4.3 Temperature, salinity and sigma-t across Hermitage Channel, looking up the channel, southwest of Miquelon, in May 1982.

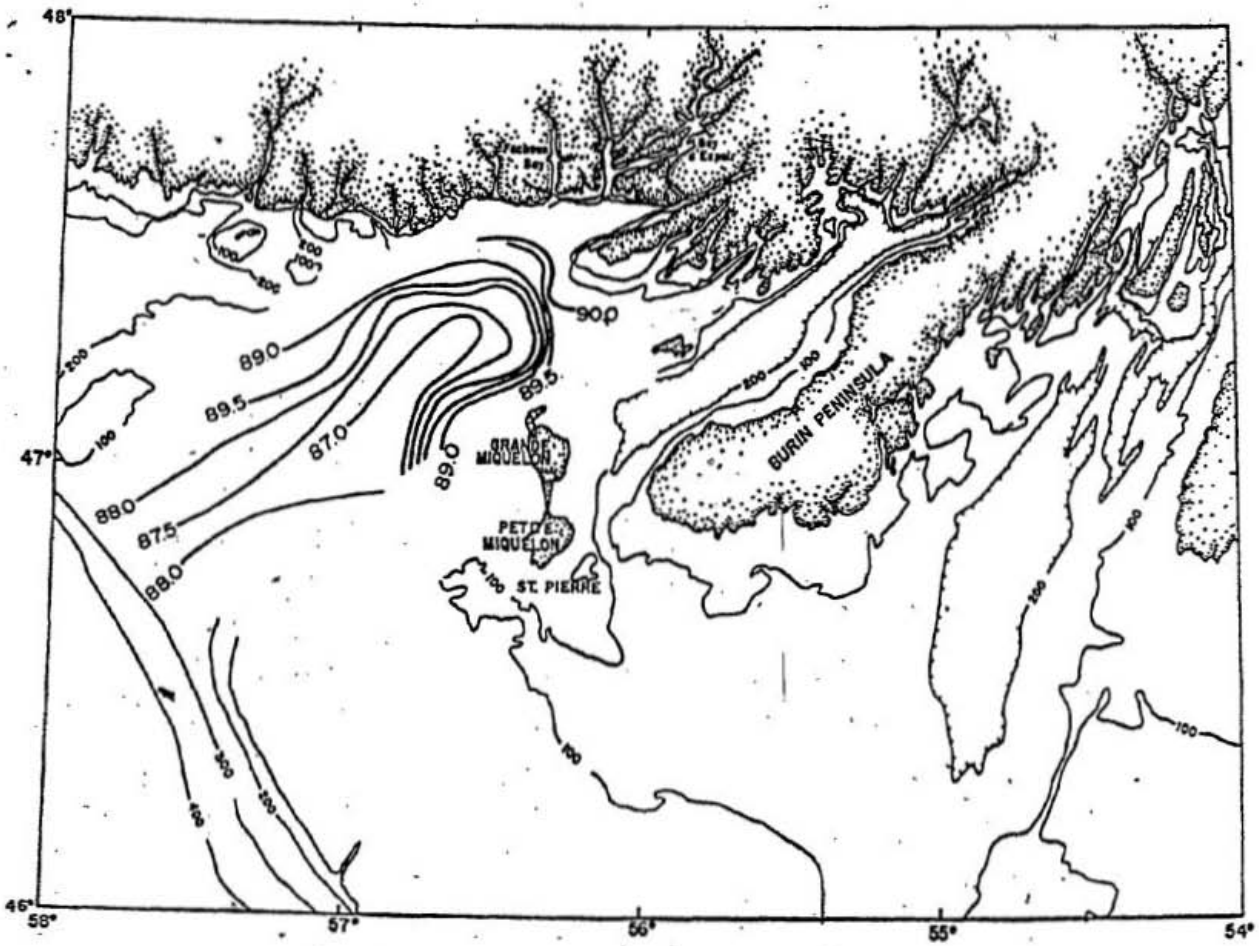


Figure 4.4 The dynamic height, plotted in units of dynamic-centimeters, in Hermitage Channel, in May 1982. The contour interval is 0.5 dynamic-centimeters.

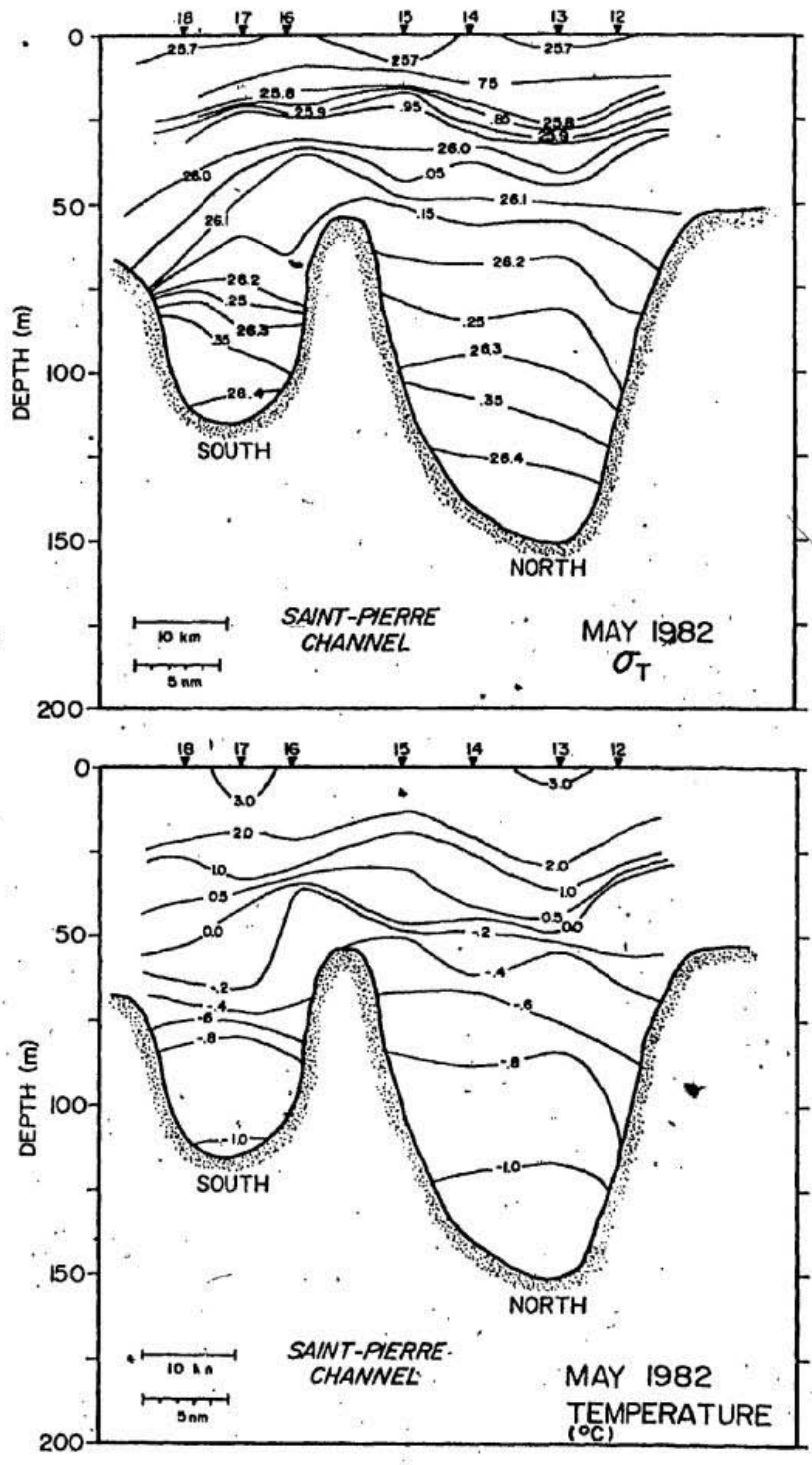


Figure 4.5 Sigma-t and temperature, plotted across the Saint-Pierre Channel, looking westward, in May 1982.

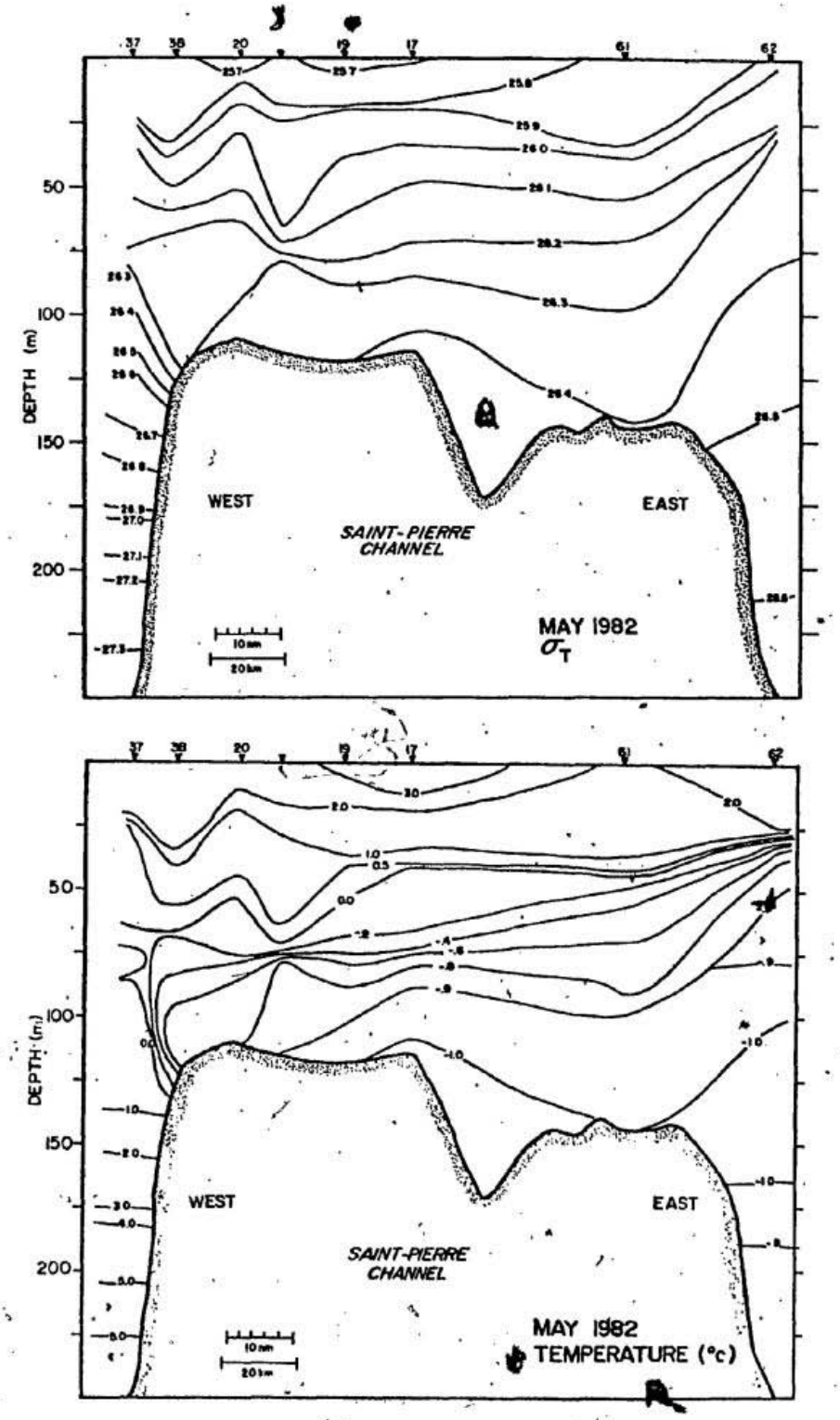


Figure 4.6 Sigma-t and temperature, plotted along Saint-Pierre Channel as far west as Hermitage Channel, in May 1982.

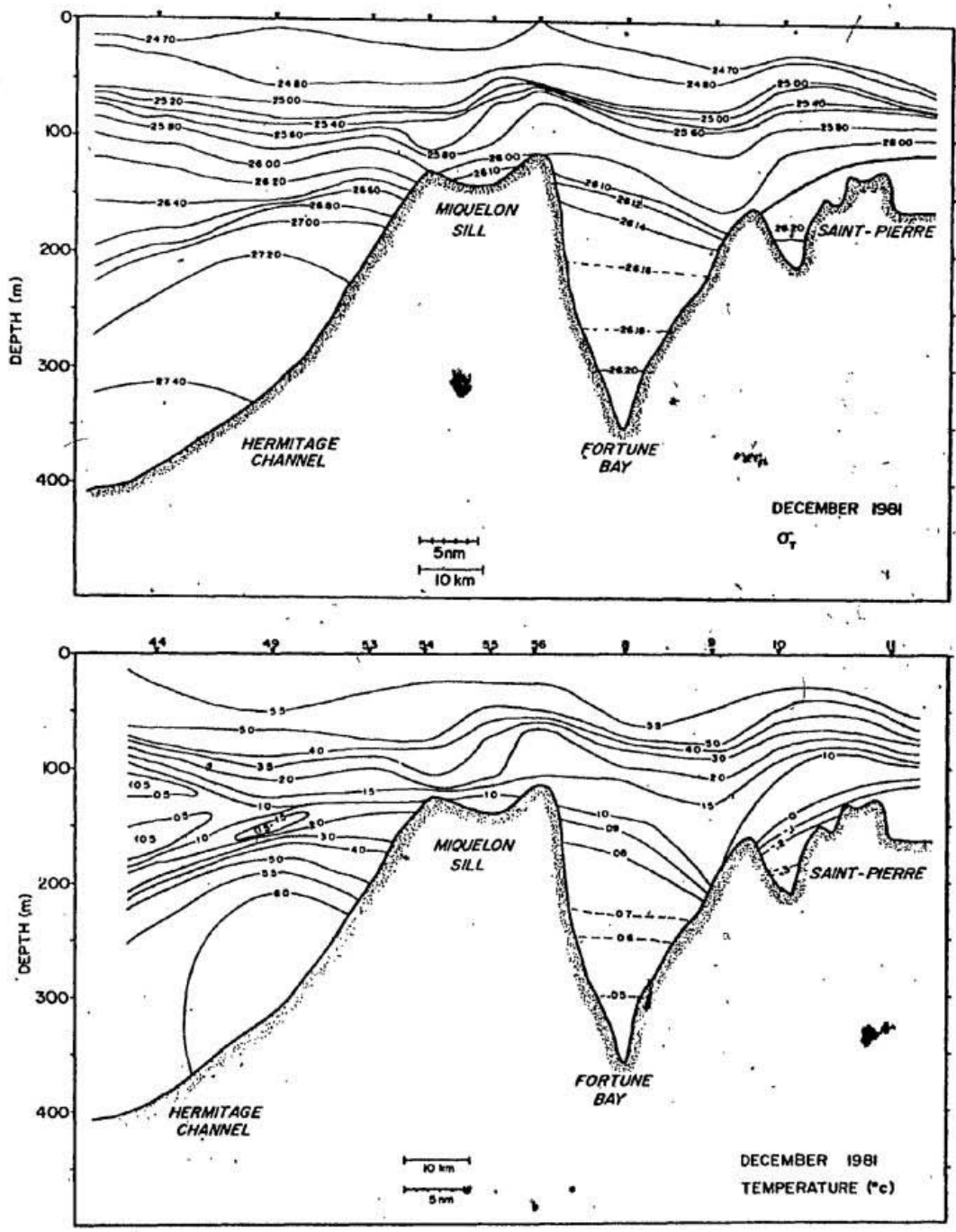


Figure 4.7 Sigma-t and temperature, plotted from Saint-Pierre across Fortune Bay to Hermitage Channel, in December 1981. The station numbers are indicated along the top of the lower figure.

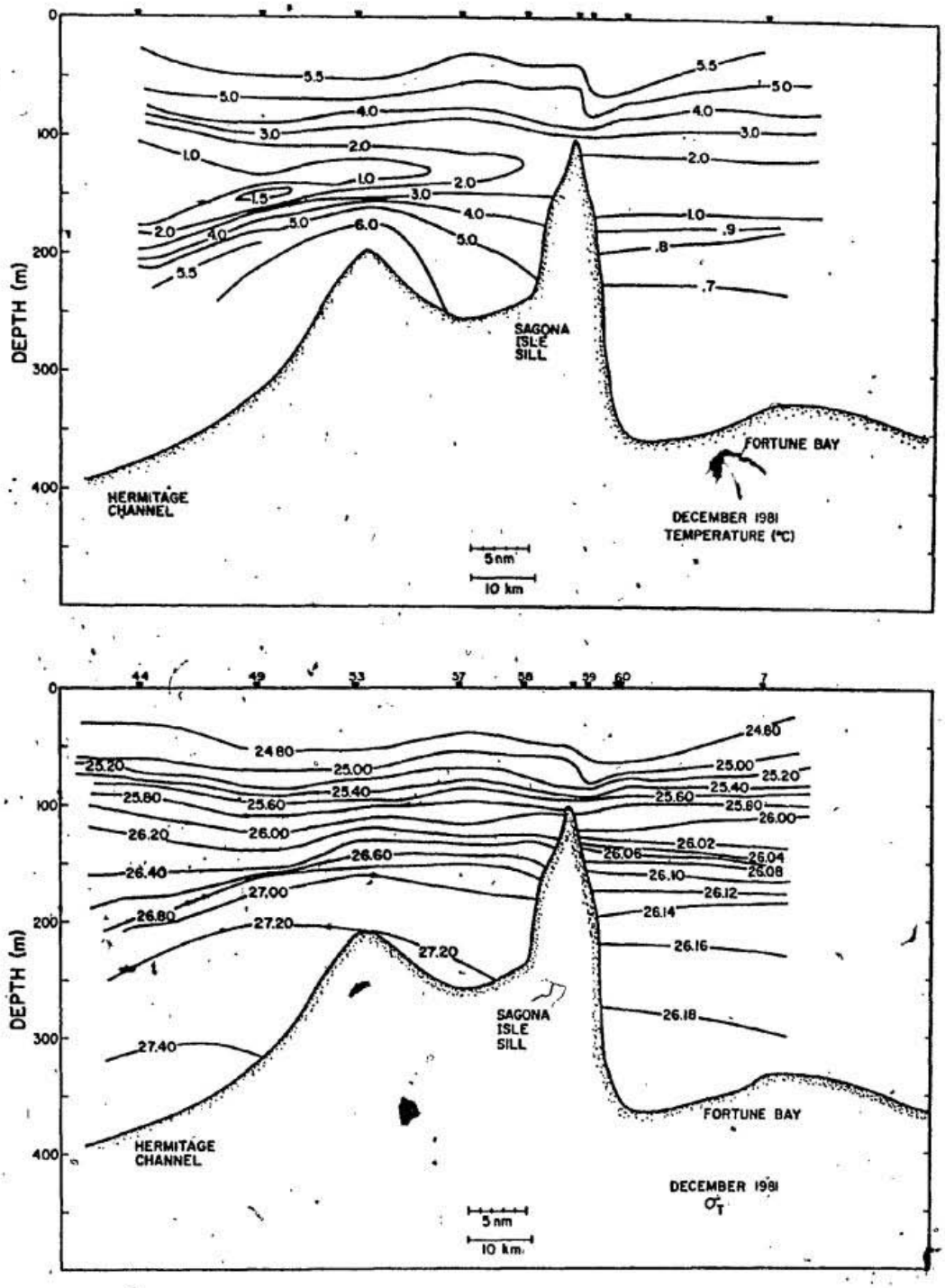


Figure 4.8 Sigma-t and temperature, plotted from Fortune Bay across the Sagona sill to Hermitage Channel, in December 1981.

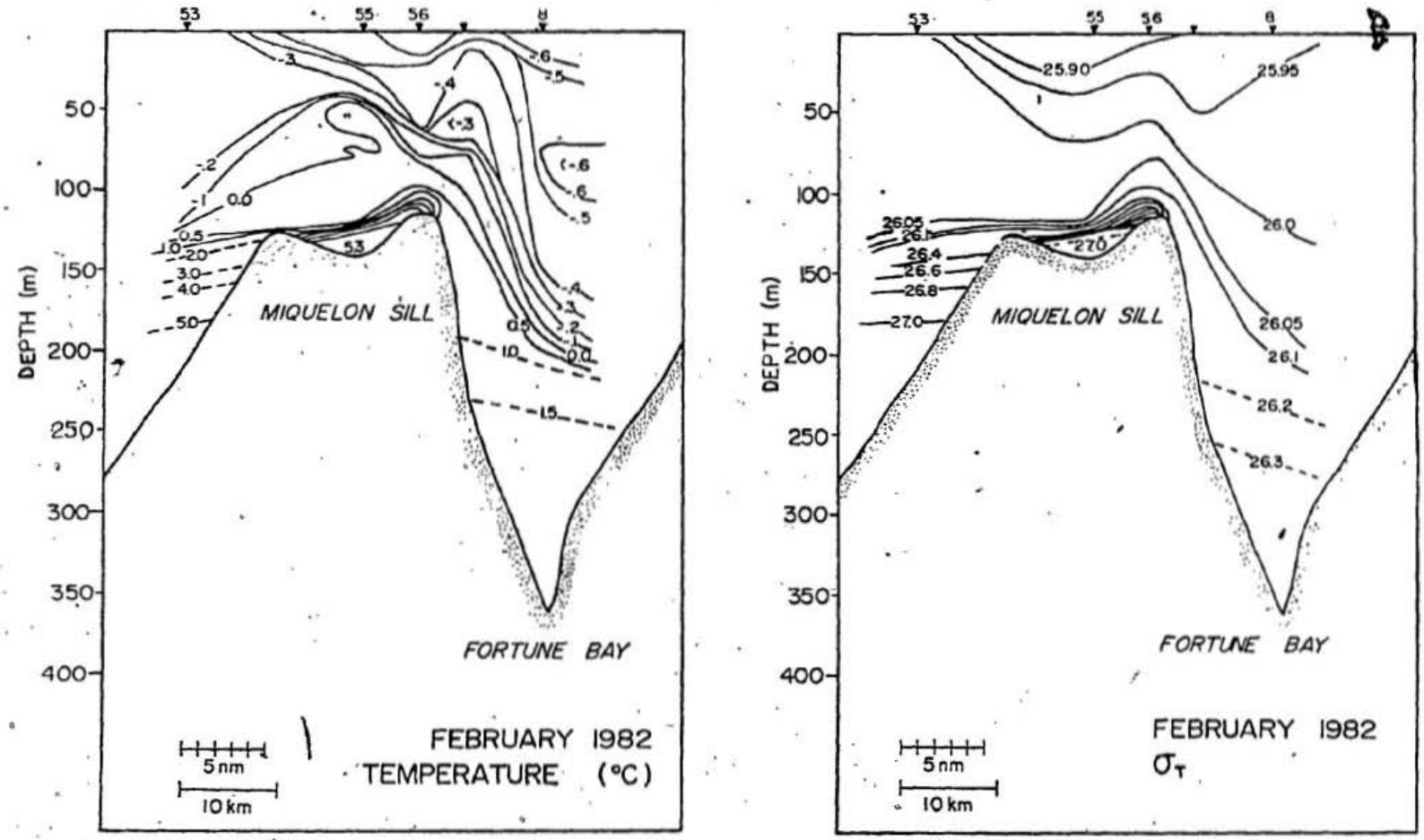


Figure 4.9 Sigma-t and temperature, plotted from Fortune Bay across the Saint-Pierre sill to Hermitage Channel, in February 1982. Note that an extra station was inserted between stations 56 and 8.

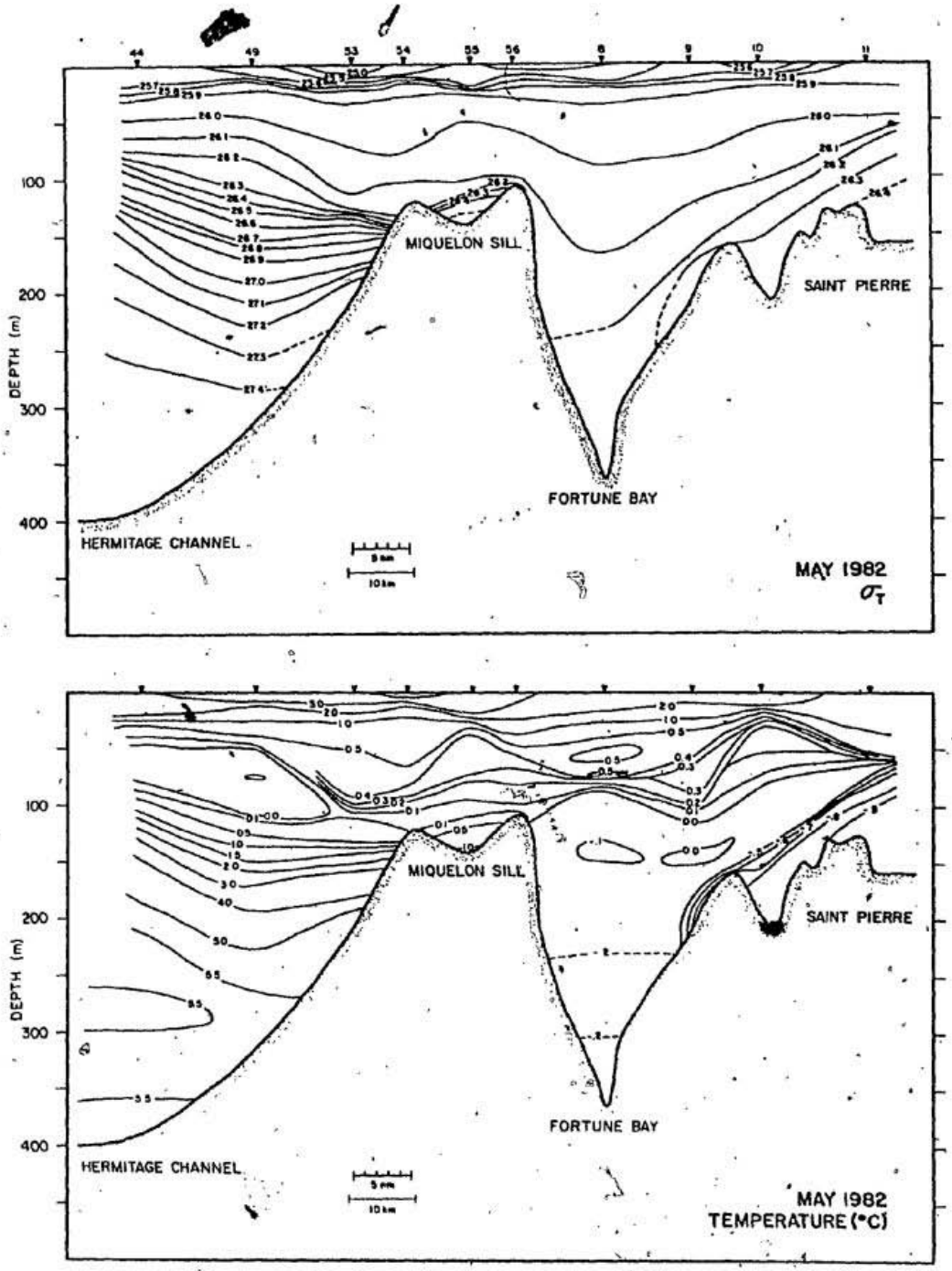


Figure 4.10 Sigma-t and temperature, plotted from Saint-Pierre across Fortune Bay to Hermitage Channel, in May 1982.

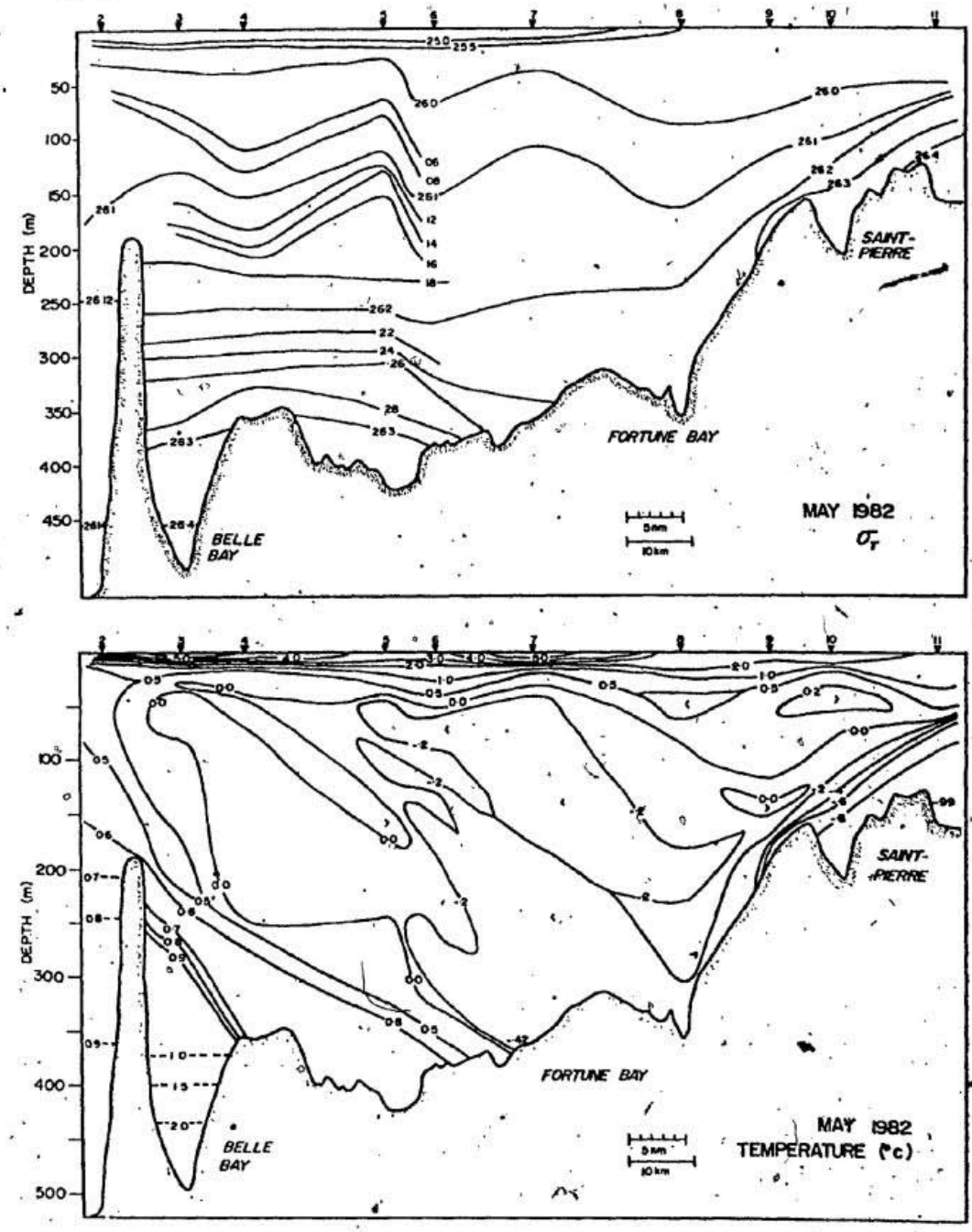


Figure 4.11 Sigma-t and temperature, plotted along the axis of Fortune Bay in May 1982.

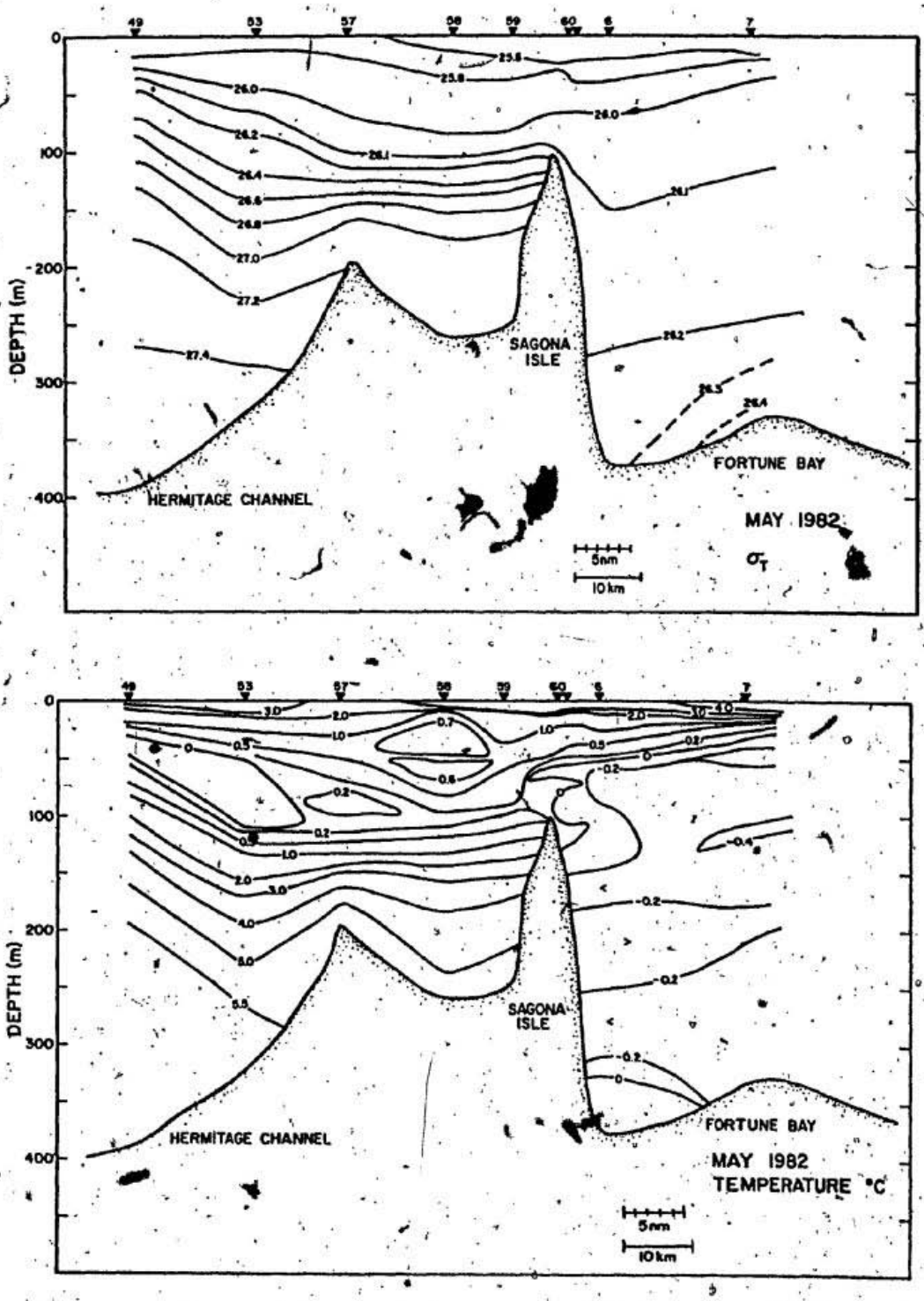


Figure 4.12. Sigma-t and temperature, plotted from Fortune Bay across the Sagona sill to Hermitage Channel, in May 1982.

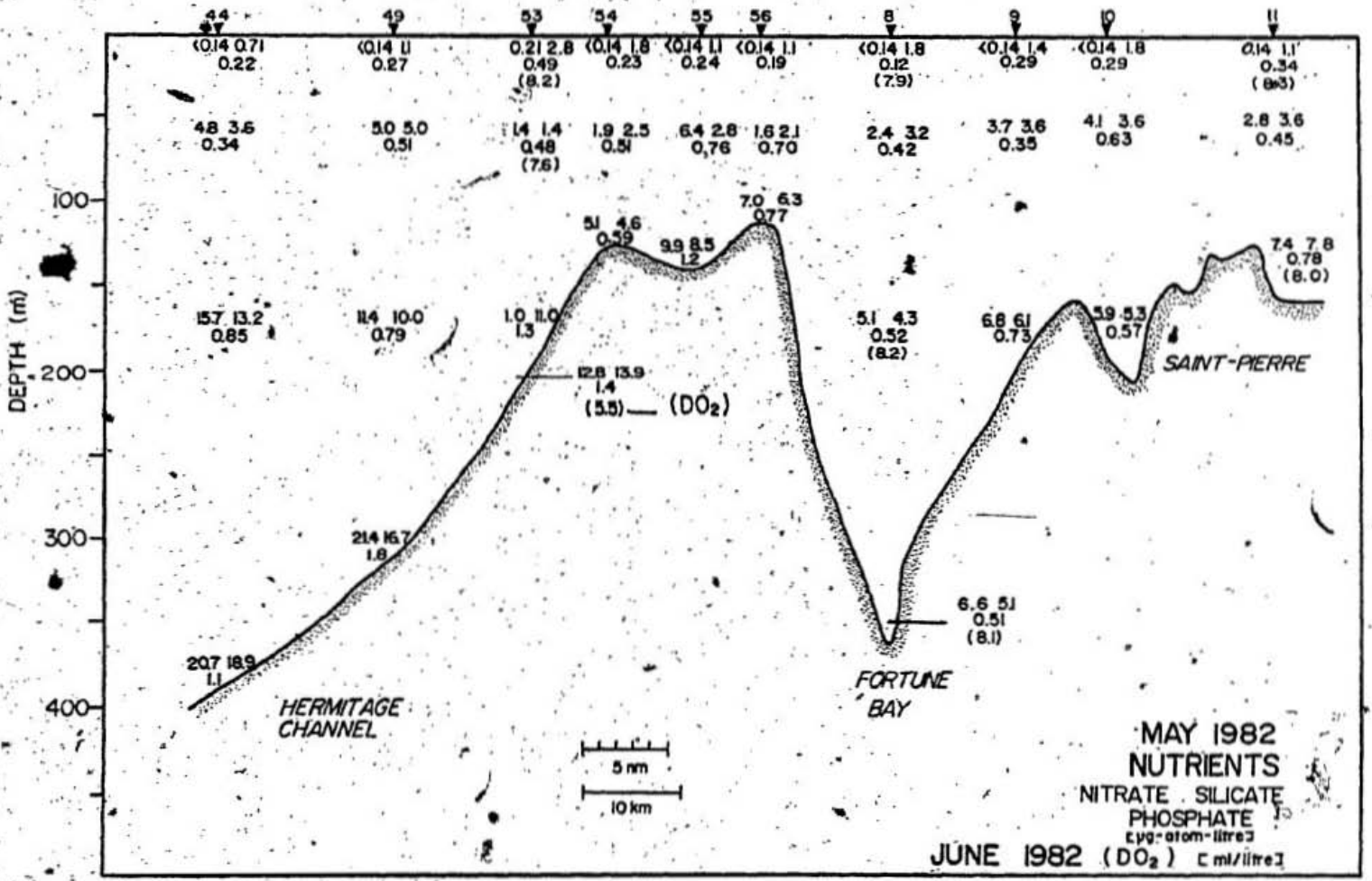


Figure 4.13 Nutrient data, plotted from Saint-Pierre across Fortune Bay to Hermitage Channel, in May 1982. Nitrate, silicate and phosphate concentrations are given in µg-atom/litre. Dissolved oxygen concentrations, measured in June 1982, are given in ml/litre.

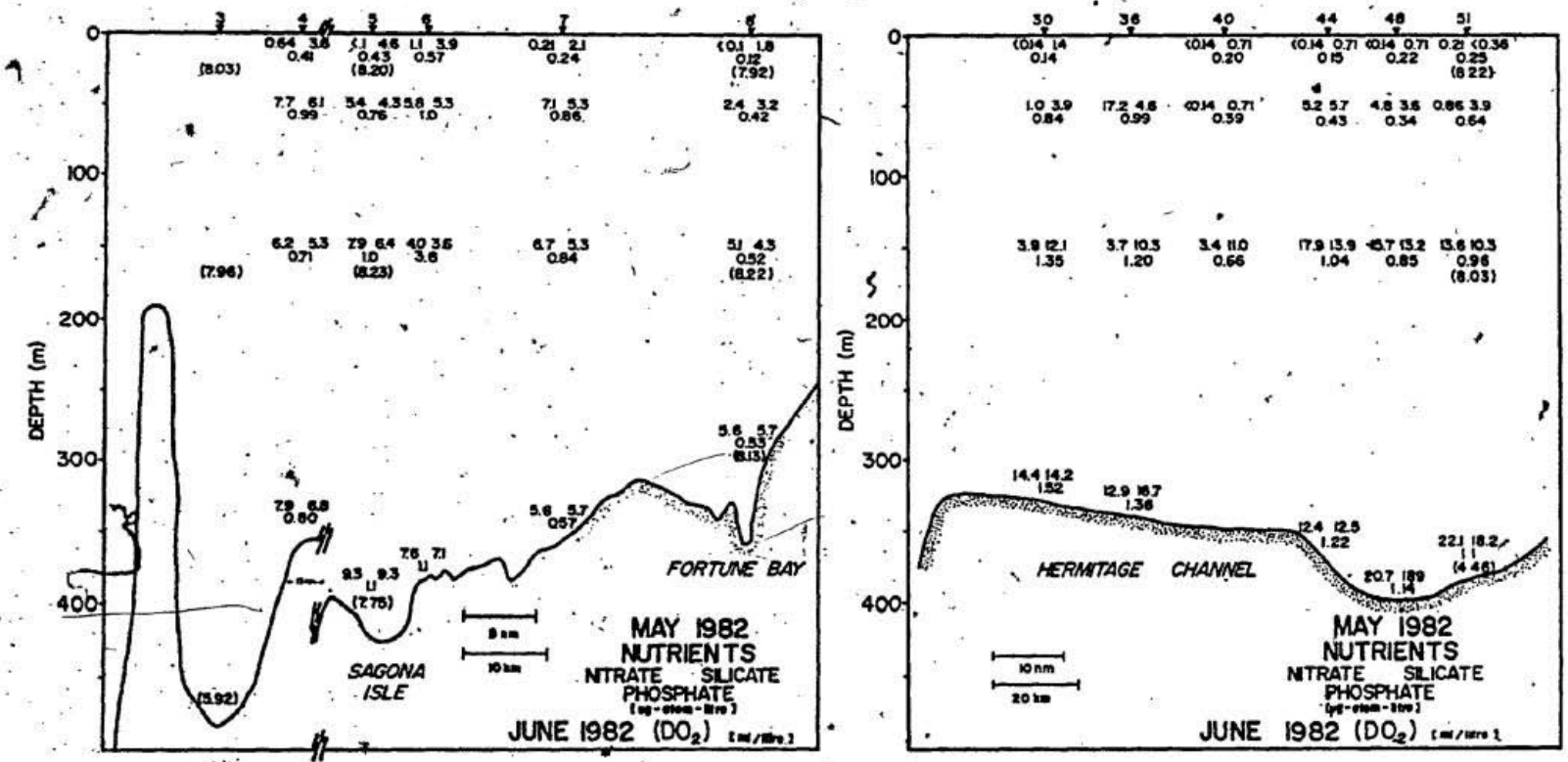


Figure 4.14 Nutrient data, plotted along the axis of Fortune Bay and Hermitage Channel, in May 1982. Nitrate, silicate and phosphate concentrations are given in µg-atom/litre. The dissolved oxygen concentrations, measured in June 1982, are given in m/litre.

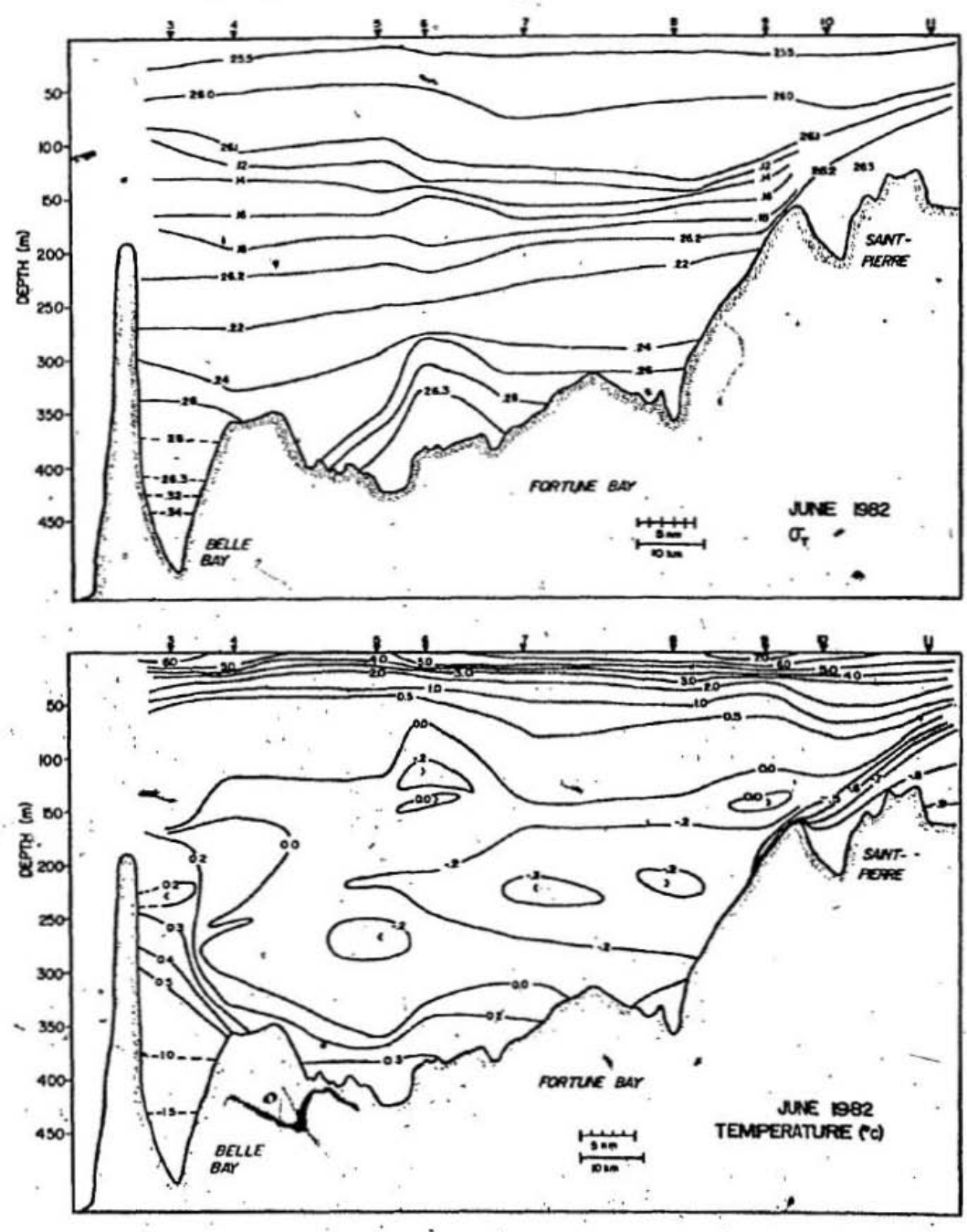


Figure 4.15 Sigma-t and temperature, plotted along the axis of Fortune Bay, in June 1982.

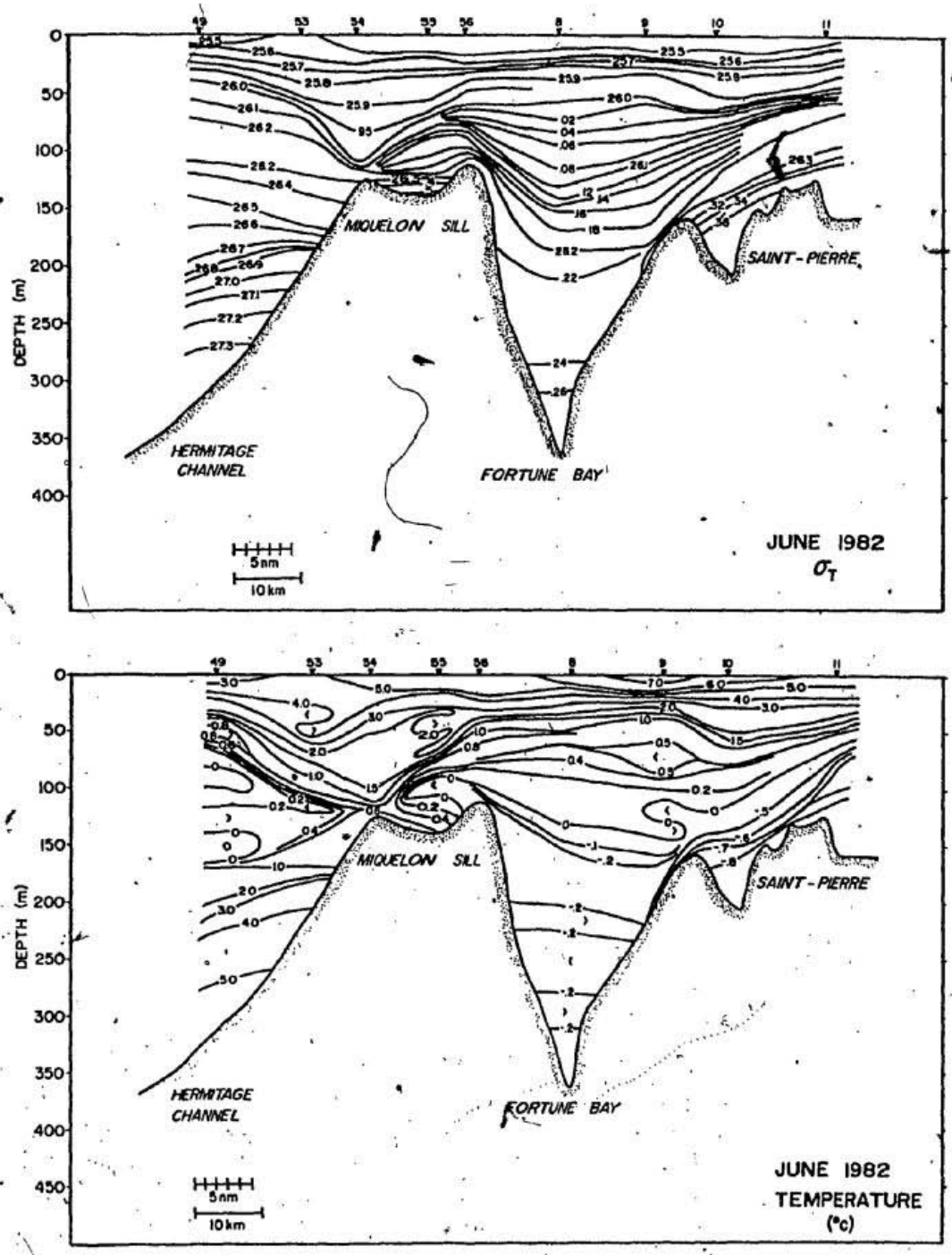


Figure 4.16 Sigma-t and temperature, plotted from Saint-Pierre Channel across Fortune Bay to Hermitage Channel, in June 1982.

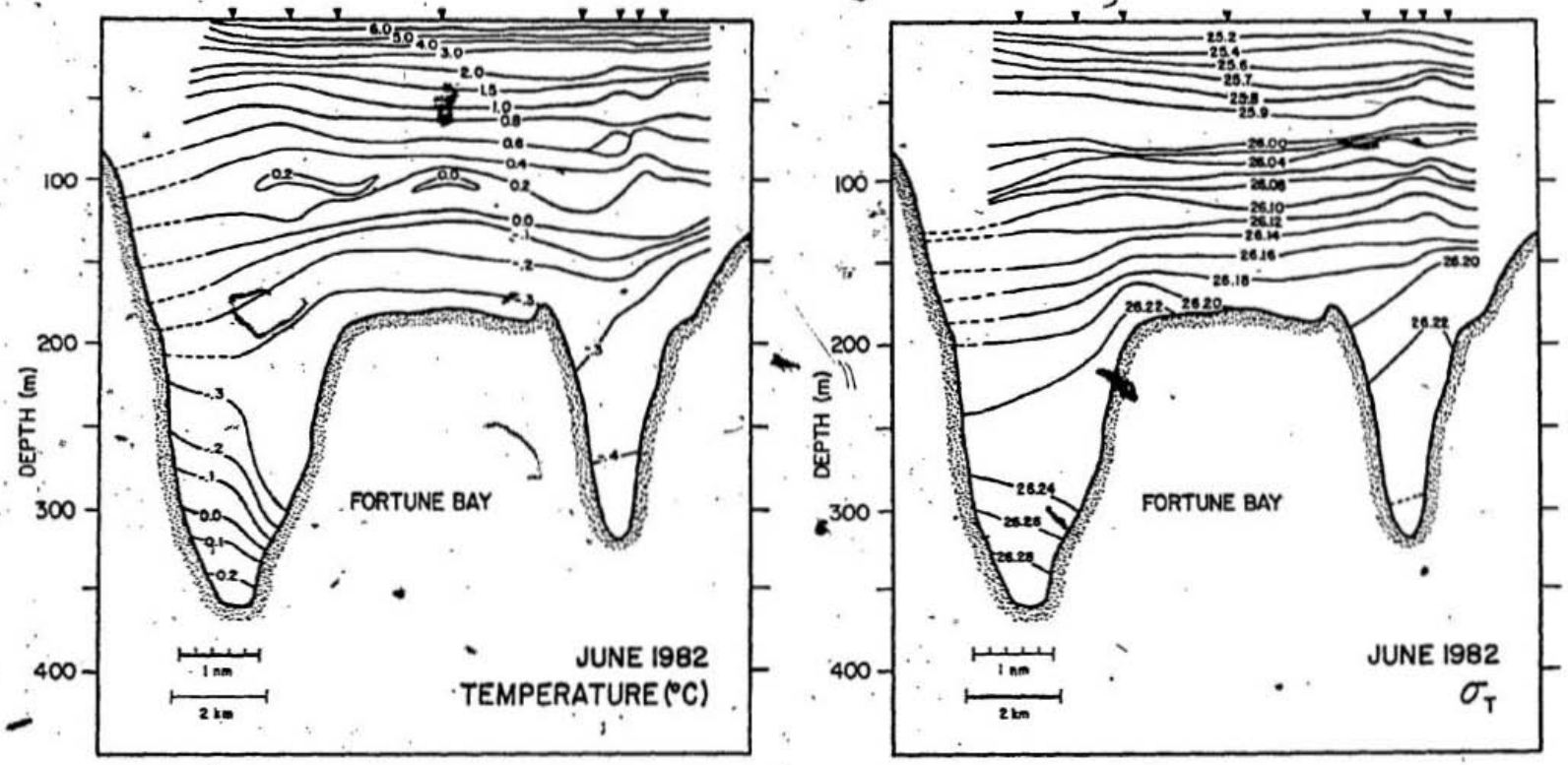


Figure 4.17 Sigma-t and temperature, plotted along transect T1, looking northeastward towards the head of the bay, on 7 June 1982.

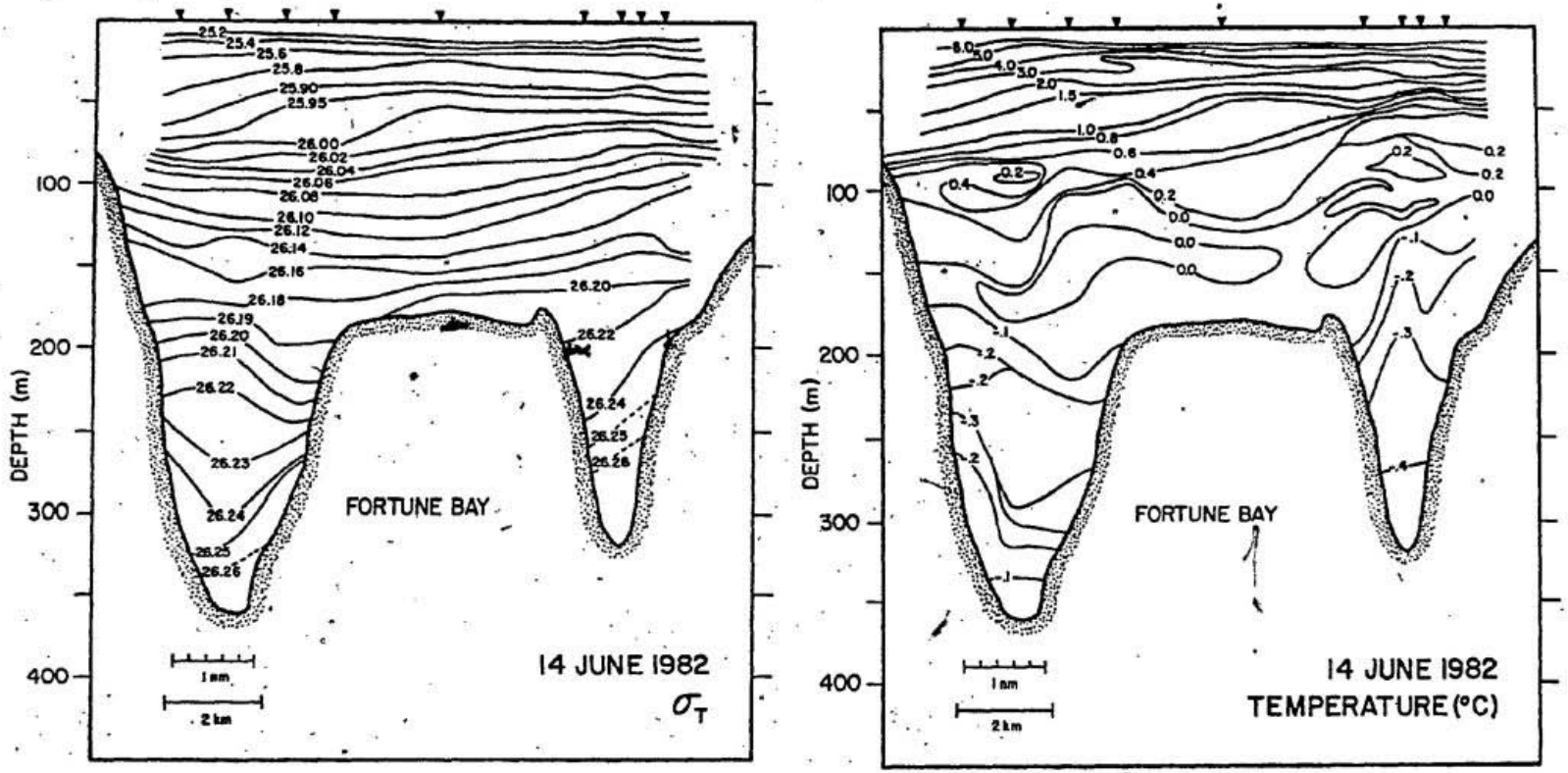


Figure 4.18 Sigma-t and temperature, plotted along transect T1, looking northeastward towards the head of the bay, on 14 June 1982.

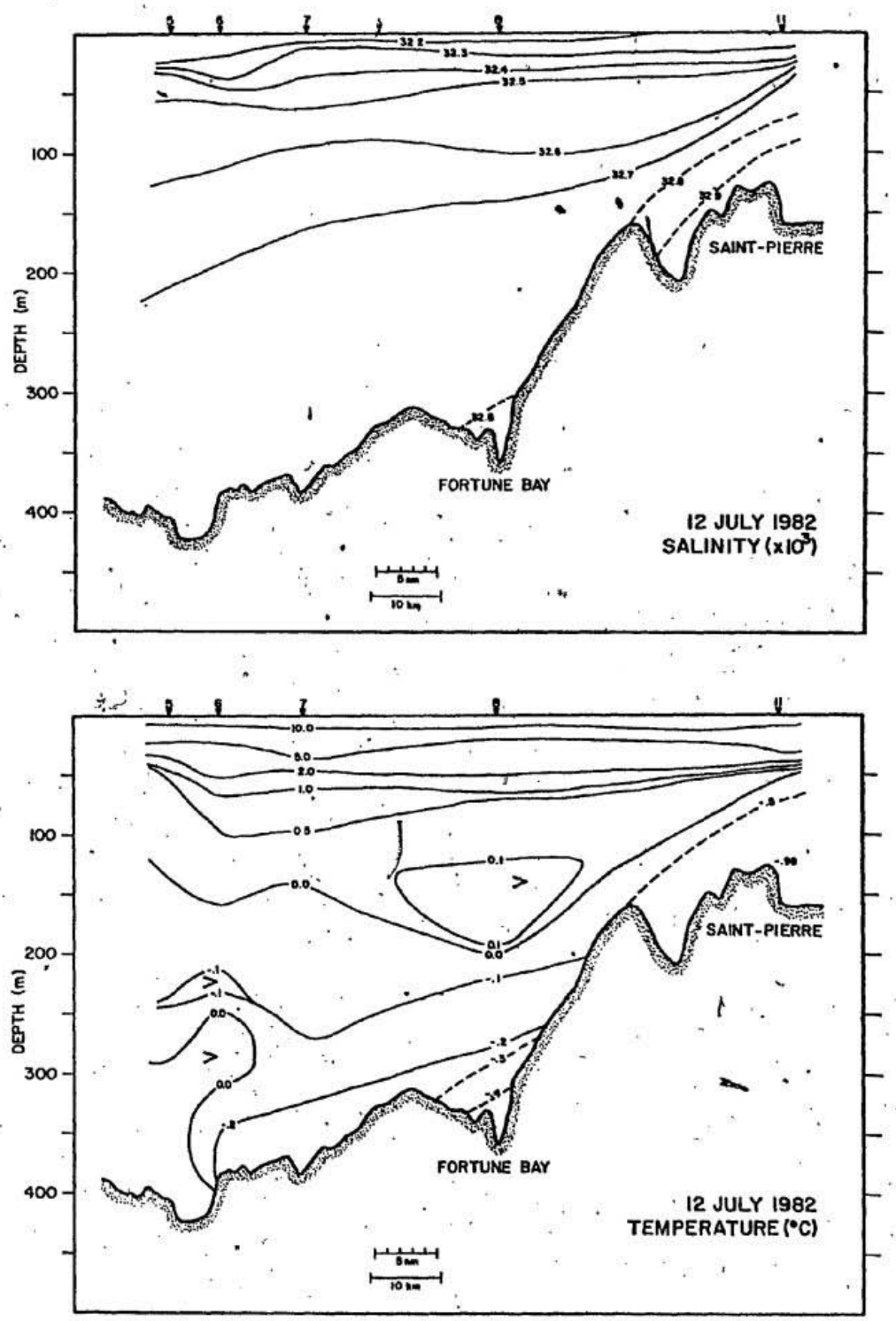
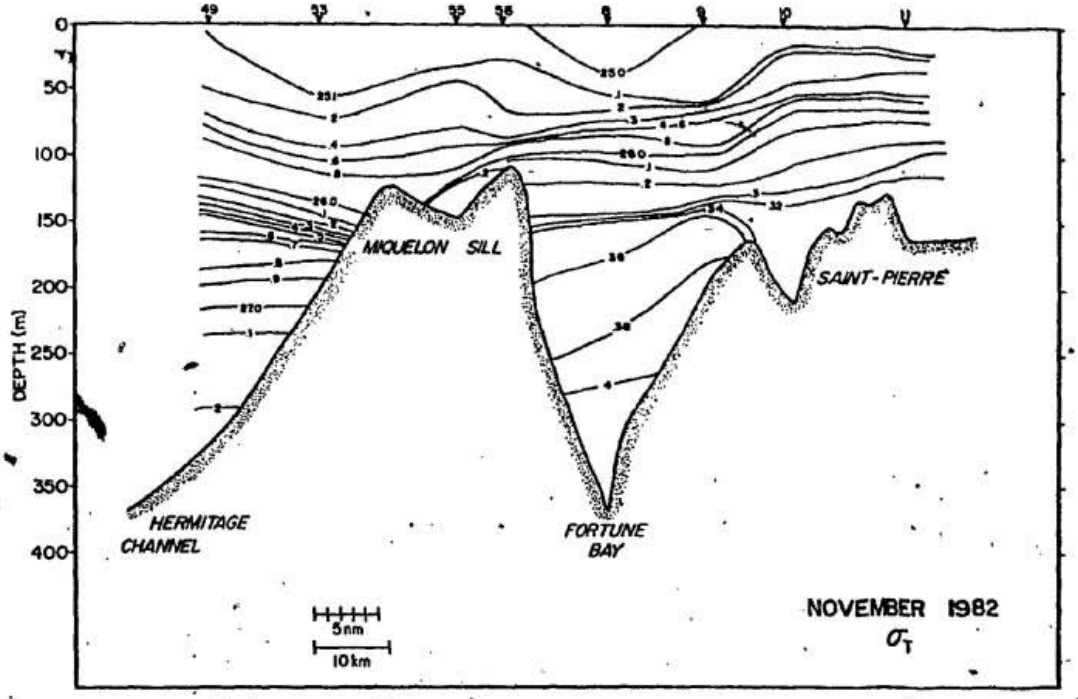


Figure 4.19 Salinity and temperature, plotted along the axis of Fortune Bay, on 12 July 1982.



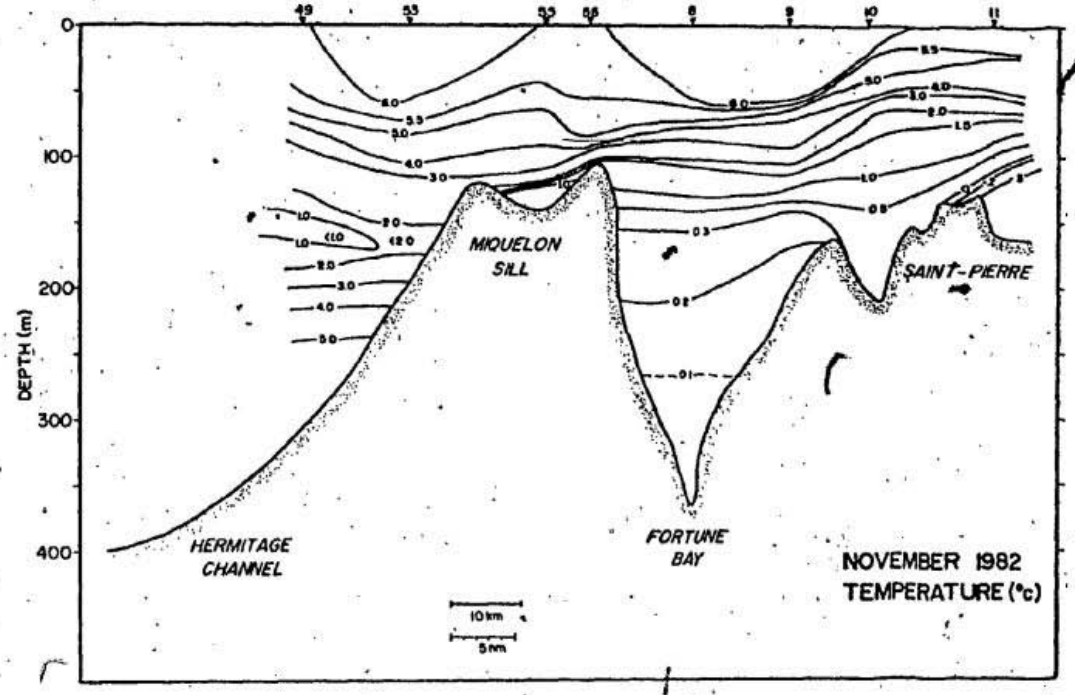


Figure 4.20 Sigma-t and temperature, plotted from Saint-Pierre across Fortune Bay to Hermitage Channel, in November 1982.

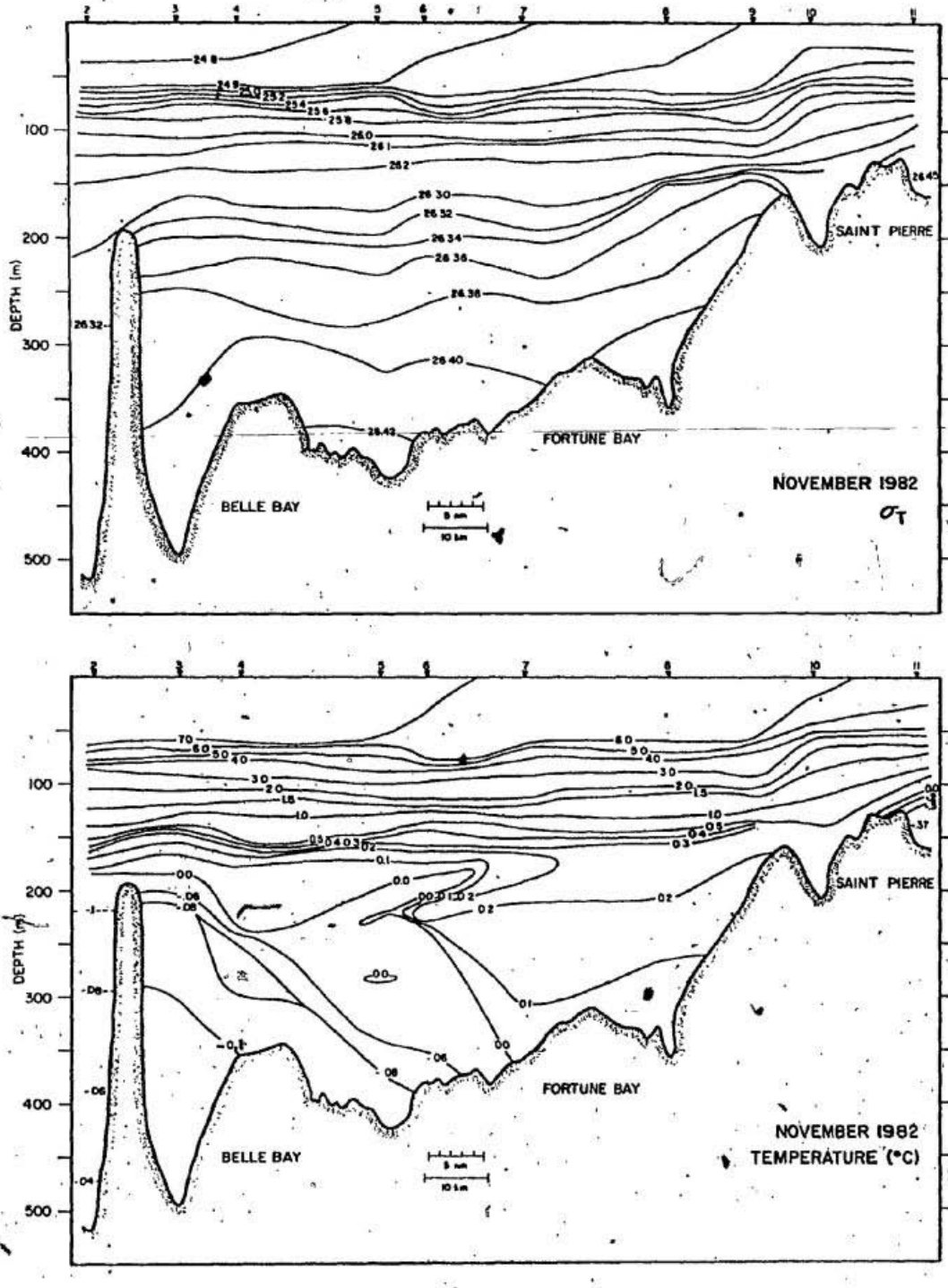


Figure 4.21 Sigma-t and temperature, plotted along the axis of Fortune Bay, in November 1982.

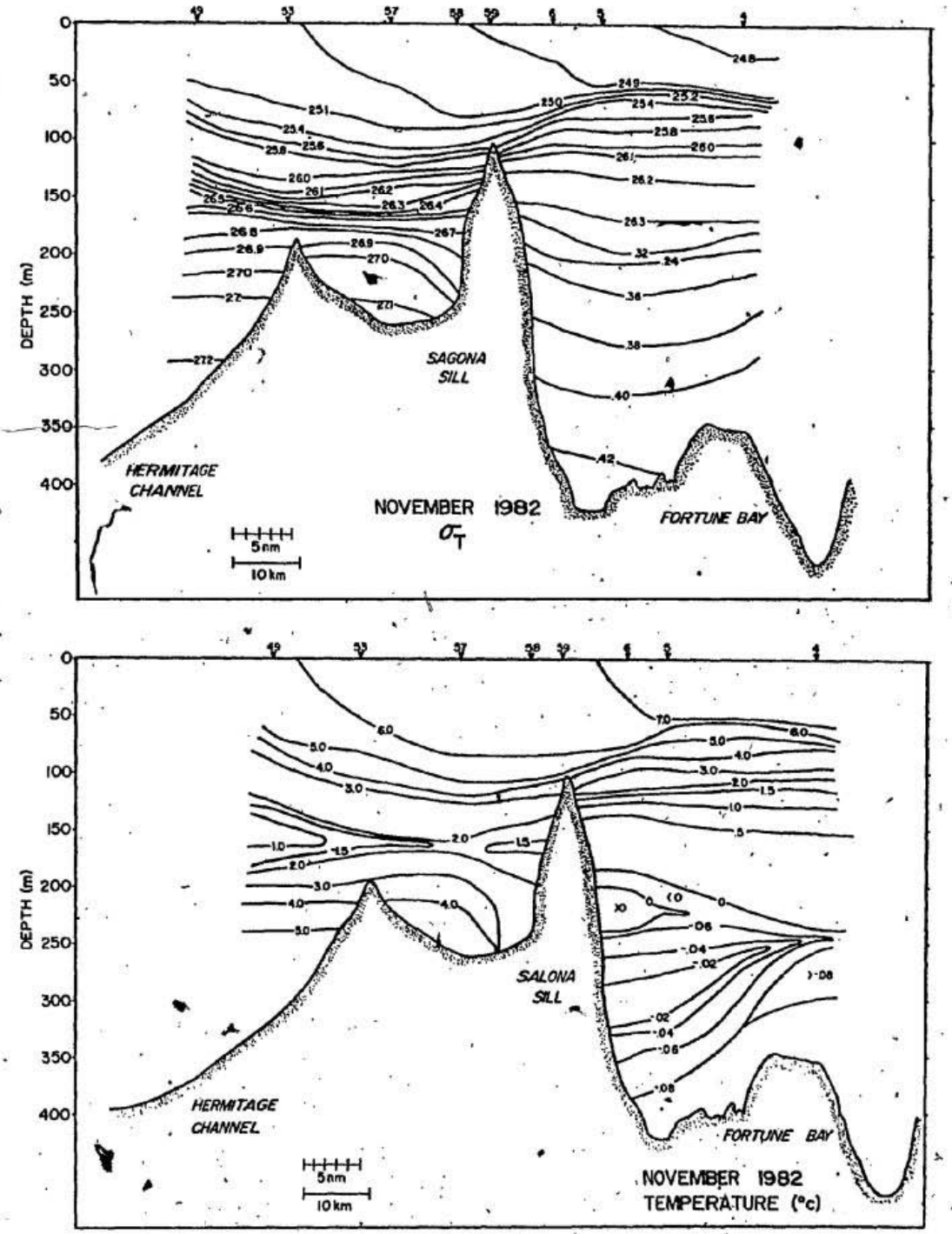


Figure 4.22 Sigma-t and temperature, plotted from Fortune Bay across the Sagona sill to Hermitage Channel, November 1982.

Chapter 5 Density Current Inflow

5.1 Review

Density current flows are an almost ubiquitous physical phenomenon. They occur, in both the atmosphere and the ocean, on a wide range of length and time scales. Powder avalanches, sea breezes, haboobs, mudslides and turbidity currents are all examples. The recent review article by Simpson (1982) shows how varied and intensive the work on density currents has been.

Density current flow occurs as a result of a buoyancy force within a fluid which exists because of density layering. Usually the fluid can be considered as being composed of two layers of fixed, but differing densities. In the ocean this density difference is commonly due to temperature and salinity differences.

The current may be either continuous (Ellison and Turner, 1959; Smith, 1975; Bo Pederson, 1980) or surge type (Middleton, 1966; Benjamin, 1968; Turner, 1973). In surge type flow a characteristic head develops which is thicker than the following flow. The general form of these flows is well described in the review article of Simpson (1982). The nature of such a flow has been recently described by Hay (1983) who studied a turbidity current flow which was artifically created by the discharge of mine tailing into an inlet.

Density current inflow has often been invoked as a mechanism of exchange in studies of deep water renewal in fjords (Gade and Edwards, 1980; Helle, 1978; and Farmer and Freeland, 1983). There have been, as well, some direct studies of these flows in the ocean and in fjords. Both Smith (1975) and Bo Pederson (1980), for example, studied the density

current flow through the Denmark Strait between Iceland and Greenland. In fjords there has been the work of Edwards and Edelsten (1977) and the recent work of Geyer and Cannon (1982). In their study of Puget Sound, Geyer and Cannon present direct observations of density flows but in a region of highly non-uniform bottom slope. Hamblin and Carmack (1978), in an interesting piece of work, describe the effects of mixing and rotation on a positively buoyant density current flow in a large lake in British Columbia.

5.2 Observations

In Chapter 3 the long term data were discussed illustrating the exchange of deep water in Fortune Bay, a discussion carried further in the description of the CTD data presented in Chapter 4. Figures 4.11 and 4.15 show the temperature and density along the axis of the bay in May and June 1982. It is important to note the cold water which extends over the Saint-Pierre sill down into Fortune Bay and beyond station 9. (This feature is also present, but is less pronounced, in Figure 1.4). The survey in June showed that the volume of the subzero water in the bay had increased significantly, as a result of inflow of cold water.

In June 1982 a current meter string was placed two kilometers upslope from station 9, and just to the east of the center of the channel leading into the bay. The mooring was described in Section 2.3 and is shown in Figure 2.3. Three current meters were deployed; at 5, 15 and 65 meters above the bottom.

Stick plots of the current meter data are presented in Figure 5.1 together with the predicted tidal height at Saint-Pierre (Canadian Hydrographic Service, 1982). The north axis of the plots points almost directly into the bay along the line of the channel. For the first day

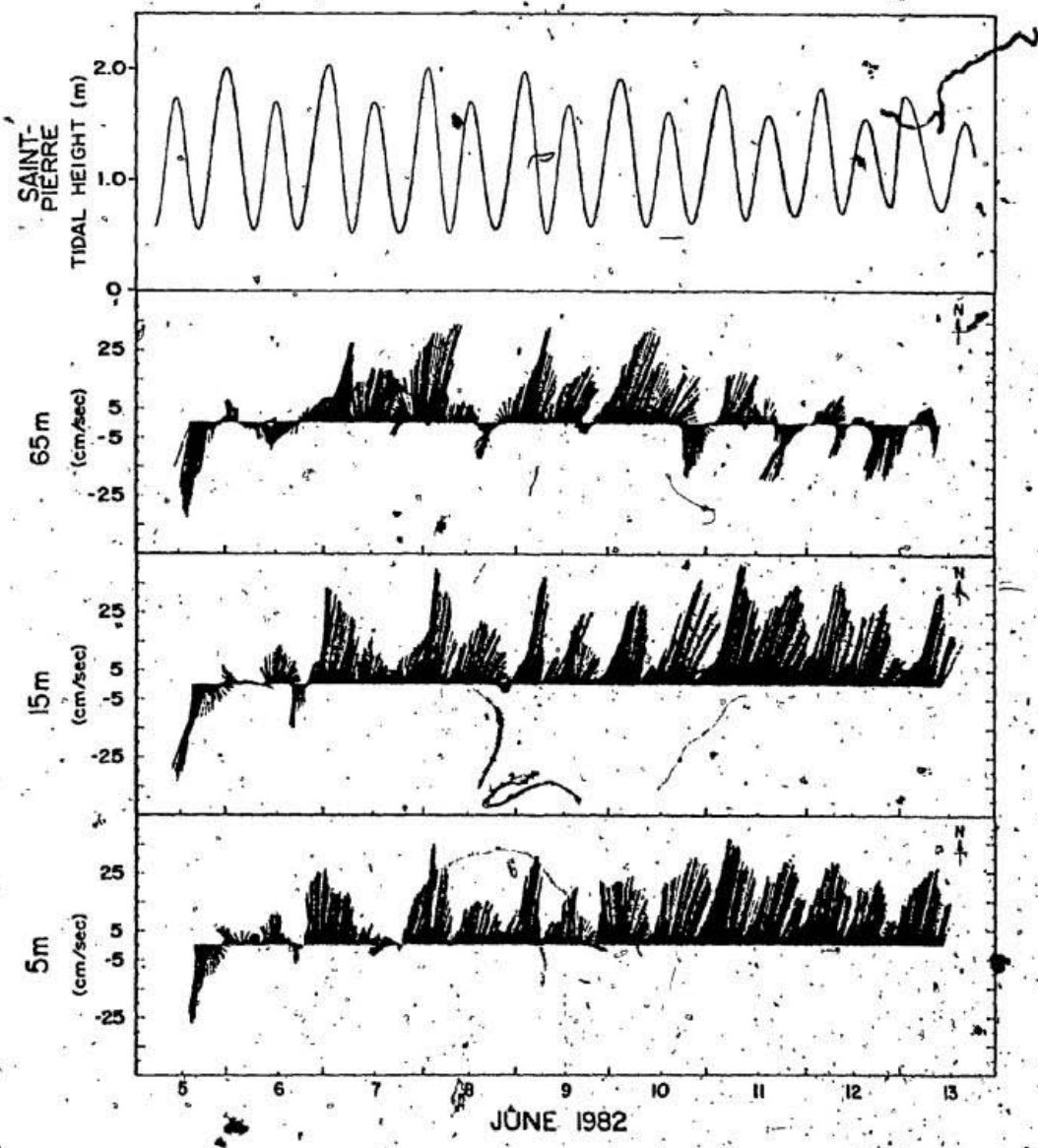


Figure 5.1 Stick plot of current meter data from mooring 3 together with the predicted tidal height at Saint-Pierre. The depth of each current meter above the bottom is indicated at the extreme left. The stick plot is oriented with the north axis straight up.

of the record there is no regular flow into the bay, instead there is oscillating tidal flow. Towards the end of 6 June the flow pattern changes and at 5 and 15 meters the flow is directed almost continuously into the bay. At the upper current meter the flow is more variable since this meter is not always within the density current. A variation in the mean current between the meters at 5 and 15 m can also be observed. The lower meter shows reduced flow speeds which are interpreted to be a result of bottom friction.

Figure 5.2 shows rotated current plots where the U component is directed along 28 degrees true and the V component along 298 degrees true. Positive U is directed into the bay, positive V across channel to the west. The cross-channel speeds are very low (about 5 cm/s) in all three records. The two lower meters show flow into the bay after 8 June while the upper meter at 65 m above the bottom continues to show oscillating tidal flow into and out of the bay.

The most obvious feature of the density current flow is that it is tidally modulated. Visual comparison with the Saint-Pierre predicted tidal plot shows a clear relationship between the two. Maximum flow speeds at the two lower meters occur at, or very near to, flood tide. Minimum flow speeds are observed at, or very near to, ebb tide. Figure 5.3 shows a CTD profile taken at 1612 GMT on 9 June in the center of the channel. The nature of the density current is apparent in the distinct jump in temperature, salinity and density about 20 meters above the bottom. Although not taken at a time when high flow speeds were registered by the near-bottom meters, it can be seen from Figure 5.2 that strong density current inflow did occur on 9 June.

Reduced flow speeds are visually correlated with the period about ebb tide, increased flow speeds with the period about flood tide. For

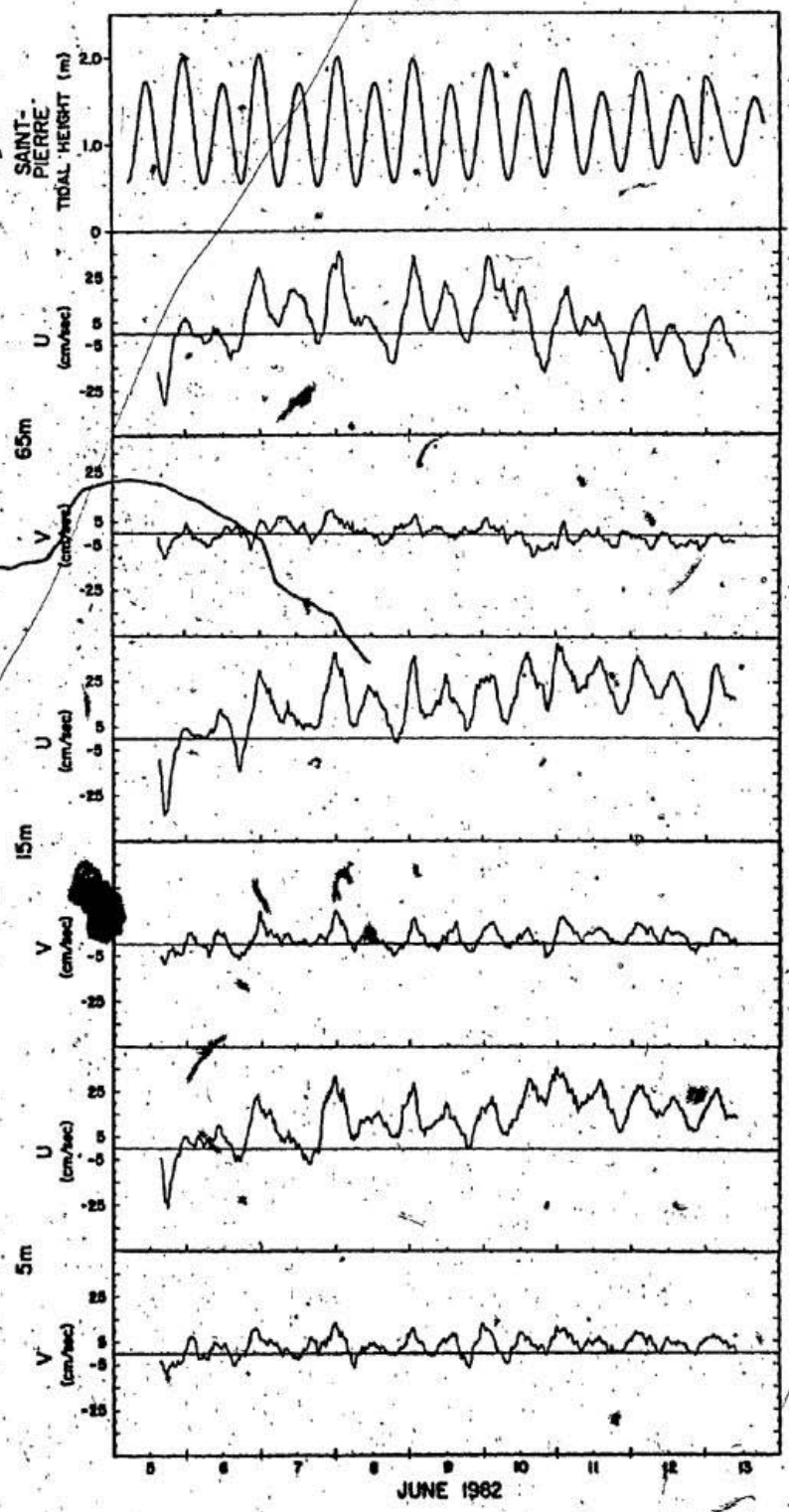


Figure 5.2 Rotated current meter data plotted together with the predicted tidal height at Saint-Pierre. The U component is along 28 degrees true and the V component along 298 degrees true. Thus, positive U is directed into the bay, V across the channel to the west.

SHAMOOK 82-3

LAT	: 47 00.0	STN NAME	: SP65
LONG	: 56 06.5	STN DEPTH	: 201m
DATE	: 9 6 1982	SEQ CAST	: 42

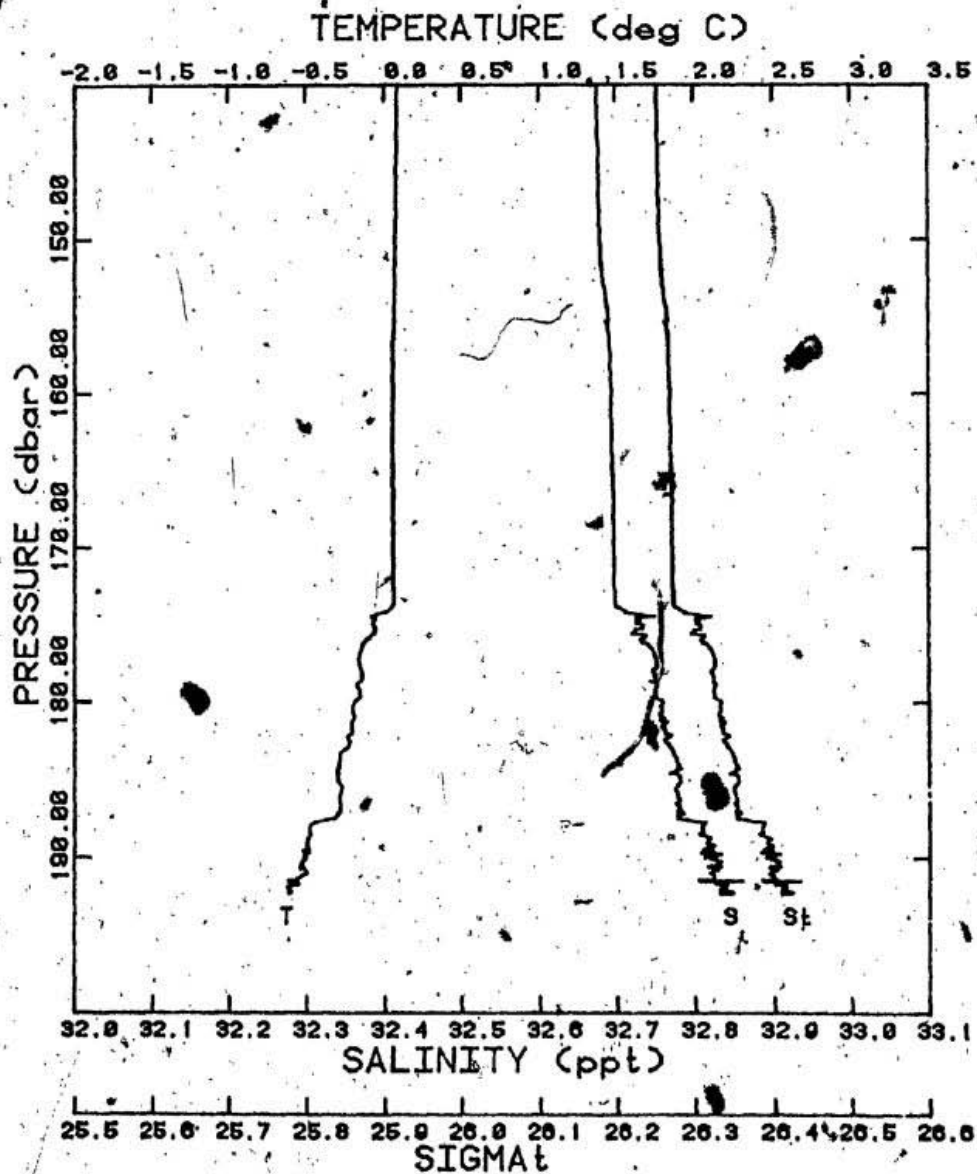


Figure 5.3 The bottom section of a CTD profile taken at station 9, in the middle of the channel, on 9 June 1982 at 1612 GMT (Note 1 dbar = 1 meter).

the early portion of the record, up to about 8 June, when the inflow is weak, peak velocities are nearer to high than flood tide and minimum velocities are nearer to low than ebb tide. Inflow in May and June was found to be at a maximum during periods of spring tides, further illustrating the tie between the inflow and the tides.

When station 11 was occupied on 14 June 1983 conditions were much different from those observed there five days earlier. The bottom temperature had decreased by 0.43°C and the density had increased by 0.14 kg m^{-3}. This indicates the short term variabilty in the deep water outside the Saint-Pierre sill and provides an explanation for the absence of inflow in the early section of the current meter records.

While the current meters were in the water CTD transects were run across the channel along three lines; T2, T3 and T4 (see Figure 1.3). Figures 5.4 and 5.5 present the CTD data from two runs along transect T2 taken on 5 June and 9 June respectively. In the first plot, Figure 5.4, taken on 5 June just after the deployment of the current meters, there appears to be a weak density current inflow. This is inferred from the tilt of the isopycnals upwards towards the right. The current record during this period (see Figure 5.2) shows oscillating tidal flow as discussed earlier. The same transect conducted four days later on 9 June (Figure 5.5) shows strong inflow with an increase in density of 0.1 kg m^{-3} in the bottom layer. The current record during this period shows steady inflow to hug the right hand side of the channel indicating that the flow is in geostrophic balance. Calculations, using the mean geostrophic equation (Pond and Pickard, 1978), based on the slope of the isopycnals near the bottom in Figure 5.5 give a flow speed of about 0.4 m s^{-1}; in reasonable agreement with flow speeds seen in Figures 5.1 and 5.2.

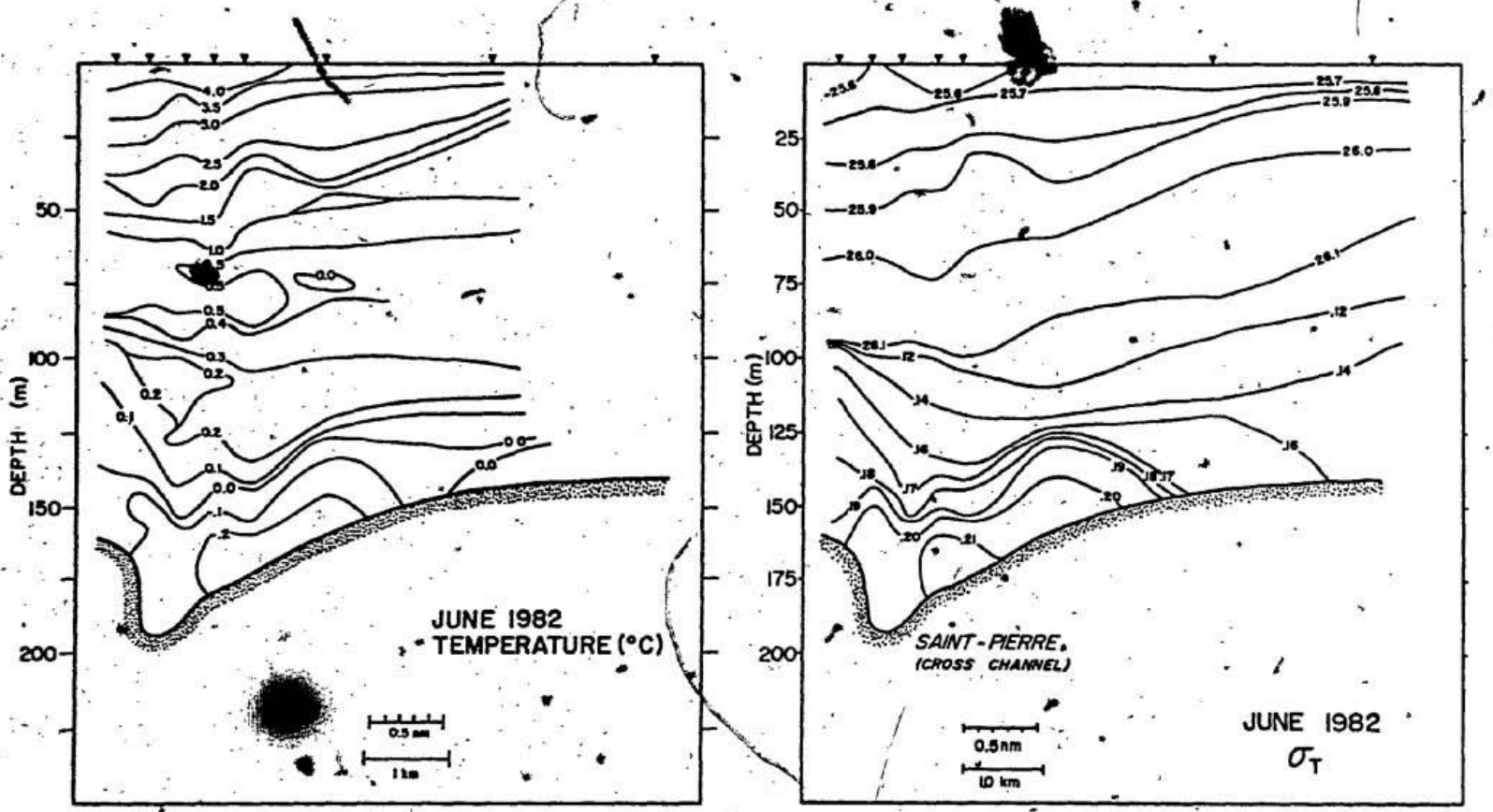


Figure 5.4 Temperature and sigma-t, plotted along transect T2, looking into the bay, on 5 June 1982.

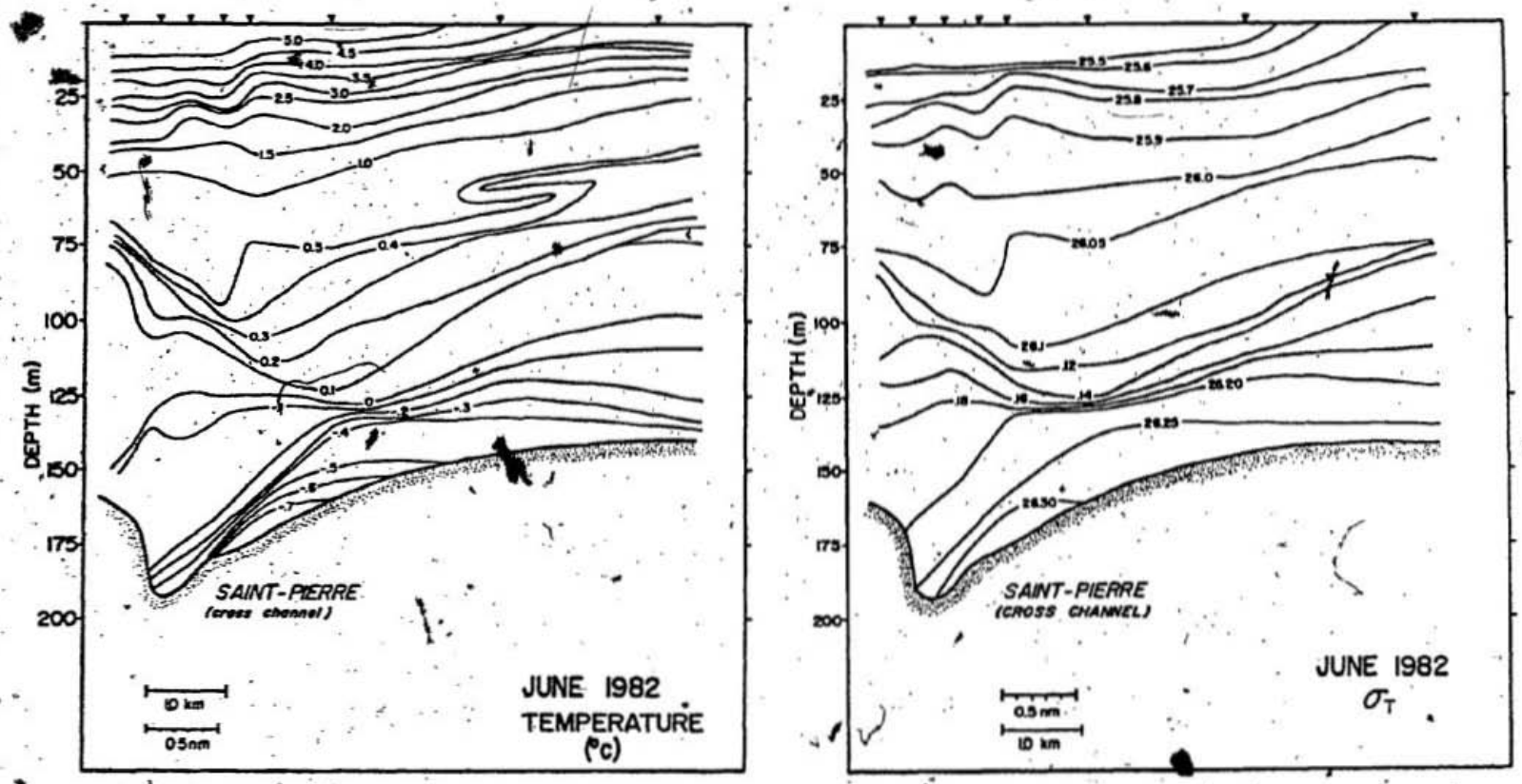


Figure 5.5 Temperature and sigma-t, plotted along transect T2, looking into the bay, on 9 June 1982.

Interpretation of the other cross-channel CTD transects is made difficult by the complex topography of the Saint-Pierre sill region. These other data can be found plotted in Appendix II.

Two explanations are possible for the observed oscillatory flow. In one the tide acts to force the dense water over the sill and so any variations in the flow of this dense current down the slope are related to tidal control of the source water. During ebb tide the dense water will be held back, thus the flow of dense water will be reduced or curtailed. On flood tide the reverse will occur and the flow will increase. The other possible explanation is that the density current is more or less continuous but is arrested by the receding tidal flow both through the action of the stress applied to the upper layer of the density current and the adverse pressure gradient imposed by the slope of the free surface. On flood tide the flow would be accelerated by the inflowing tidal current. More shall be said in the next few sections about the nature of these two mechanisms.

5.3 Theory

In this section an attempt shall be made to model a continuous density current flow along a slope. Previous treatments (Ellison and Turner, 1959; Smith, 1975; Bo Pederson, 1980) have discussed flow into an ambient fluid which was considered to be at rest. In Fortune Bay, where the inflow occurs through a narrow strait with reasonably large tidal currents, this approximation may not hold. To begin, the case where there is flow in the upper layer will be considered. The effects of entrainment upon the density current flow will be ignored. Entrainment will be discussed separately in the following section.

The model attempts to analytically describe the flow along the slope leading from the Saint-Pierre sill down into Fortune Bay. From the 160 m

point in the center of the channel to the 322 m point in the bay at station 8 is approximately 20 km. The mean slope along this path is 0.6° although there are variations in grade between the two points.

Figure 5.6 shows a schematic of the system which is to be discussed. The densities in the lower and upper layers are ρ' and ρ respectively. h is the thickness of the density current and d is the reference depth for the analysis. ξ is the surface elevation due to the tide and $d + \eta$ is the total depth when $\xi = 0$. The bottom slope is $\tan\beta$. The coordinate system is rotated such that positive x is directed into the bay along the center if the channel, and that positive z is normal to the bottom.

No cross-channel flow will be considered, an assumption supported by the measurements plotted in Figure 5.2. The cross-channel flow can be seen to be much less than that along the channel. All terms in v and v' will therefore be zero. Only the nonlinear terms $u\frac{\partial u}{\partial x}$ and $u'\frac{\partial u'}{\partial x}$ will be kept.

The equations of motion and the continuity equation in the upper layer can then be written, for the case of steady flow:

$$(5.1)\quad u\frac{\partial u}{\partial x} = \frac{-1}{\rho}\frac{\partial p}{\partial x} + g\sin\beta + \frac{1}{\rho}\frac{\partial \tau^{xz}}{\partial z}$$

$$(5.2)\quad fu = \frac{-1}{\rho}\frac{\partial p}{\partial y}$$

$$(5.3)\quad \frac{\partial u}{\partial x} + \frac{\partial w}{\partial z} = 0$$

In the lower layer the equations are:

$$(5.4)\quad u'\frac{\partial u'}{\partial x} = \frac{-1}{\rho'}\frac{\partial p'}{\partial x} + g\sin\beta + \frac{1}{\rho'}\frac{\partial \tau'^{xz}}{\partial z}$$

$$(5.5)\quad fu' = \frac{-1}{\rho'}\frac{\partial p'}{\partial y}$$

$$(5.6)\quad \frac{\partial u'}{\partial x} + \frac{\partial w'}{\partial z} = 0$$

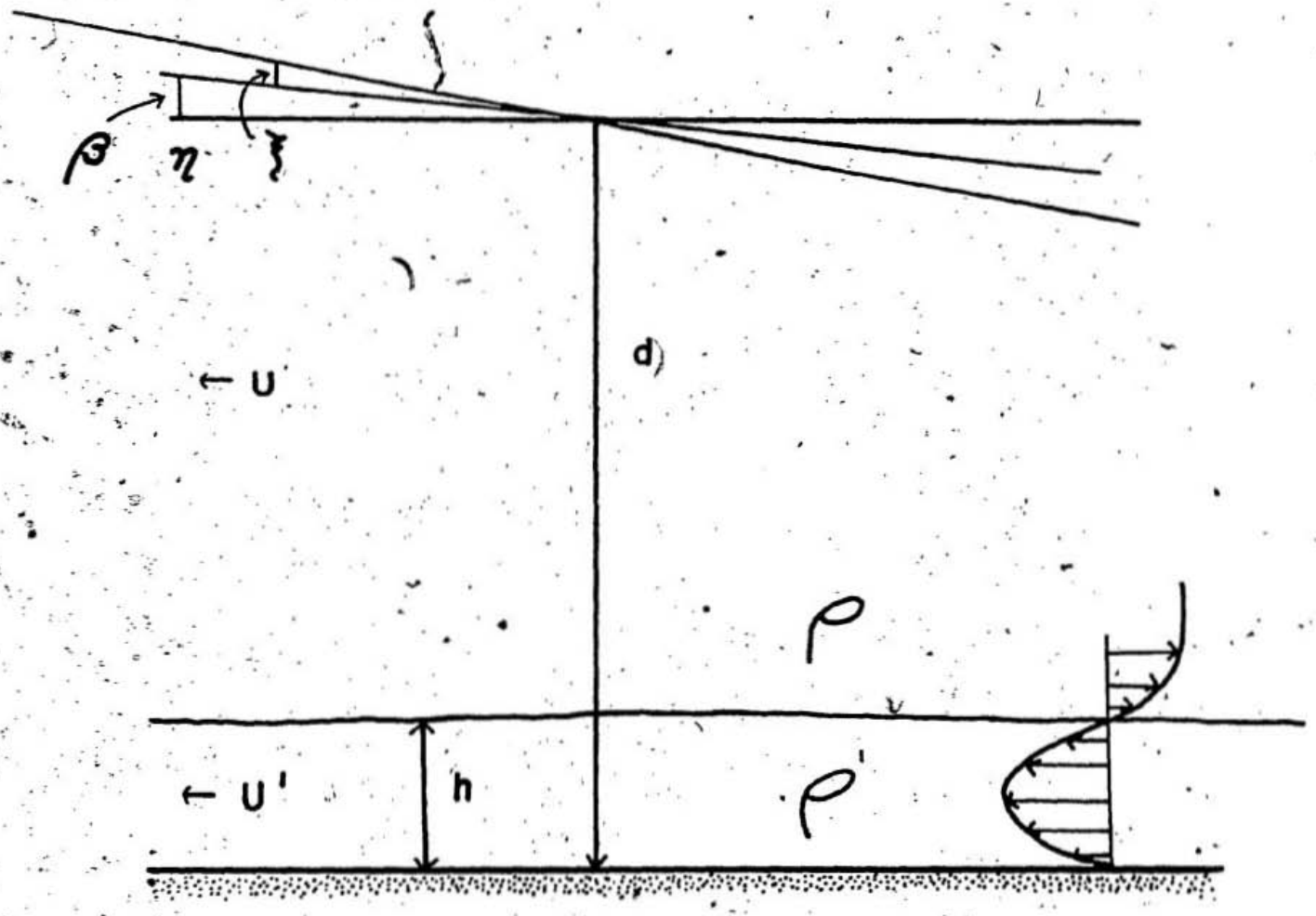


Figure 5.6 Schematic of the density current inflow in a rotated coordinate system. The z axis, located at the surface, has positive z directed upwards. The schematic current profile on the right indicates the approximate form of the current in the lower layer.

The non-linear term $w'\frac{\partial u'}{\partial z}$ has been dropped because, after vertical integration, this term becomes part of the interfacial stress. The argument for ignoring the time-dependent terms can be made by considering the tidal velocity to be of the form $U(x,t) = U(x) \sin 2\pi t/T$ where T is the tidal period. It can be seen from this that $\frac{\partial u}{\partial t}$ will be 90° out of phase with u and so when u is large, which is the case we are considering here, then $\frac{\partial u}{\partial t}$ will be small.

The pressure in the upper and lower layers can be written:

(5.7) $p = -\rho g \cos\beta\ (z-\eta-\xi)$

(5.8) $p' = -\rho g \cos\beta\ (z-\eta-\xi) - \Delta\rho g \cos\beta\ (d-h+z)$

where $\Delta\rho = \rho'-\rho$. Noting that $\frac{\partial \eta}{\partial x} = \tan\beta$, the resultant momentum equations can now be written.

(5.9) $0 = -\rho g \cos\beta \frac{\partial \xi}{\partial x} + \frac{\partial \tau^{xz}}{\partial z} - \rho u \frac{\partial u}{\partial x}$

(5.10) $0 = -\rho g \cos\beta \frac{\partial \xi}{\partial x} + \Delta\rho(\sin\beta - \cos\beta \frac{\partial h}{\partial x}) - \rho' u' \frac{\partial u'}{\partial x} + \frac{\partial \tau'^{xz}}{\partial z}$

These can be integrated to give:

(5.11) $-\tau_i = \int_{-d+h}^{\eta+\xi} \left[\rho g \cos\beta \frac{\partial \xi}{\partial x} + \rho u \frac{\partial u}{\partial x}\right] dz$

(5.12) $\tau_i' - \tau_b' = \int_{-d}^{-d+h} \left[\rho g \cos\beta \frac{\partial \xi}{\partial x} - \Delta\rho g(\sin\beta - \cos\beta \frac{\partial h}{\partial x}) + \rho' u' \frac{\partial u'}{\partial x}\right] dz$

where τ_i' and τ_b' are the interfacial and bottom stresses. The terms $\cos\beta \frac{\partial \xi}{\partial x}$ and $\sin\beta - \cos\beta \frac{\partial h}{\partial x}$ are independent of z. The densities in the upper and lower layers can also be considered z-independent. The last terms in each of the equations, the nonlinear ones, are the least straightforward to evaluate since it is not apparent that they should be independent of z. These are potentially important terms which must be dealt with.

The vertically integrated continuity equation in the upper layer is:

$$(5.13)\quad \frac{\partial \bar{u}}{\partial x} = \frac{\bar{u}}{(d-h+\eta)}\left[\frac{\partial h}{\partial x} - \frac{\partial \eta}{\partial x}\right]$$

Equation (5.13) is derived assuming that the following statement is true:

$$(5.14)\quad \frac{\partial \xi}{\partial x} << \frac{\partial h}{\partial x} << \frac{\partial \eta}{\partial x}$$

A scaling argument can be made to justify this assumption. For Fortune Bay the maximum tidal range can be taken as 2 m so the term on the left will be, at most, of order 2m/20 km = 10^{-4}. This is clearly an overestimate since the length scale for the tidal slope will be much greater than 20-km. Using the same value for x and taking h over this range as 20 m and η as 157 m the terms on the right hand side of 5.14 will be 10^{-3} and 8×10^{-3} respectively. From this it can be seen that (5.14) is a valid assumption.

In the lower layer the vertically integrated continuity equation is:

$$(5.15)\quad \frac{\partial \bar{u}'}{\partial x} = -\frac{\bar{u}'}{h}\frac{\partial h}{\partial x}$$

In these equations $\bar{u}$ and $\bar{u}'$ are vertically averaged velocities in the upper and lower layers. It will be assumed that u is independent of z. This is reasonable based upon two arguments which are best made clear by reference to one of the CTD transects, for example Figure 5.4. The upper layer is considered to be a homogeneous mixture on which the effects of the pycnocline on the density current are ignored. The thickness of this upper layer is much greater than the frictional boundary layer thickness. Frictional effects upon u will therefore be small over most of the water column. The second argument is that the kinematic constraint at the surface implies that u at the surface will be reduced by $1 - \cos\beta$, that is by less than 10^{-4}. Therefore $\frac{\partial u}{\partial z}$ will be considered to be negligibly small.

In contrast, $\frac{\partial u'}{\partial z}$ is not expected to be zero since the velocity profile in the lower layer should be of the form shown schematically in Figure 5.6

(Ellison and Turner, 1959). The thickness of the frictional boundary layer may not be much less than the flow thickness h so u' can not be considered independent of z.

Equation (5.11) can now be written:

$$(5.16) \quad \tau_i = -\rho g\,(d-h+\eta)\,\frac{\partial \xi}{\partial x}\cos\beta + \rho \bar{u}^2\,\frac{\partial \eta}{\partial x}$$

where following equation (5.14) $\frac{\partial h}{\partial x}$ is ignored with respect to $\frac{\partial \eta}{\partial x}$.

The integral of the nonlinear term in equation (5.12) can be treated by recalling the continuity equation (5.6). Since w' must be zero at the interface (in the absence of entrainment and under steady-state conditions) and at the bottom, then its partial derivative with respect to z will be approximately zero. So, therefore, will the partial derivative of u' with respect to x and thus the nonlinear terms in the lower layer can be dropped. It is reasonable to drop the term in the lower layer and not in the upper layer since they are proportional to $\frac{\partial h}{\partial x}$ and $\frac{\partial \eta}{\partial x}$ respectively.

Once again following equation (5.14) the integrated equations (5.11) and (5.12) become:

$$(5.17) \quad \tau_i = -\rho g(d-h+\eta)\frac{\partial \xi}{\partial x}\cos\beta + \rho\,\bar{u}^2\frac{\partial \eta}{\partial x}$$

$$(5.18) \quad (\tau_i' - \tau_b') = \rho g h\,\frac{\partial \xi}{\partial x}\cos\beta - \Delta\rho g h \sin\beta$$

The stress equations can be written as in Bo Pederson (1980, p. 36):

$$(5.19) \quad |\tau_i'| = \frac{\rho' f_i}{2}\,(\bar{u}' - \bar{u})^2$$

$$(5.20) \quad |\tau_b'| = \frac{\rho' f_b}{2}\,\bar{u}'^2$$

Here f_i is the friction coefficient at the interface and f_b the coefficient at the bottom. At the interface the stress must be continuous so $\tau_i = \tau_i'$. The schematic velocity profile in Figure 5.6 (Ellison and Turner, 1959) makes clear that $\tau_b' > 0$ since the lower layer velocity is

directed towards the left and $\tau_i < 0$ at the interface.

The tidal term will be eliminated by substitution from equation(5.18) into (5.17). The result of this substitution is:

$$(5.21)\quad \left[1 + \frac{h}{(d-h+\eta)}\right]\frac{f_i}{2}(\bar{u} - \bar{u}')^2 + \frac{f_b}{2}\bar{u}'^2 + \left[\frac{h}{(d-h+\eta)}\right]\bar{u}^2\frac{\partial\eta}{\partial x} = g'h\sin\beta$$

Equation (5.12) reduces to the following when there is no flow in the upper layer, i.e. $u = 0$:

$$(5.22)\quad \bar{u}' = \left[\frac{g'h\sin\beta}{\left(\frac{f_i + f_b}{2}\right)}\right]^{1/2}$$

It is also assumed here that $d >> h$. This is a Chezy-type equation in agreement with results of Bo Pederson (1980).

For the case when the upper layer has arrested flow in the lower layer, i.e. $u' = 0$, then:

$$(5.23)\quad \bar{u}^2 = \frac{g'h\sin\beta}{\left[1 + \frac{h}{d-h+\eta}\right]\frac{f_i}{2} + \left[\frac{h}{d-h+\eta}\right]\frac{\partial\eta}{\partial x}}$$

5.4 Entrainment

Entrainment has been ignored in the previous section but is in fact a very important aspect of the flow. The dense water that flows over the sill does not arrive at the bottom of the bay unmodified. Entrainment can be viewed as a one-way mixing process whereby ambient fluid is entrained into the density current.

Bo Pederson (1980,pp.13-30) provides an extensive discussion of the problem. A relationship exists between the bulk Richardson number,

$$(5.24)\quad Ri = \frac{g'h}{\bar{u}'^2},$$

and the entrainment velocity.

This is important because the bulk Richardson number of the flow is expected to be a constant. Using the results of the previous section when $\bar{u} = 0$, (5.24) becomes:

$$(5.25) \qquad Ri = \frac{f_i + f_b}{2\sin\beta}$$

This shows that for fixed slope conditions Ri should be a constant and so therefore should the entrainment velocity.

For subcritical flow the ratio of the entrainment velocity to the flow velocity is given by Bo Pederson (1980,p.76) as:

$$(5.26) \qquad \frac{w_e}{\overline{u'}} = 0.072\sin\beta$$

This result will permit the computation of the total entrainment into the density current as it flows down the slope.

5.5 Comparison of Theory and Observation

It is possible to use the results of the previous sections to compute the expected velocities and entrainment in order to test the validity of the theory and also the analysis of the effect of flow in the upper layer on the density current overflow.

From the CTD data (e.g. Figure 5.5); h = 20 m, $\Delta\rho = 0.2$ kg m^{-3} and using $\sin\beta = 1.05 \times 10^{-2}$ allows the calculation of the expected flow speeds with the use of equation (5.24) found that for subcritical flows the sum of the bottom and interfacial friction factors should be:

$$(5.27) \qquad 2 \times 10^{-3} < \frac{f_b + f_i}{2} < 3 \times 10^{-2}$$

which gives, upon substitution, the following range of values for $\overline{u'}$:

$$0.11\text{m s}^{-1} < \overline{u'} < 0.45\text{m s}^{-1}$$

a result in very good agreement with the current records presented in Figures 5.1 and 5.2 where the speed ranges from 0 to 0.45 m s^{-1}.

It is now possible to assess the effect of flow in the upper layer on the density current flow. To do this it is best to modify equation 5.23 by dividing above and below by the friction coefficient, which for simplicity shall be written $f_* = f_i + f_b$. If this is done, equation (5.23) becomes:

$$\bar{u}' = \overline{U'}_o \left[\frac{\frac{f_*}{2}}{\left(1 + \frac{h}{d - h + \eta}\right)\frac{f_i}{2} + \left(\frac{h}{d - h + \eta}\right)\frac{\partial \eta}{\partial x}} \right]^{1/2} \tag{5.28}$$

where $\overline{U'}_o$ represents the velocity of the density current in the absence of flow in the upper layer. Thus evaluating the term on the right will determine what the ratio of the upper layer flow must be to arrest a density current with flow speed $\overline{U'}_o$. Substituting the same values for the friction factor as used in the earlier calculation gives: $1.0|\overline{U'}_o| < |\bar{u}| < 4.0\,|\overline{U'}_o|$ which says that the upper layer velocity must be at least as great as the density current velocity to arrest the flow.

This is only an approximate result since the interfacial and bottom friction factors are not well known. It does show, however, that it is at least theoretically possible for the upper layer flow to arrest the density current. The current record in Figure 5.2 shows, for the period from 9 June onwards, reduced flow speeds at the bottom two meters lag the upper meter by one to two hours. This is consistent with the upper layer flow exerting a direct controlling influence upon the density current.

The entrainment problem can be considered by applying equation (5.26) to compute the entrainment velocity. The result of this calculation is $w_e = 1.3 \times 10^{-4}$ m s^{-1} using an inflow speed of 0.2 m s^{-1} determined from a visual average of the current at 5 meters above bottom in Figure 5.2 for the latter section of the record. If the layer thickness is

assumed to be 20 meters and the channel length 16 kilometers then about 30% of the resultant water will have been entrained.

A direct observation of the mixing of the inflow waters can be made using a T-S diagram. Figure 5.7 shows the temperature and salinity of the resultant waters at the two sills together with bay water at the time of exchange. For the Saint-Pierre inflow, the temperatures and salinities of the resultant water are based upon Figure 4.15 using the coldest water at the bottom of the bay (-.42°C) for the resultant water. The bay water is chosen from the depth range 150 to 250 meters at station 8; the sill water is chosen from the bottom of station 11. For the Miquelon inflow, the sill water is chosen from the bottom of station 55 and the bay water from mid-depth at station 8 in Figure 4.9. The resultant bottom water used was that at the bottom of station 8.

The plot shows that the Saint-Pierre inflow resultant water contains about 55% bay water. The resultant water from the Miquelon sill inflow water contains nearly 66% bay water. These values can be considered as upper limits to the entrainment since mixing is expected to occur via other mechanisms than entrainment.

The high proportion of bay water observed to mix with the Miquelon sill inflow is not unexpected since the slope inside the Miquelon sill is three times steeper than that for the Saint-Pierre sill. Equation 5.26 clearly shows that more entrainment will occur on steeper slopes.

5.6 Labrador Current Transport

The mean flow speed of the current can also be used to compute the transport of Labrador Current Water into Fortune Bay. Assuming an inflow speed of 0.2 m s^{-1}, a thickness of 20 meters and a channel width of 3 kilometers gives a transport of 1.4×10^4 m^3 s^{-1}. This is set to more

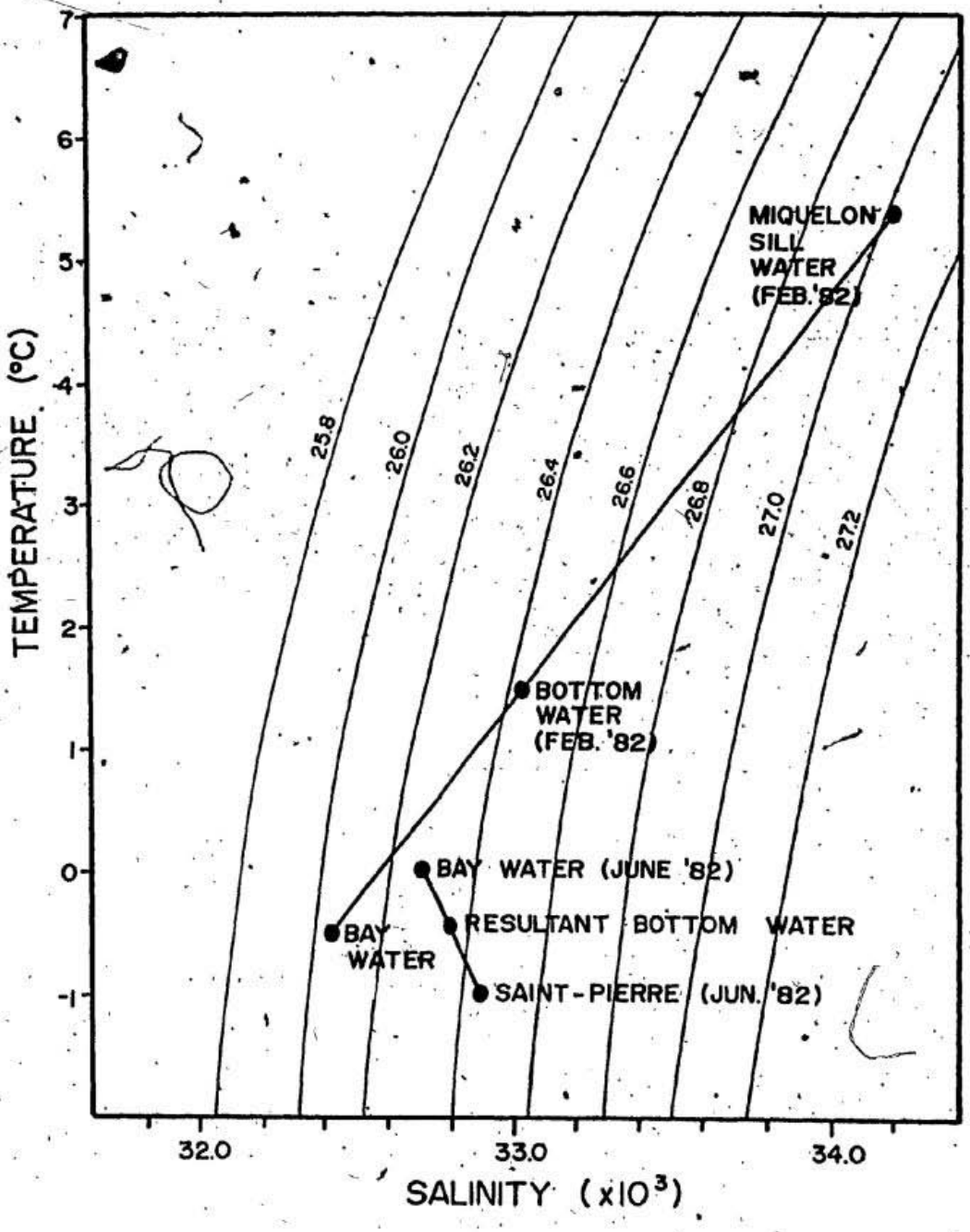


Figure 5.7 A T-S plot of inflow, bay and resultant waters showing the effect of mixing on the water which enters the bay.

or less include all of the water up to the -.3°C isotherm with the limiting horizontal width based upon Figure 5.6. The volume of Fortune Bay below 150 meters is 3.4×10^{11} m^3 which means that it would take over 300 days to exchange all of the water below 150 meters. This provides a possible explanation for the absence of water less than -0.5°C at stations 4 and 8 in Figure 3.1.

Chapter 6 Miquelon Sill Flow

6.1 Moorings

Two moorings, M1 and M2 (Figures 2.1 and 2.2), each with two current meters and a 30 meter long thermistor chain were deployed on either side of the Miquelon sill of Fortune Bay for the period 6-13 May 1982. Their positions are indicated in Figure 1.3. They were deployed and recovered from the CSS DAWSON. For convenience the position of an instrument will be given as the height above the bottom. Thus each mooring has a current meter at 6 and 65 meters and a thermister chain running from 11 to 41 meters above the bottom.

6.2 Thermistor Chain and Current Meter Data

Figures 6.1A and 6.1B show the temperature contours plotted versus time from the thermistor chain and current meter temperature data. The temperature data from the current meter immediately below the thermistor chain were used in each of these plots. The data have been filtered using three successive moving average filters of the type described by Godin (1972) to remove the high frequency components. The filter used was A12A12A14, three successive running average filters which serve to remove any signal having a period shorter than one hour. The thermistor chain data were sampled at 5 minute intervals; after filtering the data were decimated to 30 minute intervals for the purpose of plotting. Also plotted in Figure 6.1 is the predicted tidal height (Canadian Hydrographic Service, 1982) at Grand Bank, which is about 32 km east of the Miquelon sill.

The current data are presented as stick diagrams on Figure 6.2 together with the predicted tide at Grand Bank. Winds for the mooring period at Saint-Pierre, taken from surface weather charts, are plotted in

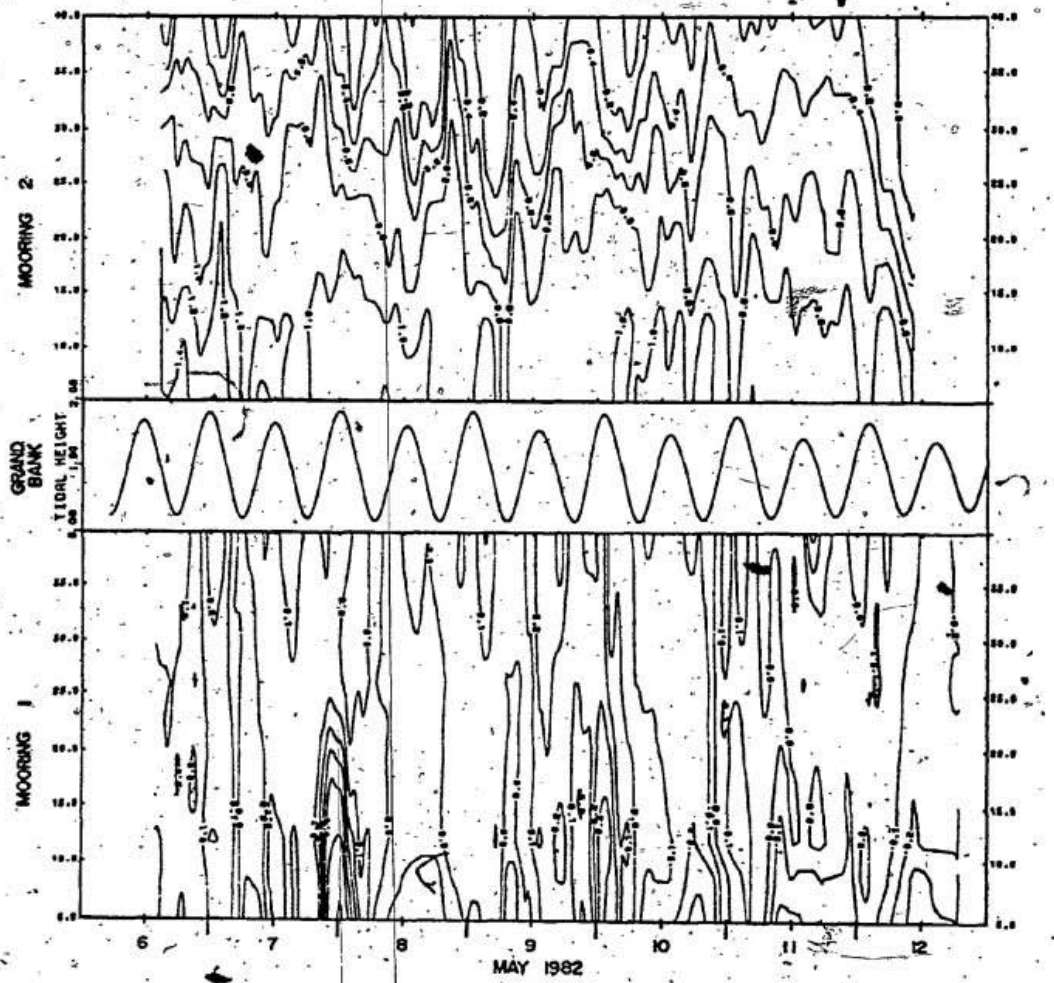


Figure 6.1 Temperature contours from the thermistor chains on moorings M1 and M2. Figures to the left and right give the height above the bottom. Predicted tidal height at Grand Bank, located on the eastern shore of Fortune Bay, is plotted in the center.

Figure 6.3. The open circles on the chart indicate no data were available.

The differences between the two thermistor chain records in Figure 6.1 are striking. The outside chain (6.1B) shows more stratification and warmer temperatures than the inside chain (6.1A). This is consistent with the CTD data discussed in Chapter 4 (Figure 4.10).

In Figure 6.1A there are four periods when warm water intrusions at the bottom are observed; at the end of 7 May; the start of 10 May; the end of 10 May and early on 12 May. The last two events are much less pronounced and will not be discussed in great detail. The first two intrusions occur between maximum flood and high tide, the last two near low tide. Currents at the bottom meter are directed between east and northeast for the two periods when the warm water intrusions are observed. The flow is thus directed into the bay. For the period around 10 May and onwards moderate northeasterly winds are observed (Figure 6.2).

For the warm water uplift on 7 and 8 May the 0.4°C isotherm is observed to rise to 15 meters and the maximum observed temperature at 6 meters is 0.66°C. This water will have a density of 26.5, easily dense enough to sink to the bottom of the bay. The rise in temperature is extremely sudden and occurs just after flood tide, indicating that the warm water between stations 56 and 54 has been forced up over the sill on the flooding tide. Once over the sill this slug of dense water should sink as a density current down the Miquelon slope and into Fortune Bay. This is consistent with the observed current speeds at the time (Figure 6.2).

It is interesting that no warm water was observed at station 8 which was sampled on 10 May some two days after this event. Station 8 is located over a bathymetric depression about 35 meters deep and less than a kilometer across. It should be possible to detect any dense water

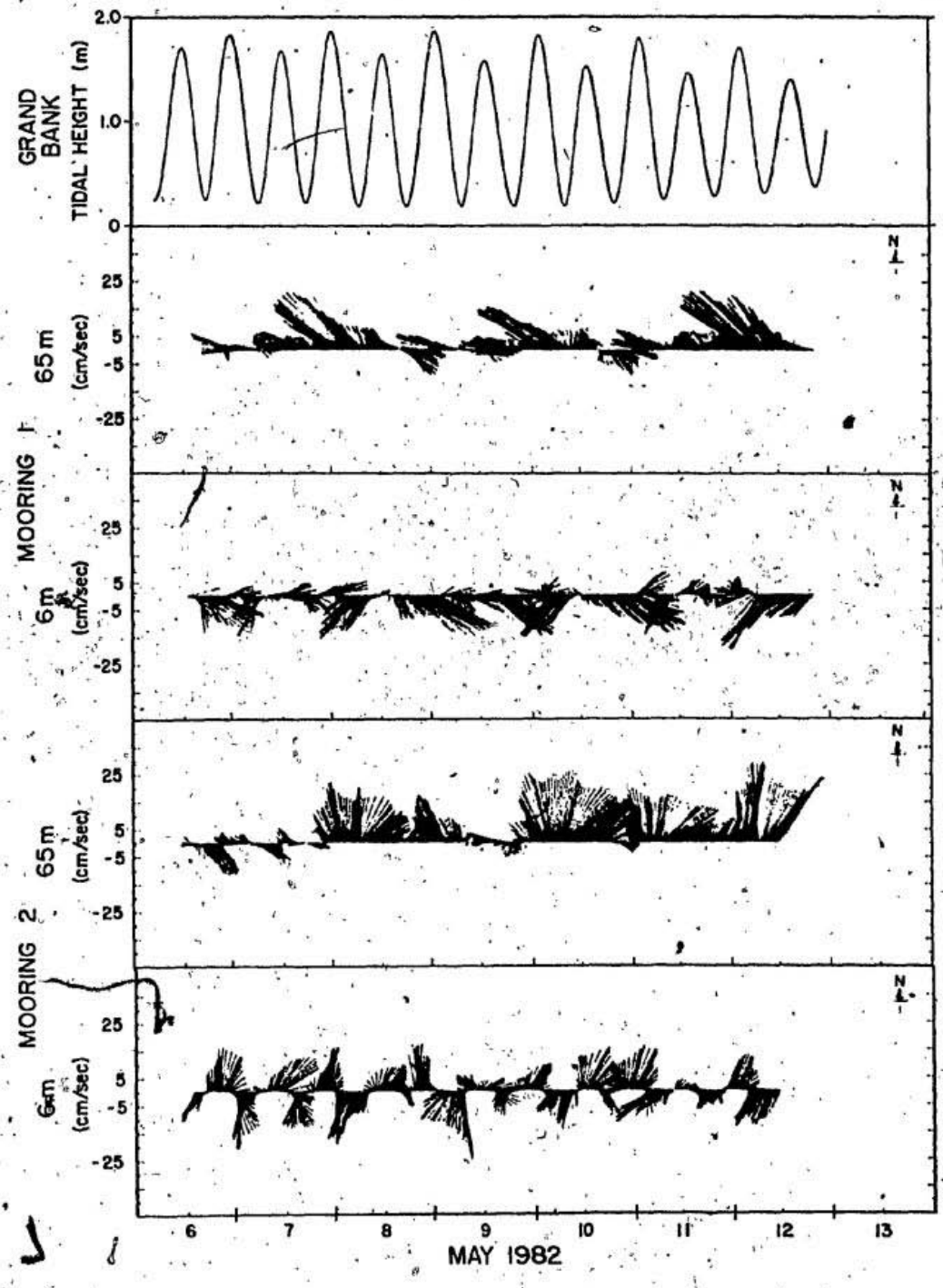


Figure 6.2 Stick plot of the current meter data from moorings M1 and M2. Figures in bold indicate the height of the meter above the bottom. The predicted tidal height at Grand Bank, located on the eastern shore of Fortune Bay, is plotted at the top.

which flows into the bay and is caught in this hole unless, of course, it bypasses this hole or is flushed away. The current speed at the time was observed to be 0.2 m s^{-1}, meaning the slug of warm water should have reached station 8 after about one day. That the warm water was not observed is probably due to the intensity of the cold water inflow over the Saint - Pierre sill. The strength of this inflow and its density, 26.4, were such that it could overwhelm this comparatively small slug of warm water from the Miquelon sill.

Current Meter Data

Current meter data at the inside mooring (Figure 6.2) presents clear evidence of a net southeastward flow into the bay. At 65 m the inside mooring shows consistent northwestward flow directed out of the bay. Mooring 2 shows oscillatory flow at the bottom and, consistent with mooring 1, northward flow at 65 m. Table 6.1 presents the results of a progressive vector analysis of the current meter data.

TABLE 6.1 PROGRESSIVE VECTOR PLOT DATA

Mooring	Isobath Alignment°	Excursion (km)	Dir°	Speed (m s^{-1})
Inside 6m	270/90	28.5	132	0.066
Inside 65m	270/90	23.0	315	0.053
Outside 6m	220/40	7.7	177	0.018
Outside 65m	220/40	30.9	19	0.072

The mean flow speeds are quite low, less than 0.1 m s^{-1}. The difference in mean flow direction seems quite significant, almost 180° from 65 meters to 6 meters. This reversal is apparent from inspection of the stick diagrams.. The flow is at approximately 40° to the right of the isobaths at the inside station and 20 to 40° to the left of the isobaths at the outside station. This result may simply be an indication of

the quality of the hydrographic chart in this specific area and the difficulty in determining the directions from it.

Figure 6.3 shows the wind for this period at Saint-Pierre taken from surface pressure charts prepared at Nordco Ltd. A complex low pressure system passed over the area during the period when the moorings were in place. A shift in the direction and speed occurred on 10 May and could have caused strong (> 0.25 m s^{-1}) northerly currents at the upper current meter at M2 which began at this time. There did not appear to be as significant a change at the inside mooring and none at all the bottom meters.

The record from the bottom meter at the inside site shows more or less regular flow into the bay with direction oscillating from 110 to 220°. For the most part this water is cold, often less than 0.1°C. During these periods, if it is denser than the water inside the bay it will be by only a small amount.

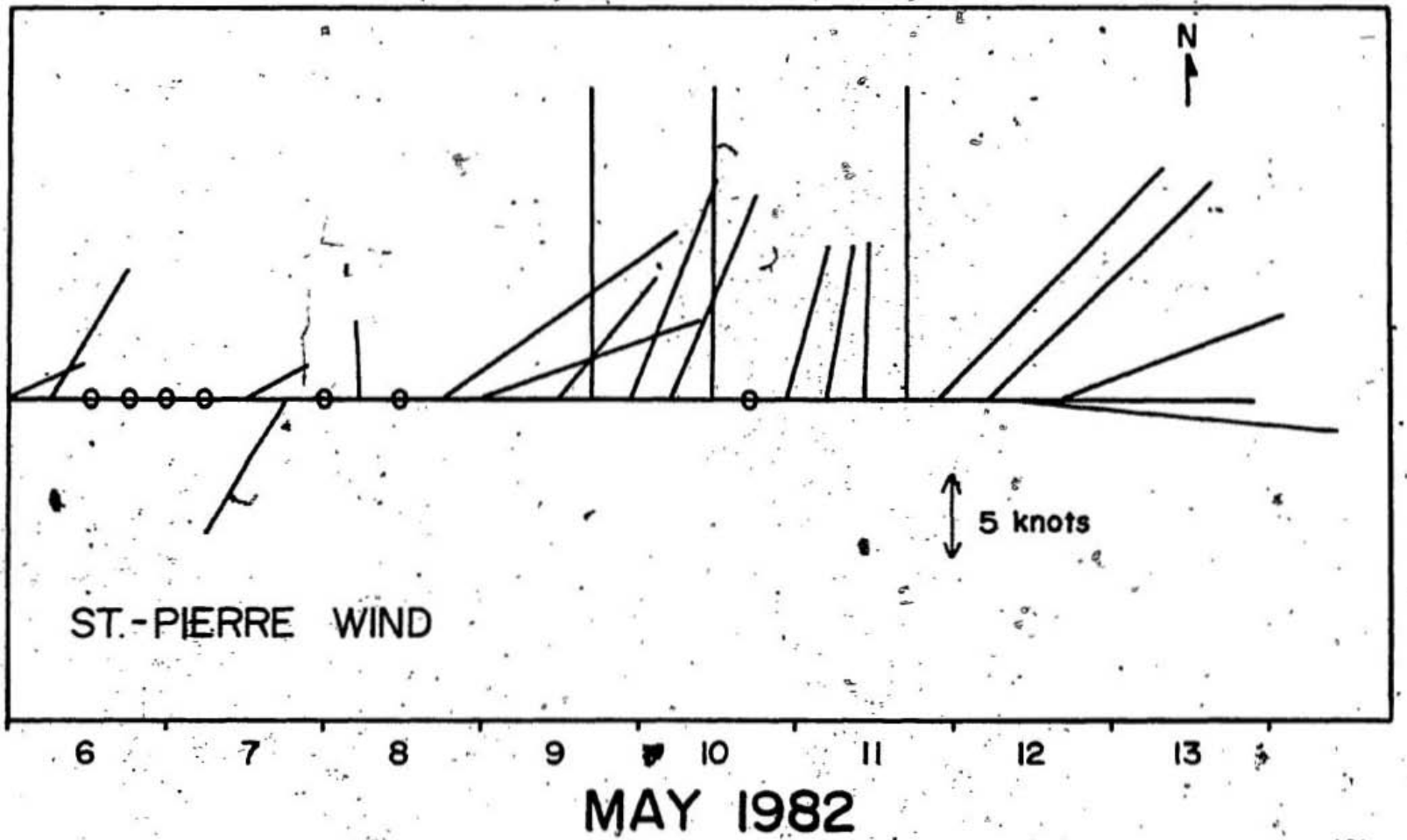


Figure 6.3 Observed wind at Saint-Pierre is plotted, in knots (1 knot = 0.5 ms), for the period when moorings M1 and M2 were in place. The open circles indicate no data.

Chapter 7 Upwelling in Hermitage Channel

7.1 Introduction

The seasonal temperature data, Figure 3.2, shows clearly that replacement of the deep water in Fortune Bay by Modified Slope Water occurs in the winter period. In Chapter 4 a correlation was drawn between this exchange and the seasonal variation in the wind stress. The data presented here do not permit the time scale over which this process occurs to be precisely resolved. Here two possible ways in which the exchange can occur will be discussed. Each involves an upwelling mechanism but one assumes a long term wind stress over a period of months where the other assumes a series of strong winds leading to intermittent periods of exchange. The wind stress data (Figure 3.4) suggests that both mechanisms could be involved.

In this chapter the two models will be applied to the Hermitage Channel system. The wind is considered to be blowing down the channel from the northeast in each of the two models. Because of the nature of the two boundaries, it is unclear whether or not this is the only wind capable of leading to upwelling of warm water into Fortune Bay. A strong wind from the west or northwest may also generate the appropriate upwelling response. The discussion of Chapter 3 does make clear, however, that a strong northeasterly wind in the winter period is a common condition.

7.2 Time-Dependent Upwelling

The approach presented here is based upon that of Gill (1982, pp.403-408). A simple two-layer system is considered, an assumption which is reasonable for the Hermitage Channel system (see Figure 4.1). Here the Modified Slope Water is associated with the lower layer. The coordinate system is illustrated in Figure 7.1 where the primed variables are in the

lower layer and the unprimed are in the upper layer. The origin of the coordinate system will be at the surface partway along the southeast side. The sill, leading into Fortune Bay, will be considered to run from the side of the channel at the point where the coordinate system is centered. The wind stress is considered to be spatially nonvarying and time independent.

The far side of the channel will be ignored because the width is much greater than the internal Rossby deformation radius a, which is the e-folding distance for the upwelling. This radius a is:

$$a = \frac{\left(\frac{g'hh'}{h+h'}\right)^{1/2}}{f} \qquad (7.1)$$

where h and h' are the upper and lower layer thicknesses and $g = g\,\frac{\rho'-\rho}{\rho}$. From Figure 4.7 appropriate values for h, h' and $\rho' - \rho$ are 125 m, [illegible] m, and 2 kg m^{-3}. This yields a value of 7 km for a in Hermitage Channel, a figure which is far less than the width of the channel, 40 km.

Terms in $\frac{\partial}{\partial y}$ will be ignored because of the length of the channel, approximately 275 km. If one considers the speed of interfacial waves propagating within the channel;

$$c' = \left(\frac{g'hh'}{h+h'}\right)^{1/2} \qquad (7.2)$$

then it will take about 1.5 days for such a wave to reach the middle of the channel from either end, since the propagation speed based upon the above formula is 1.2 m s^{-1}. The model can be applied after the time taken for an interfacial wave to travel one internal Rossby radius away from the coast, i.e. after a time $a/c' = 1/f$. This time is about 2.6 hours at this latitude, so within these time scales an infinite coastline model can be adopted.

The linear equations of motion in the upper layer can be written;

$$\frac{\partial u}{\partial t} - fv = \frac{-1}{\rho}\frac{\partial p}{\partial x} \qquad (7.3)$$

$$(7.4) \qquad \frac{\partial v}{\partial t} + fu = \frac{-1}{\rho}\frac{\partial p}{\partial y} + \frac{\partial \tau^y}{\partial z}$$

$$(7.5) \qquad 0 = \frac{-1}{\rho}\frac{\partial p}{\partial z} - g$$

The pressure in the upper layer is given by:

$$(7.6) \qquad p = \rho g(\eta - z).$$

In the lower layer the full set of linear equations are:

$$(7.7) \qquad \frac{\partial u'}{\partial t} - fv' = \frac{-1}{\rho'}\frac{\partial p'}{\partial x}$$

$$(7.8) \qquad \frac{\partial v'}{\partial t} + fu' = \frac{-1}{\rho'}\frac{\partial p'}{\partial y} + \frac{1}{\rho'}\frac{\partial \tau^y}{\partial z}$$

$$(7.9) \qquad 0 = \frac{-1}{\rho'}\frac{\partial p'}{\partial z} - g$$

Here the pressure is:

$$(7.10) \qquad p' = \rho g(\eta + h - \eta') + \rho' g(\eta' - h - z).$$

Here f is the Coriolis parameter, v the velocity along the channel, u the velocity across the channel and τ the stress. The equations are first vertically integrated, with vertically averaged velocities defined; $\bar{u}$, $\bar{v}$, $\overline{u'}$, and $\overline{v'}$. The vertically integrated continuity equations in the upper and lower layers can then be written:

$$(7.11) \qquad \frac{\partial}{\partial t}(\eta + h - \eta') + h\frac{\partial \bar{u}}{\partial x} + \frac{\partial \bar{v}}{\partial y} = 0$$

$$(7.12) \qquad \frac{\partial \eta'}{\partial t} + h'\frac{\partial \overline{u'}}{\partial x} + \frac{\partial \overline{v'}}{\partial y} = 0$$

Interfacial and bottom stresses will be ignored. The lower layer equations are then subtracted from the upper layer equations defining;

$$(7.13) \qquad \hat{u} = \bar{u} - \overline{u'} \qquad , \quad \hat{v} = \bar{v} - \overline{v'}$$

Including the combined continuity equation and dropping the $\frac{\partial}{\partial y}$ terms, as discussed earlier, the final set of equations reduces to:

$$(7.14)\quad \frac{\partial \hat{u}}{\partial t} - f\hat{v} = g' \frac{\partial \eta'}{\partial x}$$

$$(7.15)\quad \frac{\partial \hat{v}}{\partial t} + f\hat{u} = \frac{\tau_o^y}{\rho h}$$

$$(7.16)\quad \left[\frac{1}{h} + \frac{1}{h'}\right] \frac{\partial \eta'}{\partial t} + \frac{\partial \hat{u}}{\partial x} = 0$$

τ_o^y is the wind stress at the sea surface. The rigid lid approximation ($\frac{\partial \eta}{\partial t} << \frac{\partial \eta'}{\partial t}$) as well as the Boussinesq approximation have been applied.

The three equations 7.7, 7.8 and 7.9 can be reduced to a single equation in $\hat{u}$.

$$(7.17)\quad \frac{\partial^2 \hat{u}}{\partial t^2} + f^2\hat{u} - g'\left(\frac{hh'}{h+h'}\right)\frac{\partial^2 \hat{u}}{\partial x^2} = \frac{f\tau_o^y}{\rho h}$$

This equation is to be solved for an appropriate set of intial and boundary conditions. The cross-channel velocity $\hat{u}$ is expected to come to equilibrium very quickly, so the second order term $\frac{\partial^2 \hat{u}}{\partial t^2}$ may be dropped leaving the final equation:

$$(7.18)\quad g'\left(\frac{hh'}{h+h'}\right)\frac{\partial^2 \hat{u}}{\partial x^2} + \frac{f\tau_o^y}{\partial h} - f^2\hat{u} = 0$$

Boundary conditions require that $u = u' = 0$ along $x = 0$ and that u and u' should not become infinitely large as x approaches infinity. The solution is:

$$(7.19)\quad \hat{u} = \frac{\tau_o^y}{\rho f h}\left[1 - e^{\frac{-x}{a}}\right]$$

Solving for v and using equations (7.15) and (7.16) gives:

$$(7.20)\quad \hat{v} = \left[\frac{\tau_o^y}{\rho h}\right] te^{\frac{-x}{a}}$$

$$(7.21)\quad \eta' = \left[\frac{c'\tau_o^y}{\rho g' h}\right] te^{\frac{-x}{a}}$$

where c' is defined by equation (7.2).

Each of $\hat{u}$, $\hat{v}$ and η' will decay exponentially away from the coastline

within the e-folding distance defined by the internal Rossby deformation radius a. The interfacial displacement and the along-channel velocity will both increase linearly with time. $\hat{u}$ is time independent.

7.3 Steady State Upwelling

The physical situation to be modelled here is similar to that described in the previous section with the exception that the wind stress is now considered to have been imposed for long enough to allow the system to reach a steady state. As before, the coordinate system is centered at a point halfway along the channel. The walls of the channel are considered to be permeable in such a manner that continuity is ensured. The momentum equations in the upper layer will be similar to those written before.

$$(7.22) \quad -fv = \frac{-1}{\rho}\frac{\partial p}{\partial x}$$

$$(7.23) \quad fu = \frac{-1}{\rho}\frac{\partial p}{\partial y} + \frac{1}{\rho}\frac{\partial \tau^y}{\partial z}$$

In the lower layer the equations will be:

$$(7.24) \quad p = \rho g(\eta - z)$$

$$(7.25) \quad p' = \rho g(\eta + h - \eta') + \rho' g(\eta' - h - z)$$

These equations can be simplified since all the $\frac{\partial}{\partial y}$ terms are zero, a proof for which is given in Appendix III. In the steady state there is no variation in the surface or interfacial slopes along the channel. Both u and u' must also be zero since $u = u' = 0$ at the boundary $x = 0$ and no variation in x is expected. Thus, u and u' will be zero everywhere. Under these conditions the equations of motion (7.22-7.25) can be reduced to:

$$(7.28) \quad fv = \frac{\partial \eta}{\partial x}$$

$$(7.29) \quad 0 = \frac{1}{\rho} \frac{\partial \tau^y}{\partial z}$$

$$(7.30) \quad fv' = g \frac{\partial \eta}{\partial x} + g' \frac{\partial \eta'}{\partial x}$$

$$(7.31) \quad 0 = \frac{+1}{\rho'} \frac{\partial \tau^y}{\partial z}$$

Equations (7.29) and (7.31) can be integrated to give:

$$(7.32) \quad \tau_o^y - \tau_o^y = 0$$

$$(7.33) \quad \tau'^y_i - \tau_b^y = 0.$$

Equation (7.32) says that the surface stress will be balanced by the interfacial stress in the upper layer. Equation (7.33) says that the interfacial stress in the lower layer will be balanced by the bottom stress. Thus, the surface stress will be balanced by the bottom stress since the stress must be continuous across the interface. Writing the stresses in quadratic form with drag coefficients results in an equation of the form:

$$(7.34) \quad v' = \left(\frac{\rho_{air} C_D}{\rho' C_B} \right)^{1/2} \quad \text{Wind Speed}$$

This equation will permit a rough calculation of the transport in the lower layer. A similar calculation can be made for the upper layer.

The steady state case differs from the time-dependent one in that the cross-channel slope is constant. Thus, both $\frac{\partial \eta}{\partial x}$ and $\frac{\partial \eta'}{\partial x}$ are constants. In the time-dependent case these slopes take on an exponential form.

This rather straightforward approach was developed to determine whether or not steady state upwelling conditions were capable of generating a sufficient response to transport warm water into Fortune Bay. The difficulty with solving the full set of equations is with applying the full set of boundary conditions.

7.4 Application to Hermitage Channel

The next step, having worked out the theory for the two upwelling situations, is to apply the data from Hermitage Channel to the equations of the previous section. Table 7.1 presents the data for the Hermitage Channel system which shall first be applied to the time-dependent upwelling situation.

TABLE 7.1 HERMITAGE CHANNEL DATA

Upper Layer	Lower Layer	Wind
ρ 1025.0 kg m^{-3}	ρ' 1027.0 kg m^{-3}	Wind Speed 15 m s^{-1}
h 125 m	h' 175 m	C_D 1.5 x 10^{-3}

Substitution into equation 7.21 gives a result for the interfacial height of $\eta' = 2.9 \times 10^{-4}$ t(m). After a period of two days η' = 52 m. It is unfortunate, but this will not allow the computation of a transport since the cross-channel velocity is assumed to be zero along the boundary. So this assumption was made in solving the differential equation (7.18) which yielded a solution in which $\hat{u}$ goes to zero at the boundary.

Examining the temperature and density plots from the May 1982 survey it can be seen that this 15 m s^{-1} wind blowing for one day would be sufficient to raise dense water up over the sill. Thus this wind should be sufficient to initiate an inflow event.

The other possibility to be considered is that of steady state upwelling conditions where a relatively weak wind blows for an extended period of time. Such a wind field is indicated by the winter wind stresses shown in Figure 4.4 for 1979 and 1980. The transport induced by the upwelling can be determined by first computing the upchannel velocity

using equation 7.34. The upchannel transport is then estimated by multiplying the velocity v' by the height h' and the width of the channel w. This gives an upper limit to the transport since it is expected that the real boundary conditions will act to reduce this transport. The bottom friction coefficient C_B is chosen to be 2×10^{-3} (Csanady, 1982, p. 11), a value which Csanady describes as an order of magnitude estimate. Based upon Figure 3.4 a mean geostrophic wind stress of 0.3 N m^{-2} is chosen, in reasonable agreement with Saunders (1977). This corresponds to a geostrophic wind of 12 m s^{-1}, which seems high. This is reduced to 7 m s^{-1} based upon the observed wind speed at Grand Bank in the winter (see section 3.3). Based upon these values the transport will be 1.6×10^6 m^3 s^{-1}. Such a transport would be sufficient to exchange all the water in Fortune Bay below 150 meters in just 2.5 days. This indicates that the computed transport is indeed an upper limit although it clearly shows the feasibility of this mechanism to cause Modified Slope Water inflow.

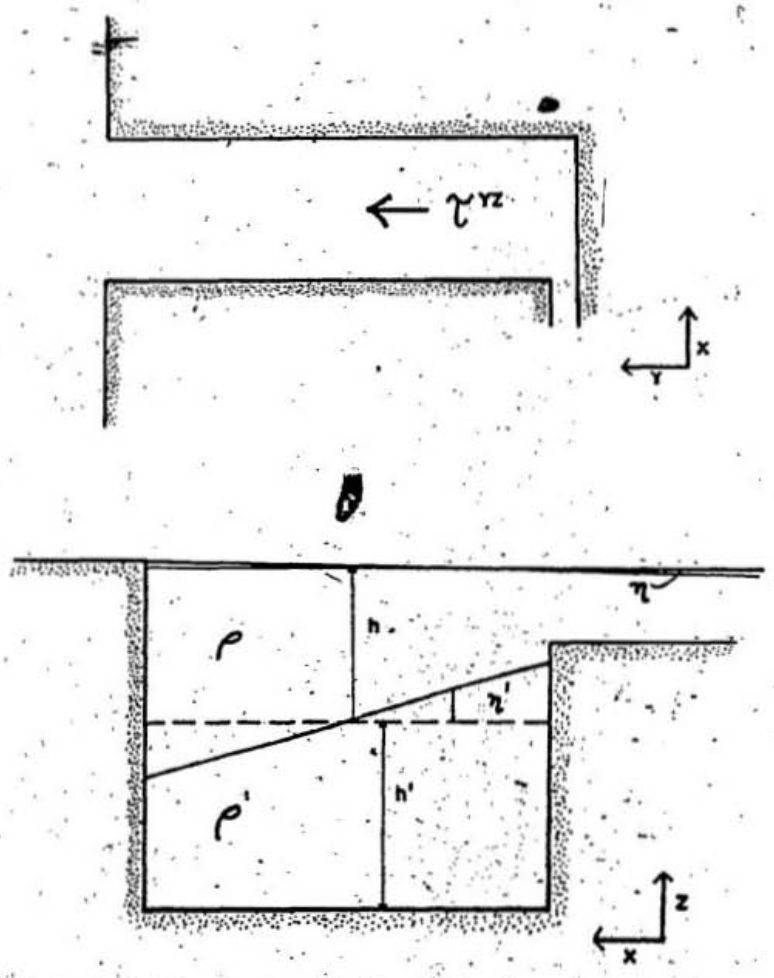


Figure 7.1 Schematic for both the time-dependent and steady state upwelling analysis. The sill, indicated in the lower diagram, is located, for the purposes if the analysis, partway down the channel. The coordinate axis is centered at the surface along the boundary over the sill.

Chapter 8 Summary and Conclusions

Seasonal variation in the surface wind has been related to a seasonal variation in the bottom temperatures of Fortune Bay. Light winds from the southwest occur in the summer when the bottom temperature in the bay is comparatively cold. Strong winds from the northeast occur in the winter when bottom temperatures are comparatively warm.

A description of the water structure and seasonal circulation in Hermitage Channel is presented. A strong, but variable, outflow of cold Labrador Current Water from Saint-Pierre Channel was detected. The transport in the channel in May 1982 was observed to be 5.2×10^4 m^3 s^{-1}. This outflow was not observed in the May 1983 cruise.

Upwelling in Hermitage Channel in response to a northeasterly wind is shown to be capable of generating sufficient transport to exchange the deep water in Fortune Bay. Two different upwelling mechanisms are proposed for Modified Slope Water inflow over the Miquelon sill; a steady state model in which winds blow for a long enough period of time that steady state conditions are reached (about 4 or 5 days) and the other a time-dependent model in which strong winds blow for a relatively short period of time, a few days. It was not determined which was the predominant mechanism.

Dense water inflow over the Saint-Pierre sill is described as a density current flow (e.g. Bo Pederson, 1980). The results of analysis of this flow are in substantial agreement with earlier work done on density current inflows in fjords (Geyer and Cannon, 1982; Edwards and Edelsten, 1977). The inflow is observed to oscillate tidally with peak velocities associated with flooding to high tide and minimum velocities with ebb to low tide.

An analysis of the effect of flow in the upper layer on the density current inflow showed that a flow in the upper layer which is 1 to 4 times that of the density current inflow speed but in the opposite direction is capable of arresting the inflow.

Transport of Labrador Current Water into the bay in June 1982 was computed to be 1.2×10^4 m^3 s^{-1} using the observed current speeds. The total transport of the Labrador Current in Saint-Pierre Channel was therefore found to be 6.4×10^4 m^3 s^{-1} which compares reasonably well with the value of 10×10^4 m^3 s^{-1} estimated by Petrie and Anderson (1983).

More detailed observations of the density current inflow are required to determine a number of factors. The relationship between the inflow and the tide and any forcing function in the coastal water outside the Saint-Pierre sill must be more clearly established. Further current measurements combined with wind data from Saint-Pierre would help to resolve this.

Direct observation of the Hermitage Channel system together with measurement of the surface winds would make it possible to directly observe the effect of wind upon the system and to determine whether steady state or time-dependent upwelling is the predominant mechanism driving the exchange.

REFERENCES

Akenhead, S.A, B.D. Petrie, C.K. Ross and D.W. Ware (1981) Ocean Climate and Marine Fisheries of Atlantic Canada: An assessment. Bedford Institute of Oceanography Rep. Series BI-R-81-8, 121pp.

Bell, W.H. (1973) The exchange of deep water in Howe Sound Basin. Pacific Marine Science Report 73-13, 35pp.

Benjamin, T.B. (1968) Gravity Currents and Related Phenomena. J.Fluid Mech., 31, 20-248.

Berteaux, H.O. (1976) Buoy Engineering. Wiley Interscience, New York, 313 pp.

Bo Pederson, F.(1980) A monograph on turbulent entrainment and friction in two layer stratified flow. Inst. of Hydrodynamics and Hydraulic Eng., Technical University of Denmark, 397 pp.

Canadian Normals (1975) Canada. Dept. of Environment. Atmospheric Environment Service. Volume 3: Wind, 1941-1970. Downsview.

Canadian Hydrographic Service (1982) Atlantic Coast and Bay of Fundy Tide and Current Tables. Fisheries and Oceans, Ottawa, 53 pp.

Csanady, G.T. (1979) The pressure field along the western margin of the North Atlantic. J. Geophysical Res. 84, 4905-5915.

Dodge, J.(1982) A CTD System Software Package. B.Sc. Honours Thesis (unpublished), Memorial University, 55 pp.

Edwards, A. and D.J. Edelsten (1977) Deep water renewal of Loch Etive. Estuarine and Coastal Marine Science, 5, 575-595.

Ellison,T.H. and J.S.Turner (1959) Turbulent entrainment in stratified flows. J. Fluid Mech., 6, 423-448.

El-Sabh, M.I. (1977) Oceanographic features, currents and transport in Cabot Strait. J. Fish. Res. Bd. Can., 34, 516-528.

Farmer, D.M. and Freeland, H.J. (1983) The physical oceanography of fjords. Progress in Oceanography, 12, 147-220.

Fomin, L.M. (1964) The dynamic method in oceanography. Elsevier Publishing, Amsterdam, 211 pp.

Forbes, A.M.G. and J.A. Church (1980) The effects of compass calibration on Aanderaa current meter records. Div. Fish. Oceanogr. Rep. 121, 8 pp.

Gade, H.G. and A. Edwards (1980). Deep water renewal in fjords, in Fjord Oceanography edited by H.J. Freeland, D.M. Farmer and C.D. Levings, Plenum, New York, 453-489.

Geyer, W.R. and G.A. Cannon (1982) Sill processes related to deep water exchange in a fjord. J. Geophysical Res., 87, 7985-7996.

Gill, A.E. (1982) Atmostphere-Ocean Dynamics. Academic Press, New York, 662 pp.

Godin, G. (1972) The analysis of tides. University of Toronto Press, Toronto, 264 pp.

Hamblin, P.F. and Carmack, E.C. (1978) River-induced currents in a fjord lake. J. Geophysical Res., 83, 885-897.

Hay, A.E. (1983) On the frontal speeds of internal gravity surges on sloping boundaries. J. Geophysical Res., 88, 751-753.

Heggie, D.T. and D.C. Burrell (1981) Deep water renewals and oxygen consumption in an Alaskan fjord. Estuarine and Coastal Shelf Science, 13, 83-99.

Helle, H.B. (1978) Summer replacement of deep water in Byfjord, Western Norway: Mass exchange across the sill induced by coastal upwelling, in Hydrodynamics of Estuaries and Fjords. Edited by J.C. Nihoul, Elsevier Publishing, Amsterdam, 441-464.

Huyer, A. and A. Verney (1975) Temperature, salinity and sigma-t at Station 27 (47° 33N, 52° 35W), 1950-1959. Marine Environment Data Service, Technical Report No. 3, 45 pp.

Keeley, J.R. (1981) Temperature, salinity and sigma-t at Station 27 (47° 33N, 52° 35W). An analysis of historical data. Marine Environmental Data Service, Technical Report No. 3, 56 pp.

Keenan, P.V. (1979) Sources of compass error within the Aanderraa recording current meter: Revised 1979. Bedford Institute of Oceanography Report Series B1-R-79-6, 70 pp.

Keenan, P.V. (1981) Aanderaa recording current meter compass error caused by mooring system components. Bedford Institute of Oceanography Report Series B1-R-81-6, 27 pp.

Kudlo, B.P. and V.V. Burmakin (1972) Water circulation in the South Labrador and Newfoundland areas in 1970-71. Commission for the Northwest Atlantic Fisheries Res. Doc. 72/104.

Lauzier, L.M. and R.W. Trites (1958) The deep waters in the Laurentian Channel. J. Fish. Res. Bd. Can., 15, 1247-1257.

McLellan, H.J. (1957) On the distinctness and origin of the slope water off the Scotian shelf and its easterly flow south of the Grand Banks. J. Fish. Bd. Can., 14, 213-219.

Matthews, J.B. (1981) The seasonal circulation of the Glacier Bay, Alaska fjord system. Est. Coastal and Shelf Sci., 12, 679-700.

Middleton, G.V. (1966) Experiments on density and turbidity currents I. Motion of the head. Can. J. of Earth Sci., 3, 523-546.

Millero, F.J. and A. Poisson (1981) International one-atmosphere equation of state for seawater. Deep-Sea Research, 28, 625-629.

Murray, A.R. and T.J. Harmon (1969) A preliminary consideration of the factors affecting the productivity of Newfoundland streams. Fisheries Res. Bd. of Canada Tech. Rep. No. 130, 405 pp.

Nelson, C.S. (1977) Wind stress and wind stress curl over the California Current. U.S. Dep. Commer., NOAA Tech. Rep. NMFS -714, 87 pp.

Petrie, B. and C. Anderson (1983). Circulation on the Newfoundland Continental Shelf. Atmosphere-Ocean 21, 207-226.

Pickard, G.L. (1963) Oceanographic characteristics of inlets of Vancouver Island, B.C., J. Fish, Res. Bd. Can., 24, 1475-1506.

Pond, S. (1975) The exchange of momentum, heat and moisture at ocean-atmoshpere interface. Numerical Models of Ocean Circulation, Nat. Acad. Sci, 26-38.

Pond, S. and G.L. Pickard (1978) Introductory Dynamic Oceanography. Pergamon Press, Oxford, 241 pp.

Reid, J.L. and A.W. Mantyla (1976) The effect of the geostrophic flow upon the coastal elevations in the northern North Pacific Ocean. J. Geophysical Res., 81, 3100-3110.

Saunders, P.M. (1977) Wind stress on the ocean over the eastern continental shelf of North America. J. Phys. Ocean., 7, 555-566.

Simpson, J.E. (1982) Gravity currents in the laboratory, atmosphere and ocean. Ann. Rev. Fluid Mech., 14,213-234.

Smith, P.C. (1975) A streamtube model for bottom boundary currents in the ocean. Deep-Sea Research, 22, 853-873.

Strickland, J.D.H. and T.R. Parsons (1972) A Practical Handbook of Seawater Analysis. Fish. Res. Bd. Can. Bull, 167, 310 pp.

Stucchi, D.J. and Farmer, D.M. (1976) Deep water exchange on Rupert-Holberg inlet. Pacific Marine Science Report 76-10, 32 pp.

SUN Report, IUGG Publication Office, Paris, (1979).

Trites, R.W. (1971) The gulf as a physical oceanographic system. in E.M. Hassan (coord.) Proc. 2nd Gulf of St. Lawrence Workshop, Bedford Institute of Oceanography, Dartmouth, N.S., 32-63.

Turner, J.S. (1973) Buoyancy Effects in Fluids. Cambridge University Press, Cambridge, 368 pp.

Appendix I: Station Positions

These stations are those occupied during the 1982 cruises. There will be small differences in the earlier cruises, generally less than one kilometer; so for the purposes of labelling stations on the plots the same numbers will be used. The position of the stations on the plots is based upon the actual position for the cruise.

CTD STATIONS

NUMBER	STATION	LATITUDE (°N)	LONGITUDE (°W)	DEPTH (m)
1	Fo1	47 35.75	54 56.0	417
2	BeB1	47 39.5	55 24.8	524
3	BeB2	47 36.8	55 14.4	547
4	Fo2	47 31.36	55 12	355
5	Fo2.5	47 24.0	55 28	424
6	Fo3	47 15.03	55 36	380
7	Fo4	47 15.24	55 47.6	360
8	Fo5	47 06.8	56 01.17	322
9	SP1	47 00.0	56 06.5	183
10	SP2	46 54.3	56 08.4	174
11	SP3	46 45.4	56 04.3	134
12	SP20	46 42.7	55 48.2	115
13	SP21	46 41.1	55 53.0	156
14	SP22	46 39.2	55 59.4	137
15	SP23	46 37.6	56 04.6	101
16	SP30	46 34.8	56 12.4	101
17	SP31	46 32.7	56 15.1	121
18	SP32	46 29.7	56 17.8	99
19	SP5	46 40.4	56 24.6	104
-	SP6	46 44.6	56 36.75	101
20	SP7	46 49.9	56 42.7	102
21	HC55	47 00.2	57 16.5	300
22	LA5	46 06.8	58 37.1	293
23	LA4	46 14.9	58 23.8	406
24	LA2	46 33.5	57 53.4	448
25	LA2	46 33.5	57 53.4	448
26	LA1	46 40.2	57 41.8	330
27	HC66	47 01.3	57 42.5	160
28	HC65	46 58.5	57 38.5	220
29	HC64	46 56.2	57 35.2	284
30	HC63	46 52.5	57 30.0	324
31	HC62	46 48.8	57 25.0	271
32	HC61	46 46.6	57 21.5	220

33	HC60	46 43.8	57 17.5	114
34	HC54	47 19.6	57 11.6	234
35	HC53	47 13.6	57 08.2	265
36	HC52	47 07.2	57 01.3	344
37	HC51	47 01.7	56 55.5	240
38	HC50	47 56.9	56 50.8	119
39	HC43	47 19.3	56 48.2	316
40	HC42	47 15.0	56 43.0	375
41	HC41	47 09.5	56 38.0	240
42	HC40	47 04.6	56 33.8	119
43	HC33	47 25.0	56 39.8	260
44	HC32	47 21.1	56 33.0	384
45	HC31	47 16.1	56 25.7	240
46	HC30	47 12.4	56 18.6	119
47	HC22	47 20.8	56 22	263
48	HC21	47 31.5	56 28.3	256
49	SA5	47 24.5	56 19.2	296
50	HC20	47 28.6	56 24.5	375
51	HC10	47 32.0	56 21.0	375
52	HB8	47 35.3	56 15.6	311
53	SA4	47 22.0	56 07.3	192
54	F08	47 17.5	56 08.0	124
55	F07	47 11.7	56 10.7	150
56	F06	47 09.0	56 10.96	117
57	SA3	47 23.2	55 54.0	254
58	SA2	47 24.6	55 46.0	254
59	SAI	47 23.7	55 42.0	88
60	SA0.5	47 22.4	55 40.4	128
61	SP51	46 35.0	55 27.5	139
62	PA1	45 34.0	54 55.6	231

TRANSECT 4 - T4

NUMBER	STATION	LATITUDE (°N)	LONGITUDE (°W)
T4-1	SP 80	46 53.26	56 07.35
T4-2	SP 81	46 53.27	56 07.68
T4-3	SP 82	46 53.28	56 08.0
T4-4	SP 83	46 53.30	56 08.32
T4-5	SP 84	46 53.31	56 08.62
T4-6	SP 85	46 53.32	56 08.94
T4-7	SP 86	46 53.33	56 08.25

CURRENT METER MOORING LOCATIONS

NUMBER	LATITUDE (°N)	LONGITUDE (°W)	DEPTH (m)
M1	47 08.2	56 08.41	146
M2	47 12.1	56 09.9	146
M3	46 57.12	56 08.3	176

SEASONAL DATA STATIONS

NUMBER	LATITUDE (°N)	LONGITUDE (°W)	DEPTH (m)
L1	46 28	54 54	210
L2	46 33	56 03	160
L3	46 44	56 34	100
STN27	47 33	52 35	176

TRANSECT 1 - T1

NUMBER	STATION	LATITUDE (°N)	LONGITUDE (°W)	DEPTH (m)
T1-1	FO 40	47 15.9	55 48.2	300
T1-2	FO 41	47 14.8	55 47.0	300
T1-3	FO 42	47 14.2	55 46.5	200
T1-4	FO 43	47 13.0	55 45.3	180
T1-5	FO 44	47 11.75	55 44.0	250
T1-6	FO 45	47 11.4	55 43.7	320
T1-7	FO 46	47 11.0	55 43.3	250
T1-8	FO 47	47 10.8	55 43.0	200
T1-9	FO 48	47 10.3	55 42.5	140

TRANSECT 2 - T2

NUMBER	STATION	LATITUDE (°N)	LONGITUDE (°W)
T2-1	SP 60	46 58.67	56 02.56
T2-2	SP 61	46 59.12	56 03.9
T2-3	SP 62	46 59.58	56 05.3
T2-4	SP 63	46 59.8	56 05.91
T2-5	SP 64	46 59.9	56 06.2
T2-6	SP 65	46 00.0	56 06.5
T2-7	SP 66	46 00.09	56 06.8
T2-8	SP 67	46 99.19	56 07.05

TRANSECT 3 - T3

NUMBER	STATION	LATITUDE (°N)	LONGITUDE (°W)
T3-1	SP 70	46 56.6	56 07.3
T3-2	SP 71	46 56.6	56 07.62
T3-3	SP 72	46 56.6	56 07.95
T3-4	SP 73	46 56.6	56 08.25
T3-5	SP 74	46 56.6	56 08.60
T3-6	SP 75	46 56.61	56 08.90
T3-7	SP 76	46 56.61	56 08.3

APPENDIX II

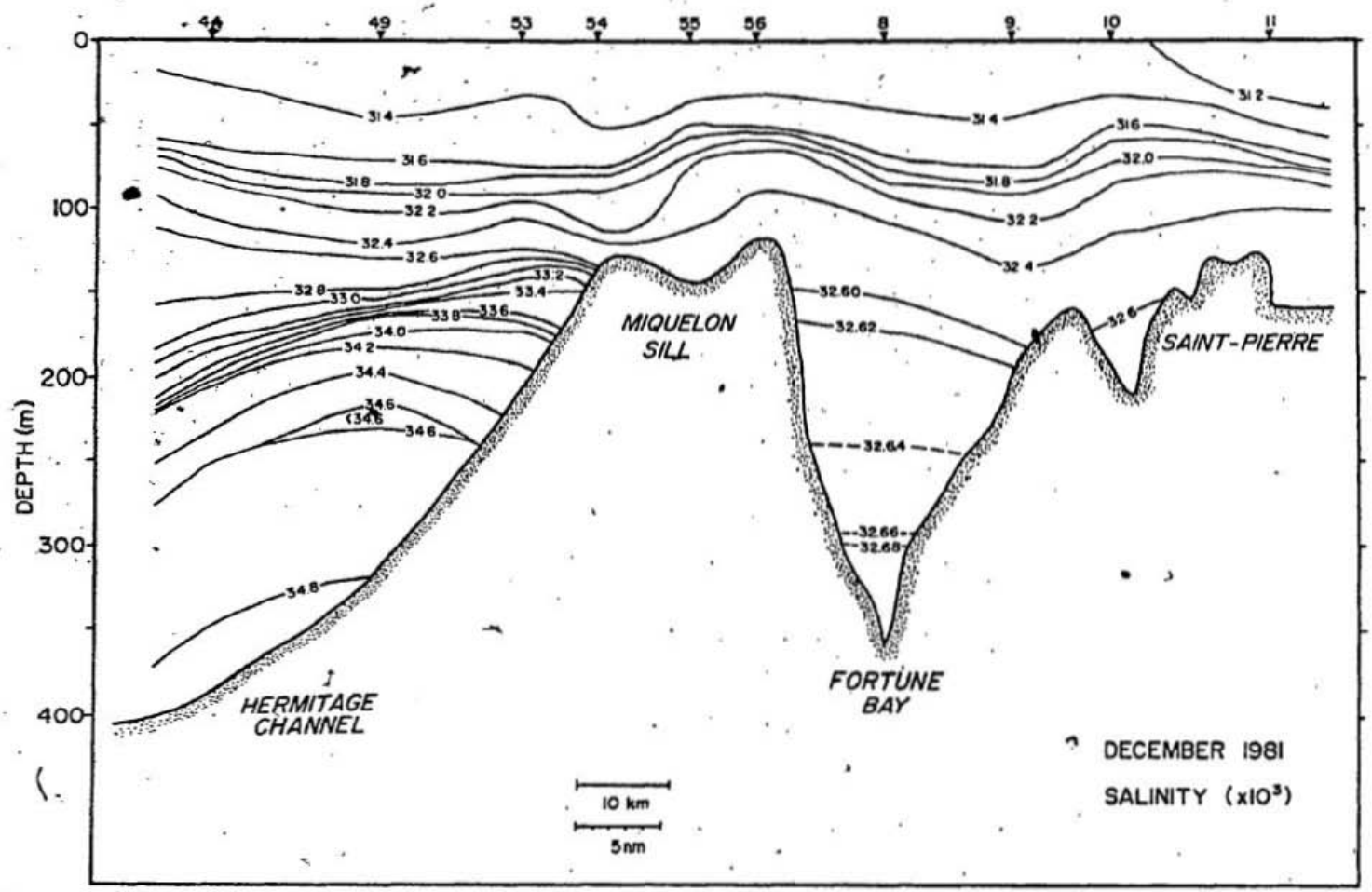


Figure A2.1 Salinity from Saint-Pierre to Hermitage Channel, December 1981.

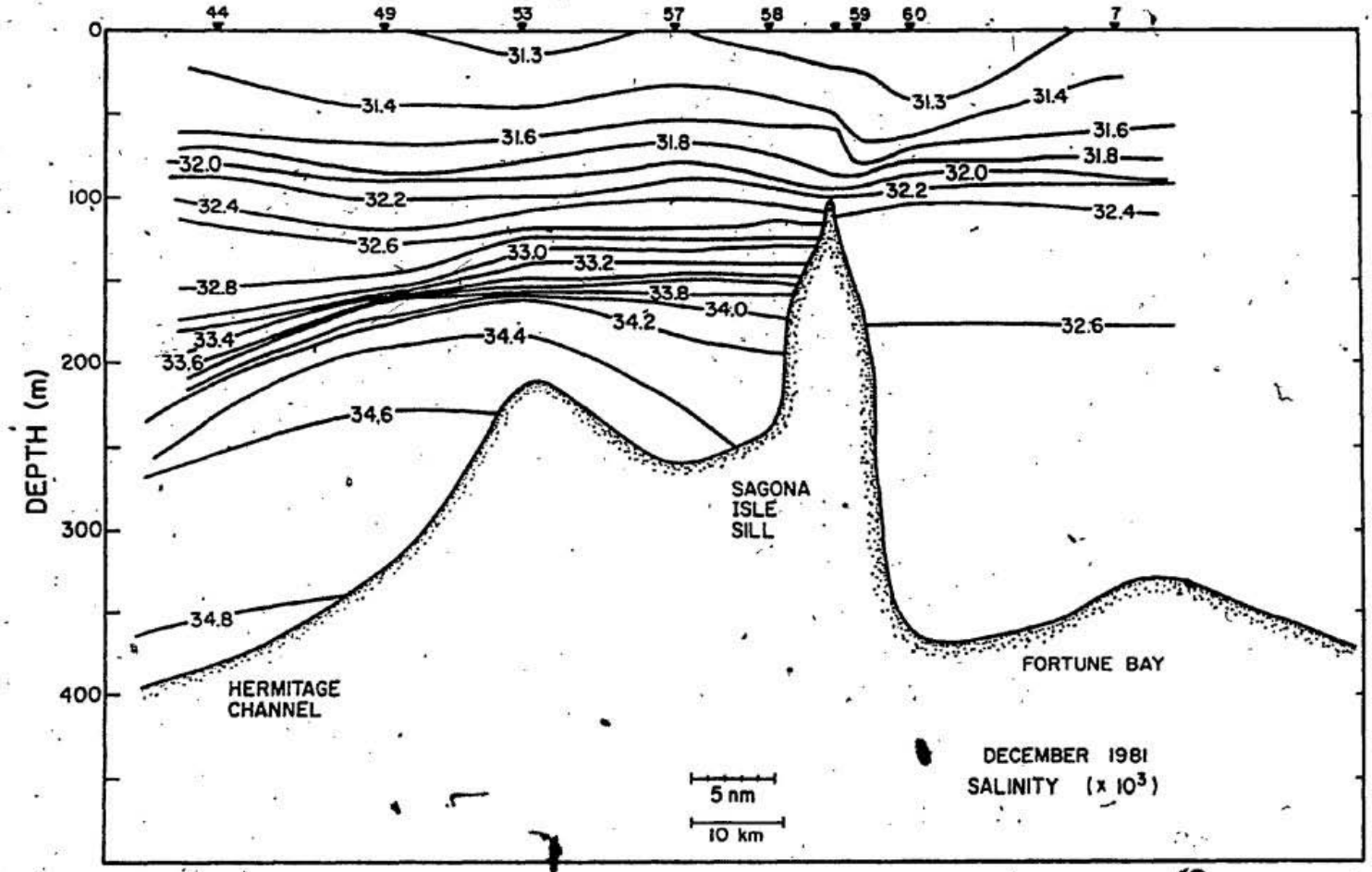


Figure A2.2 Salinity across Sagona sill, December 1981.

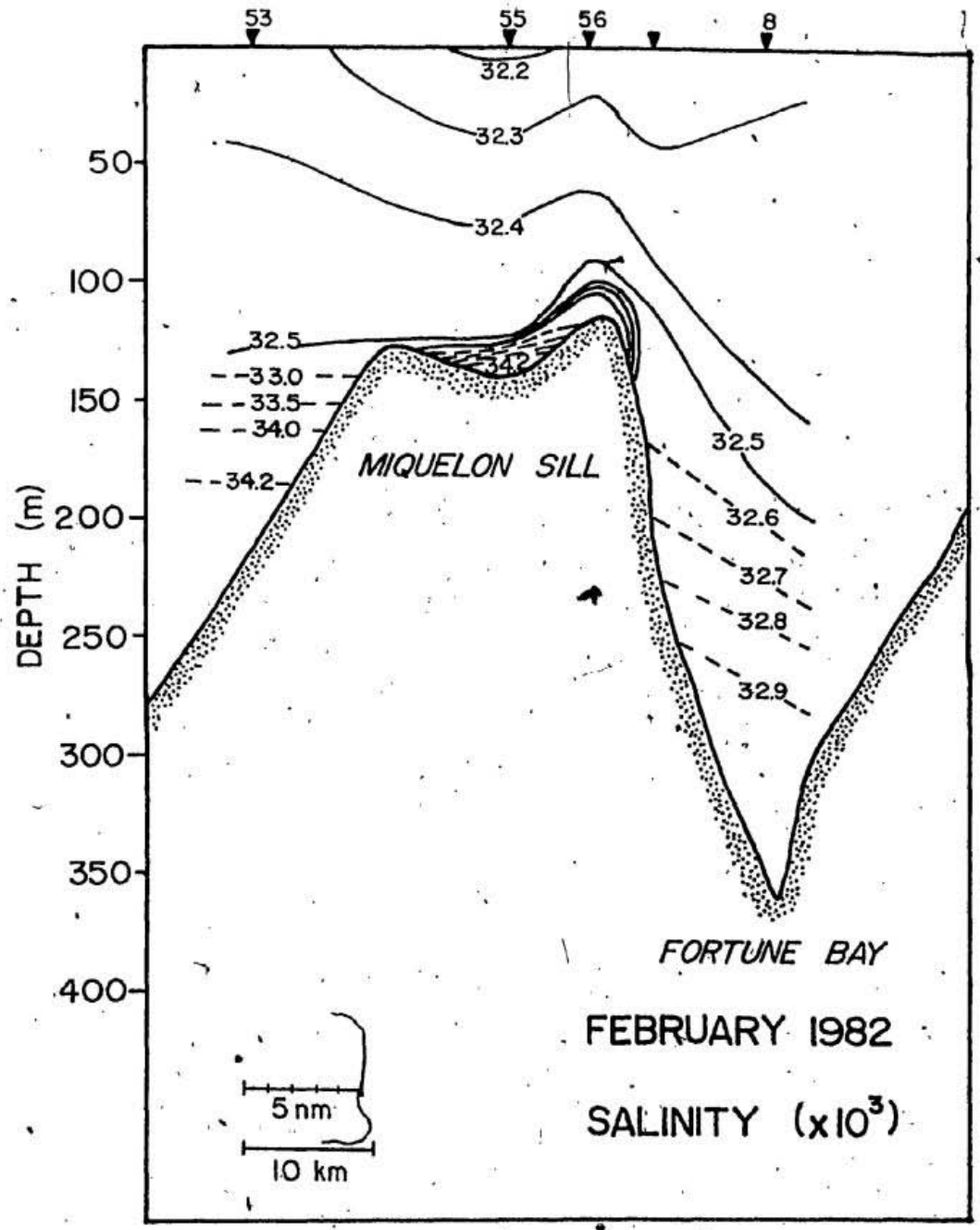


Figure A2.3 Salinity across Miquelon sill, February 1982.

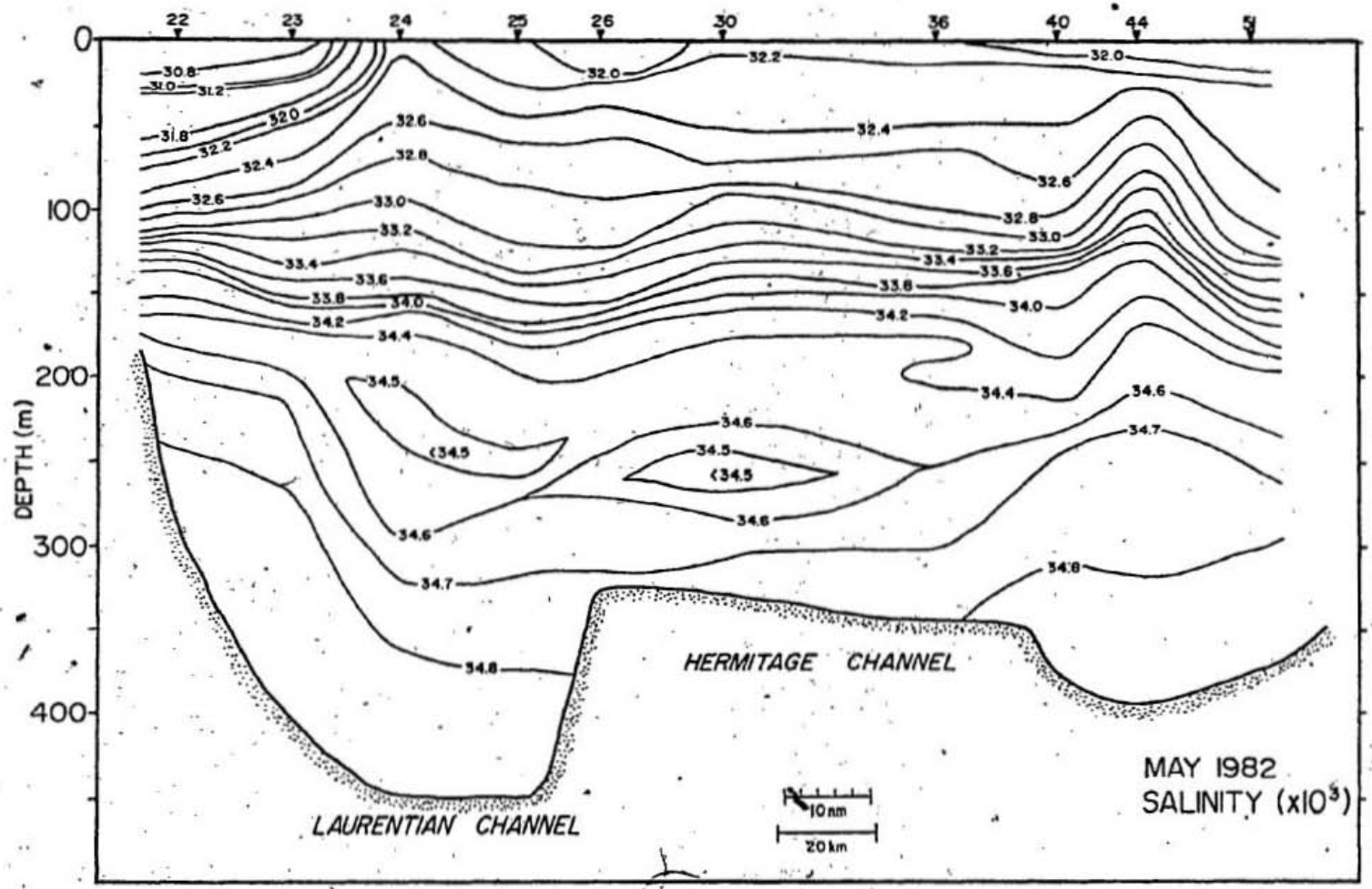


Figure A2.4 Salinity along Hermitage Channel, May 1982.

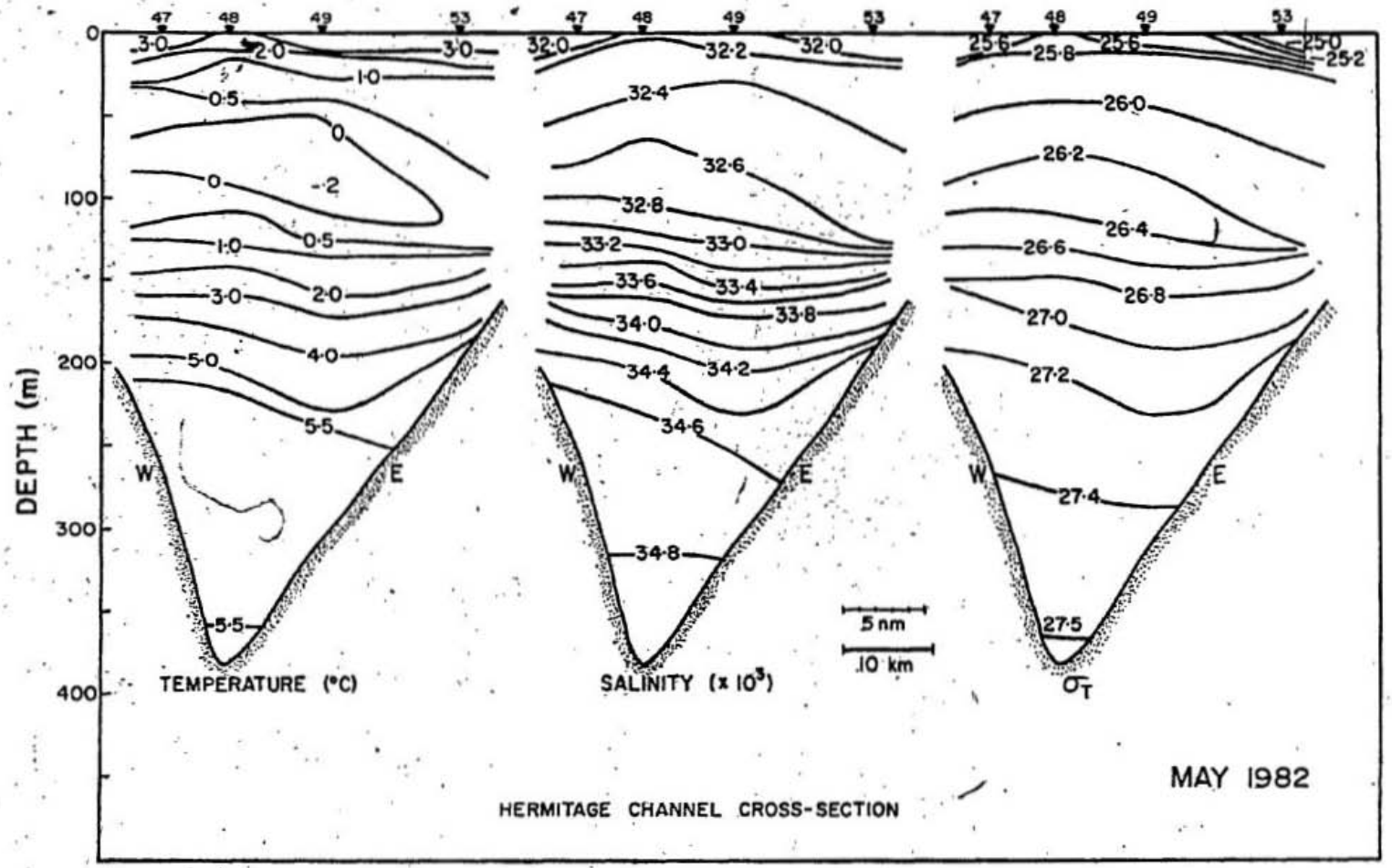


Figure A2.5 Transect across Hermitage Channel, stations 47-53, May 1982.

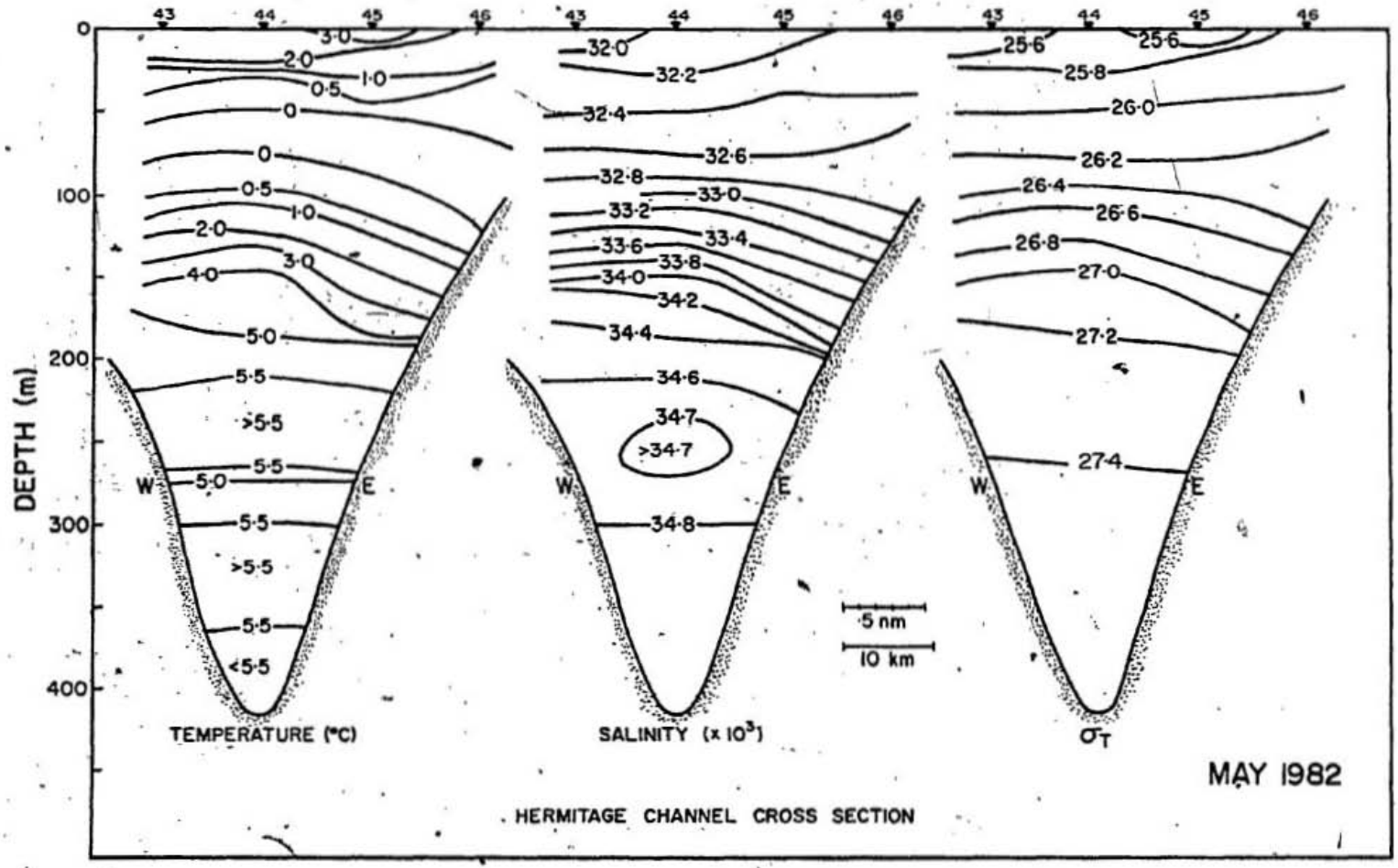


Figure A2.6 Transect across Hermitage Channel, stations 43-46, May 1982.

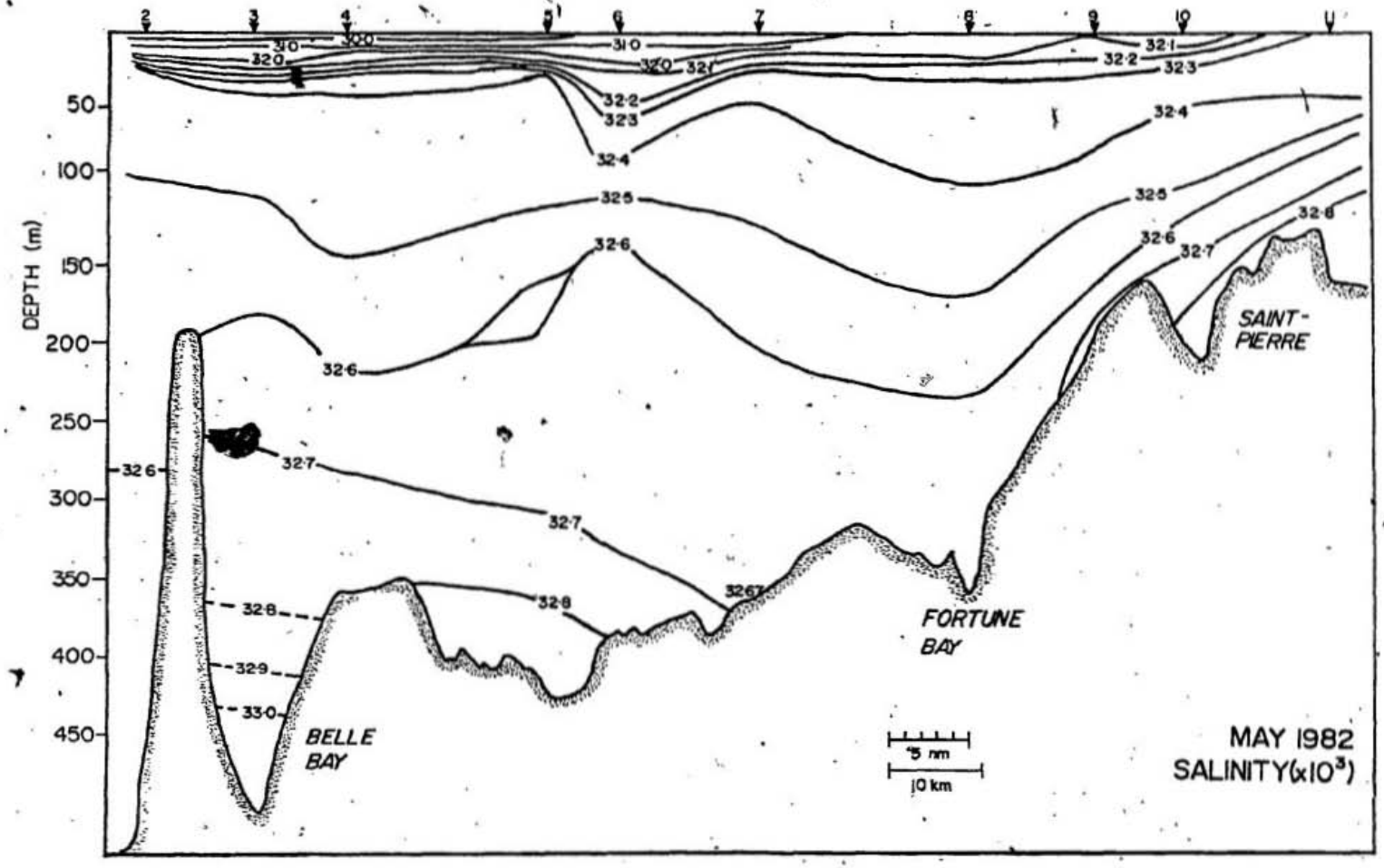


Figure A2.7 Salinity along Fortune Bay, May 1982.

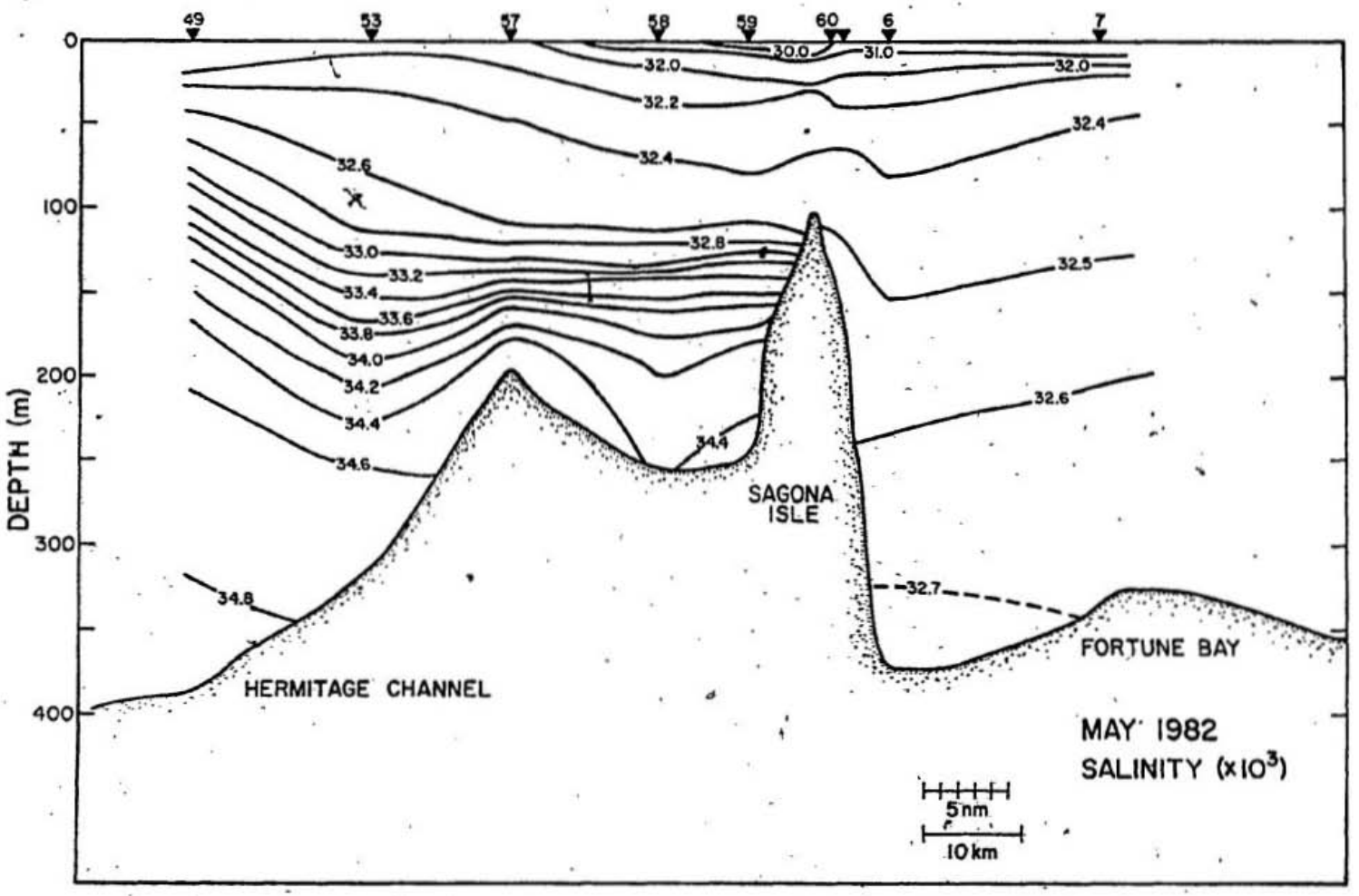


Figure A2.8 Salinity across Sagona sill, May 1982.

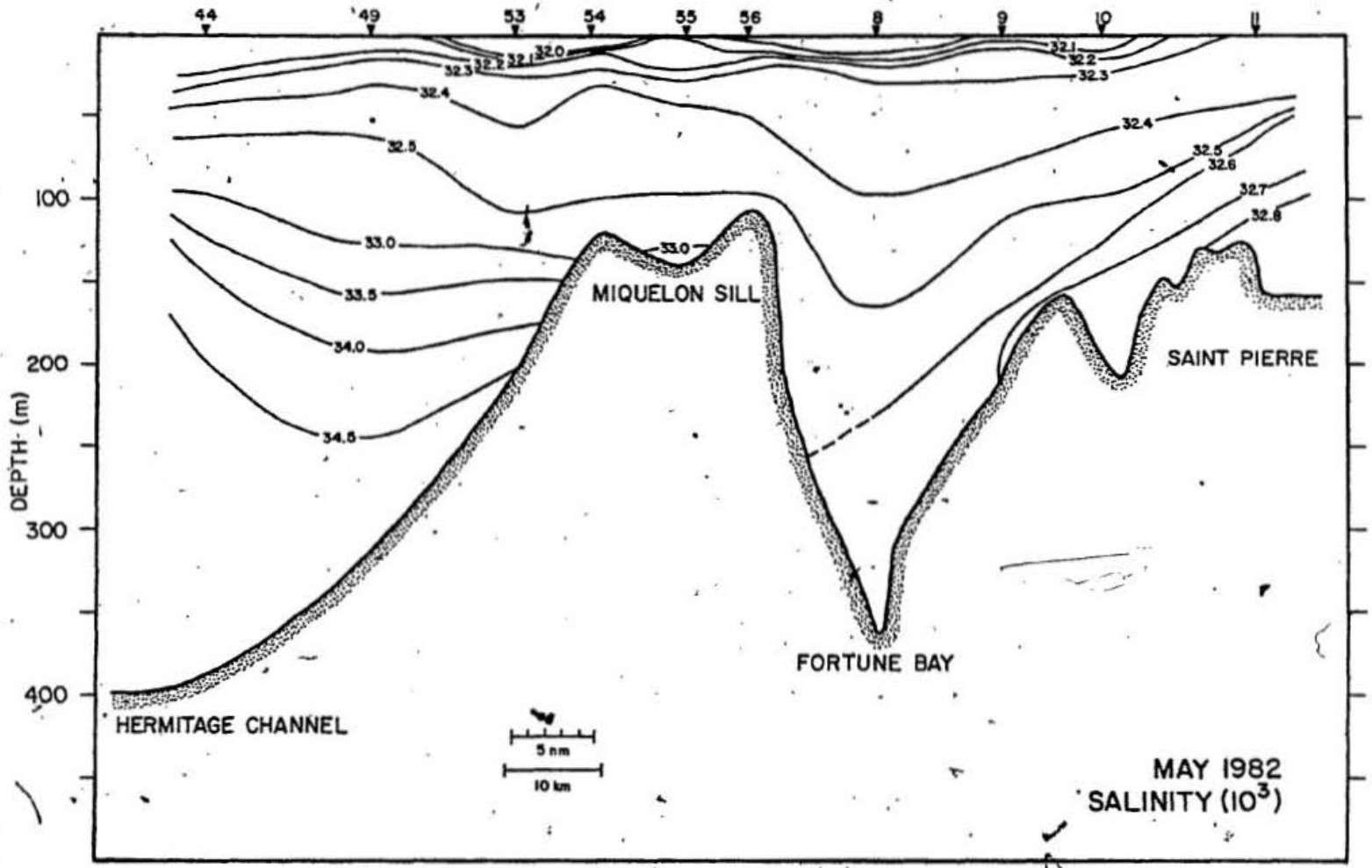


Figure A2.9 Salinity from Saint-Pierre to Hermitage Channel, May 1982.

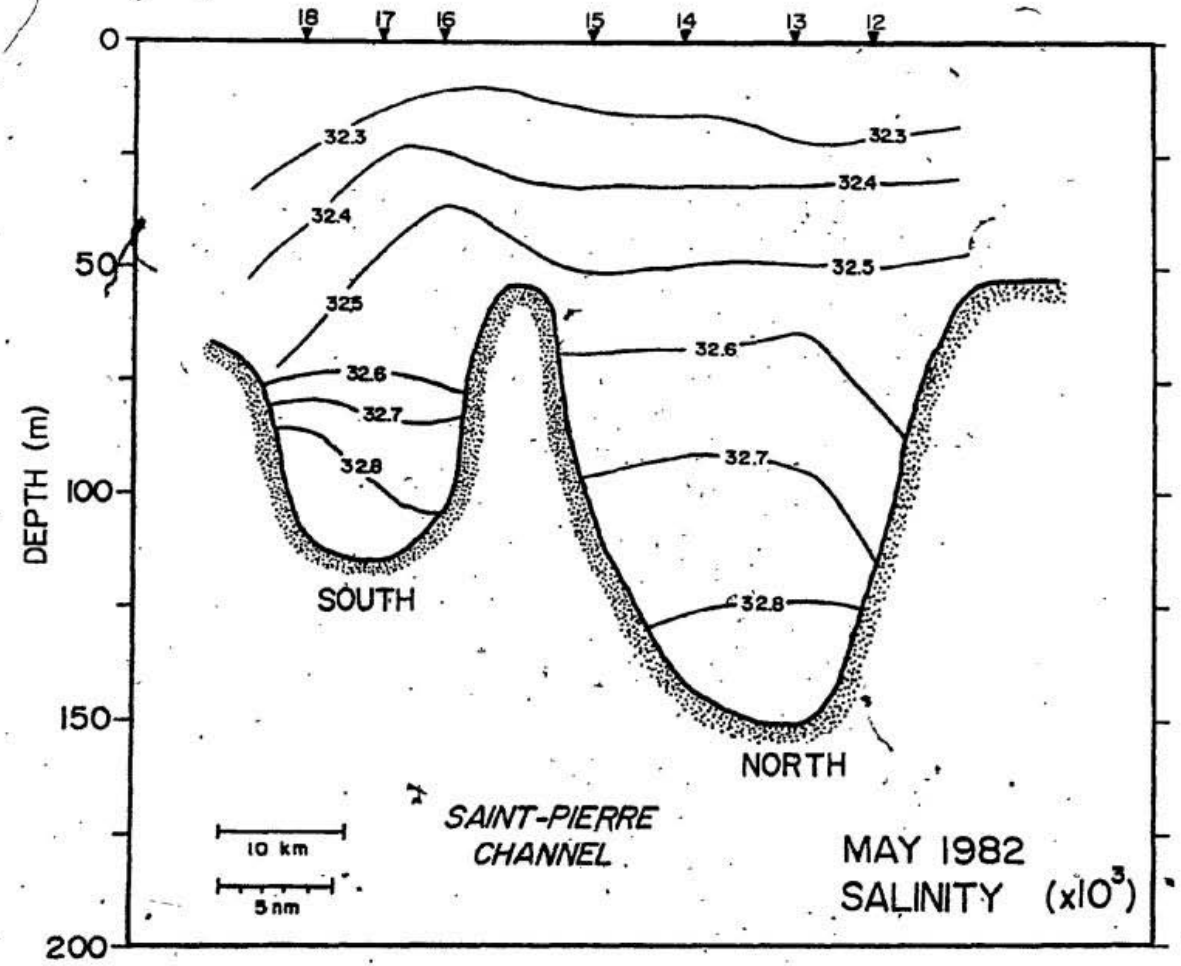


Figure A2.10 Salinity in Saint-Pierre Channel cross section, May 1982.

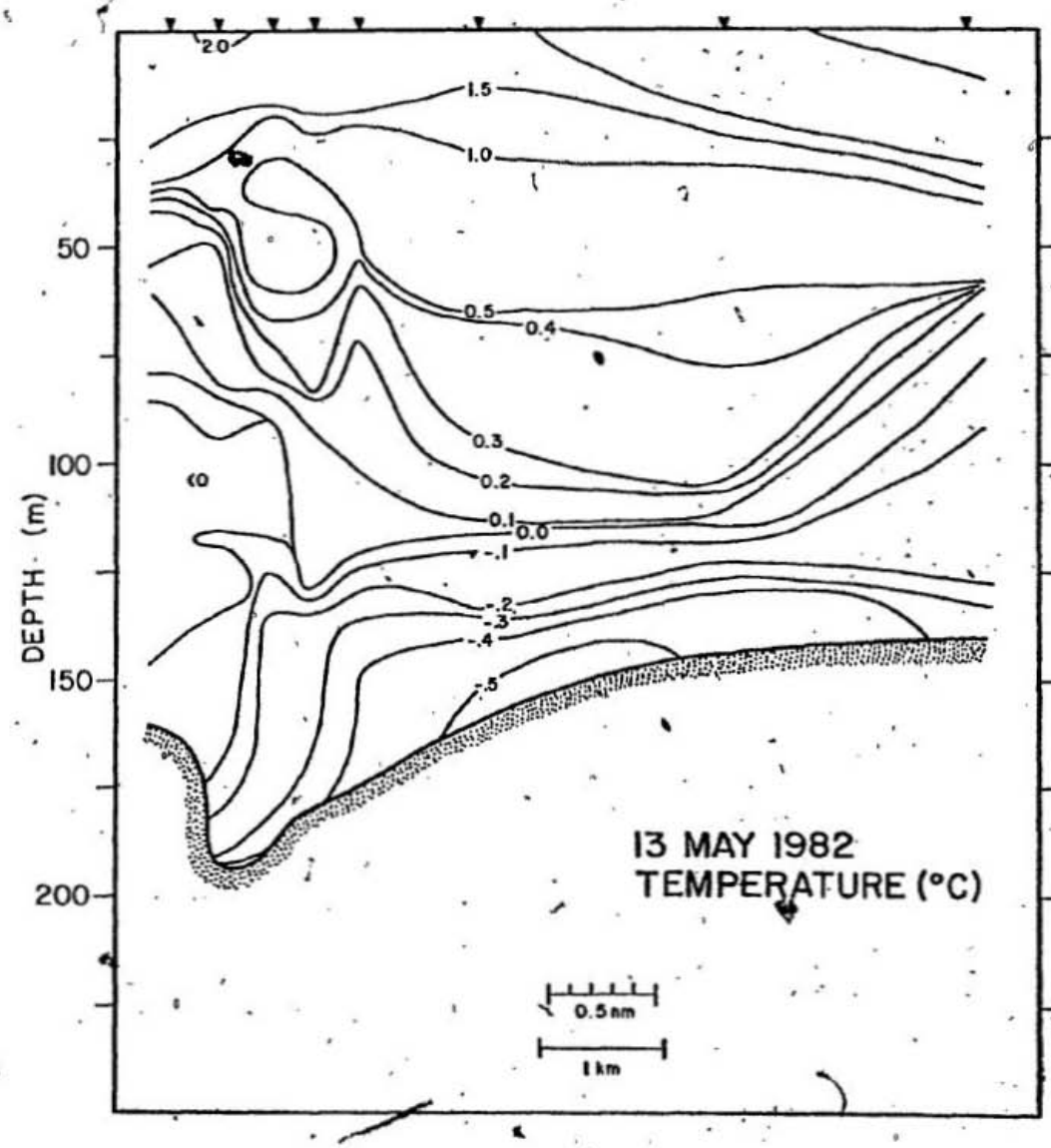


Figure A2.11 Temperature along transect T2 looking into the bay, May 1982.

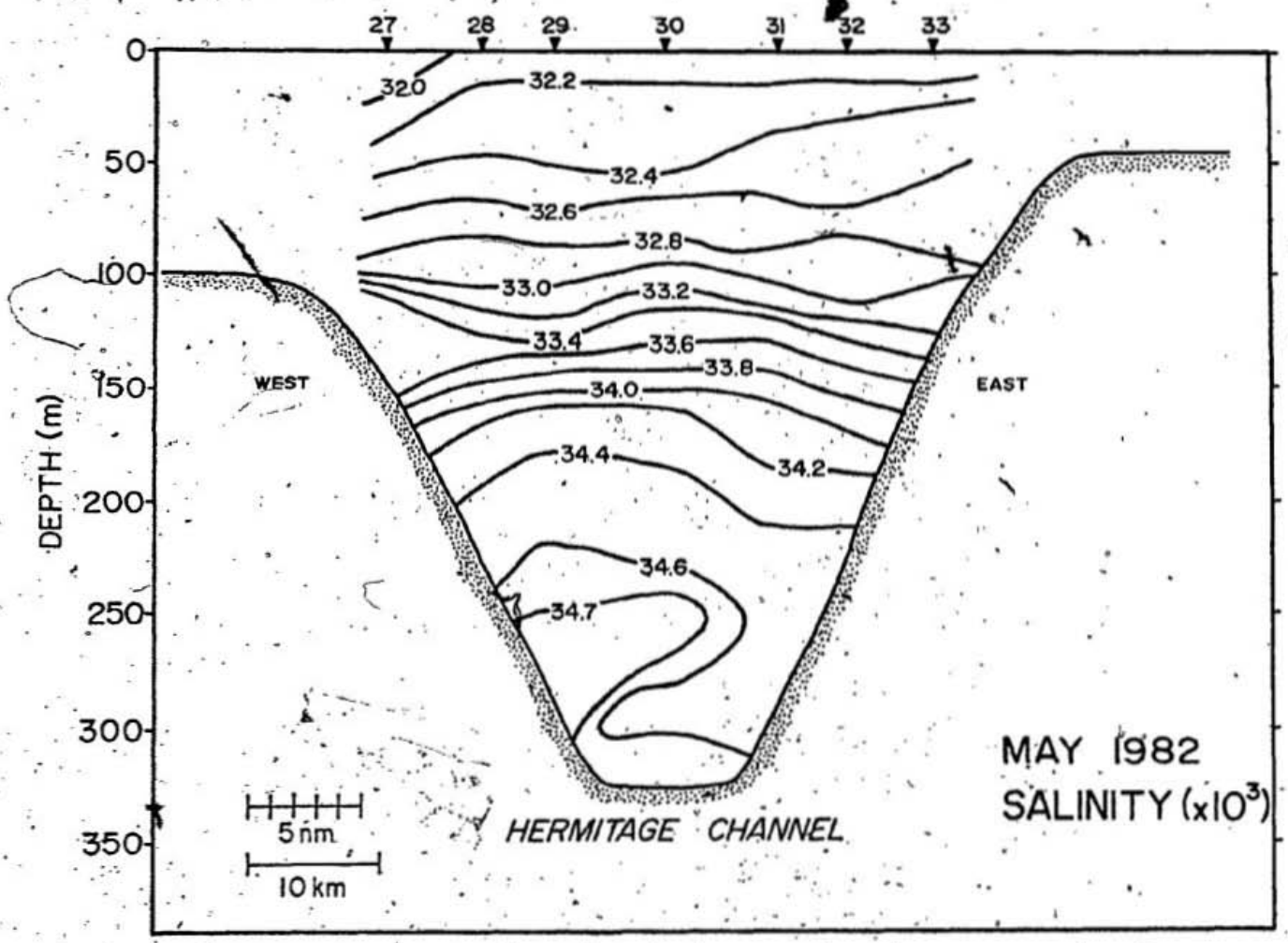


Figure A2.12 Salinity across the mouth of Hermitage Channel, May 1982.

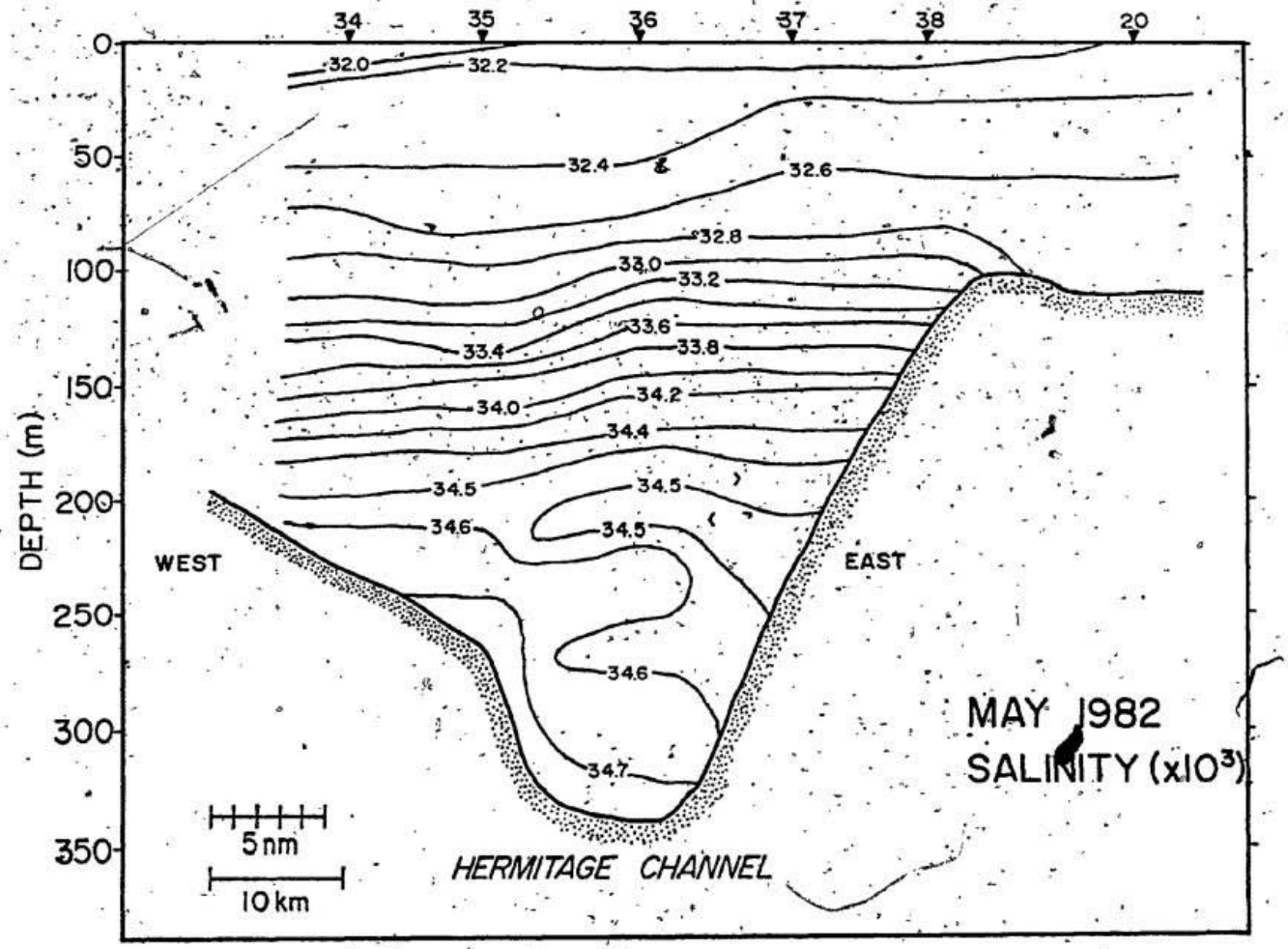


Figure A2.13 Salinity across Hermitage Channel, stations 34-20, May 1982.

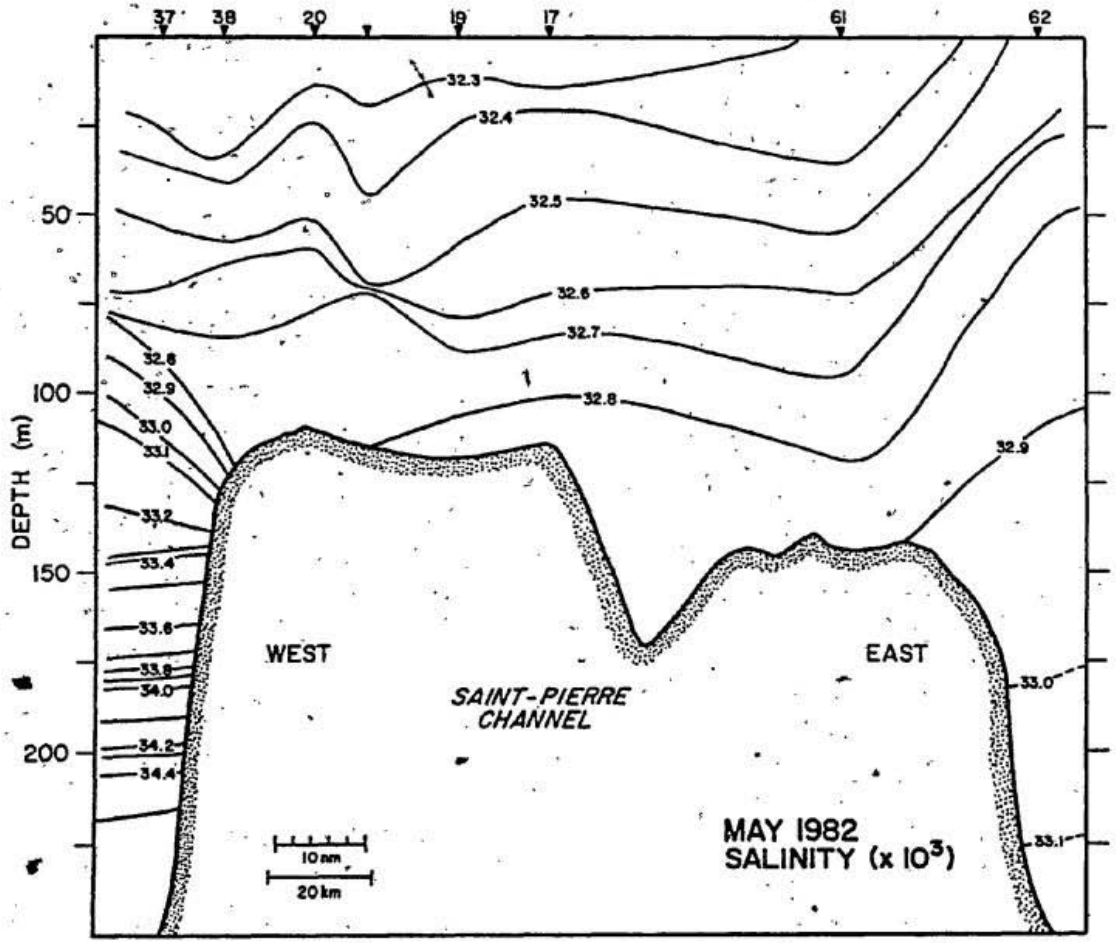


Figure A2.14 Salinity along Saint-Pierre Channel, May 1982.

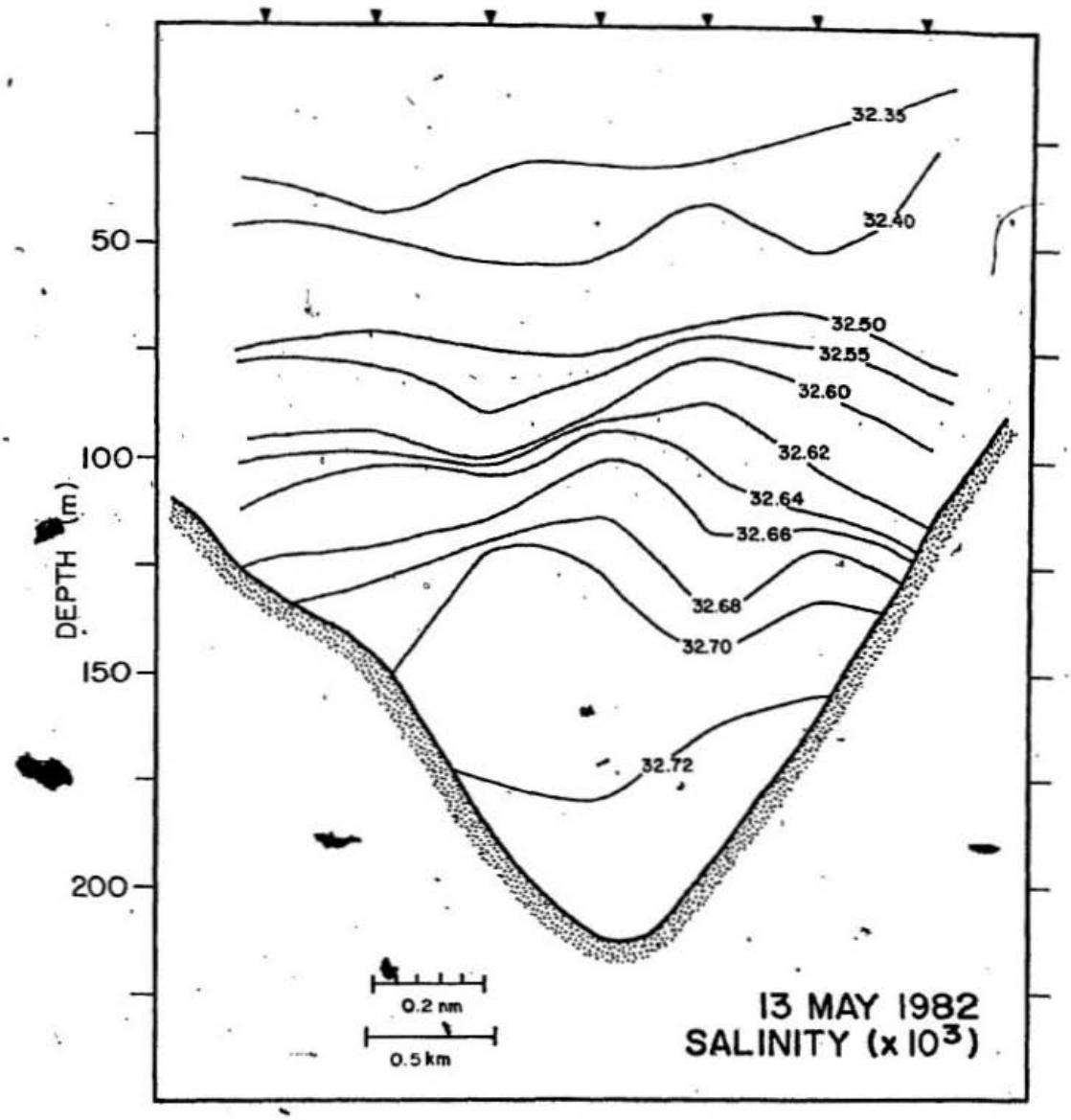


Figure A2.15 Salinity along transect T3 looking into the bay, 13 May 1982.

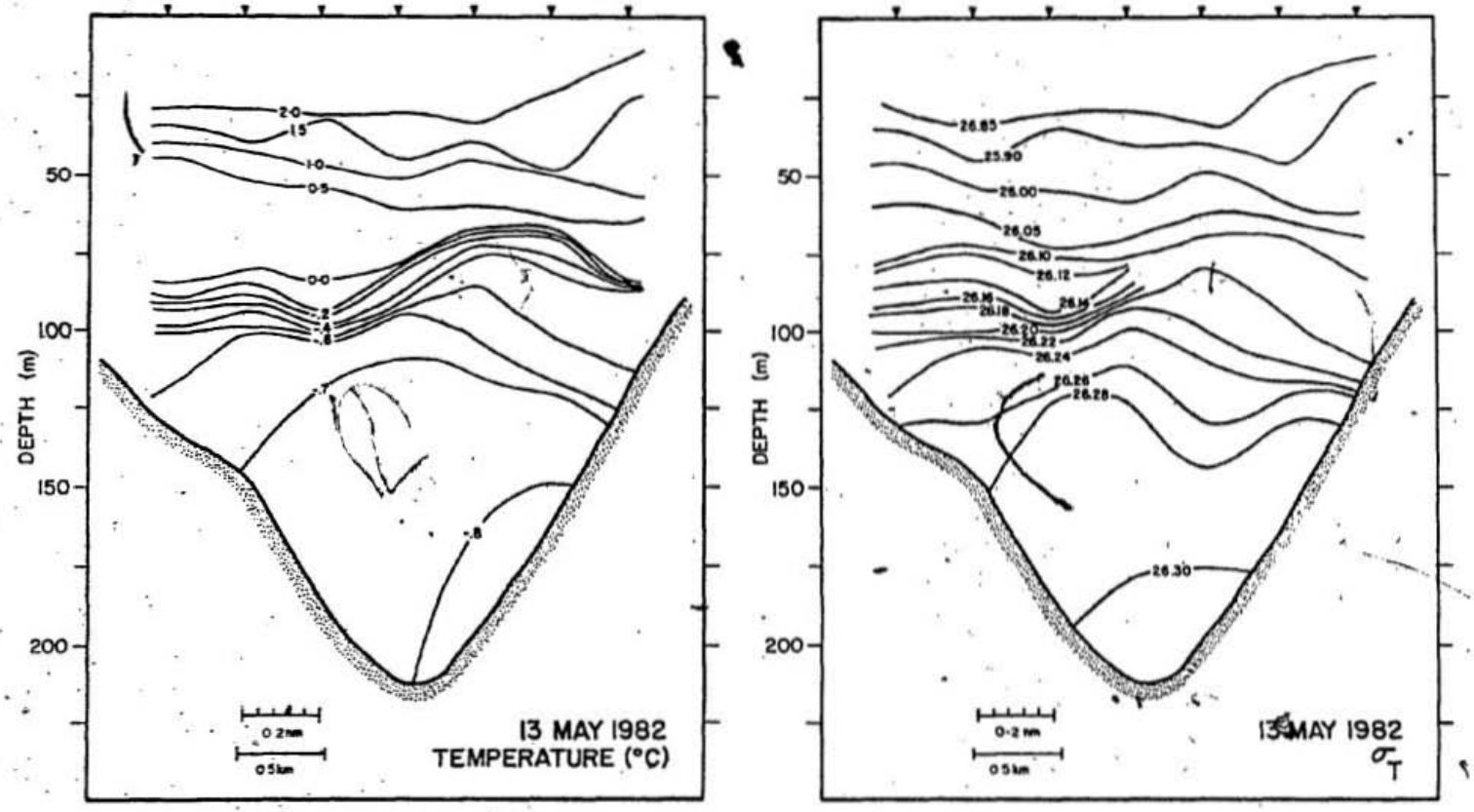


Figure A2.16 Temperature and density along T2 looking into the bay, June, 1982.

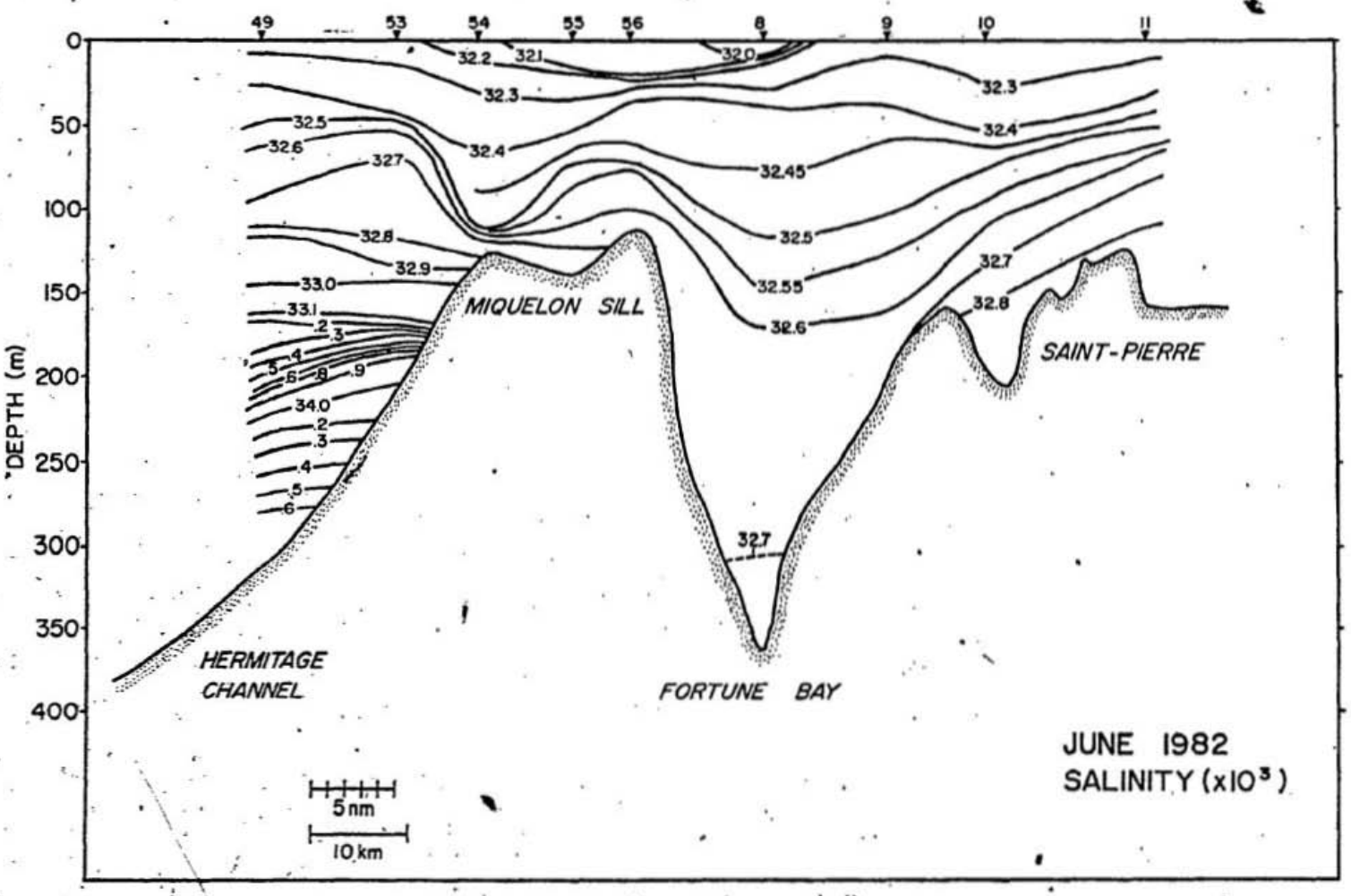


Figure A2.17 Salinity from Saint-Pierre to Hermitage Channel, May 1982.

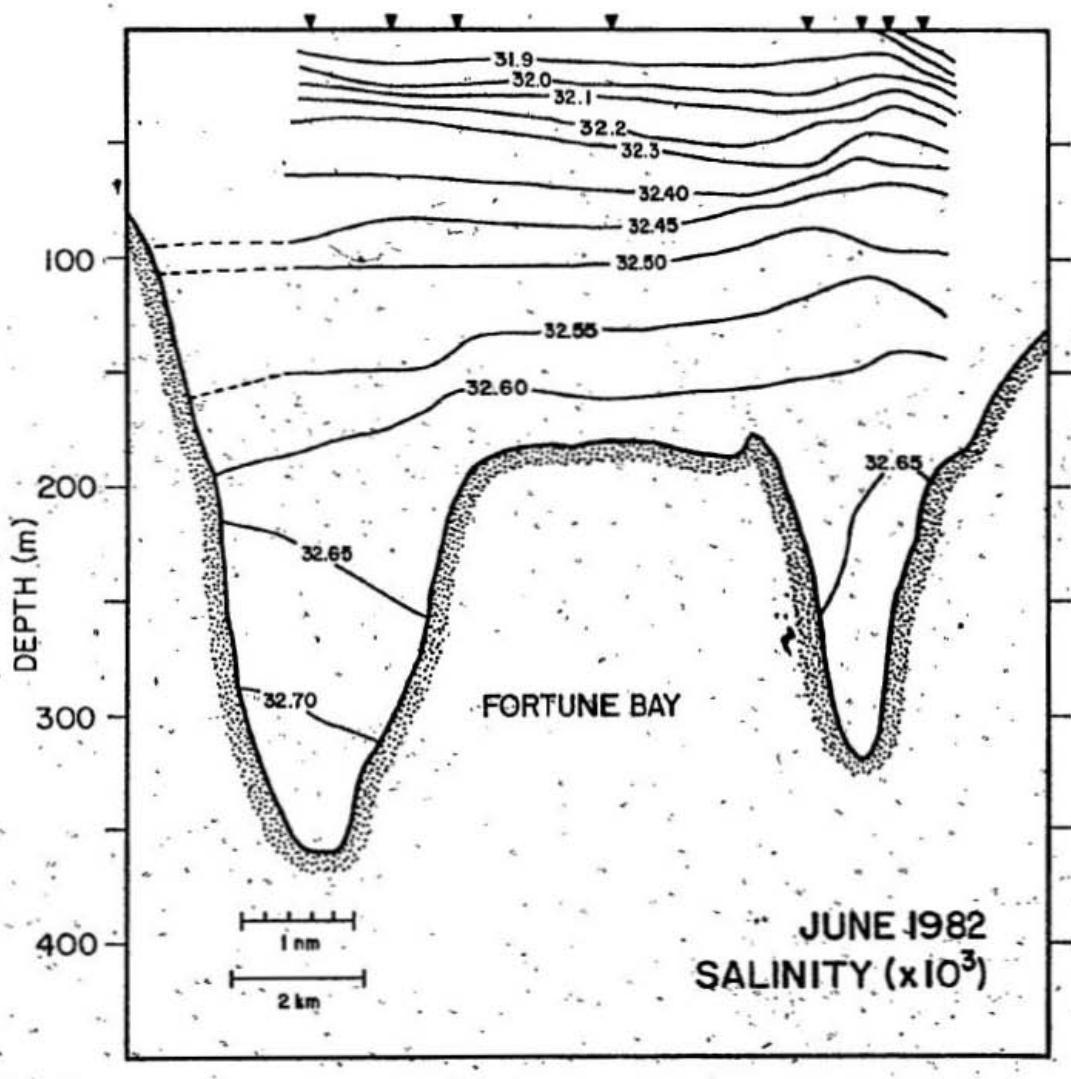


Figure A2:18 Salinity along T1 looking up the bay, 7 June 1982.

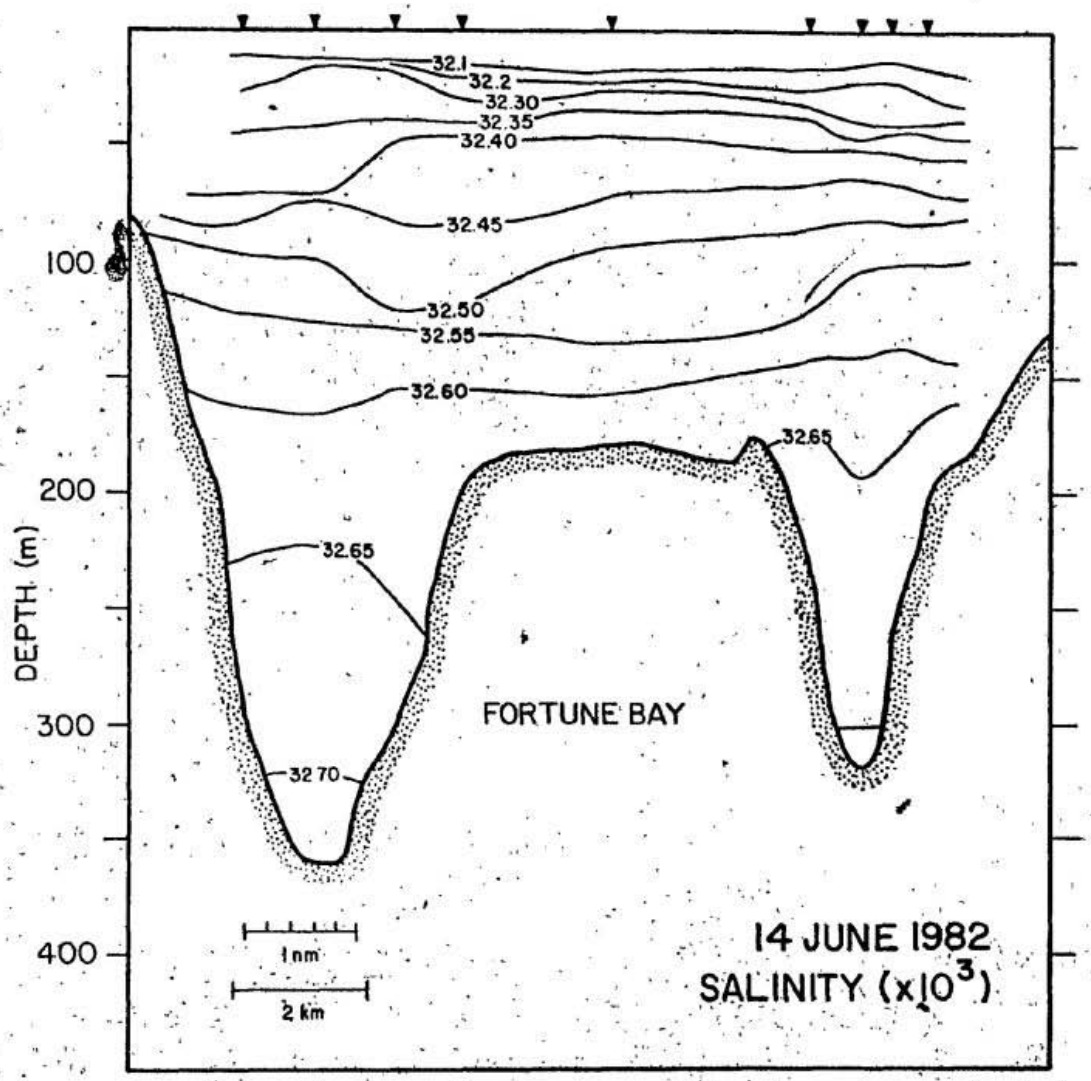


Figure A2.19 Salinity along T1 looking up the bay, 14 June 1982.

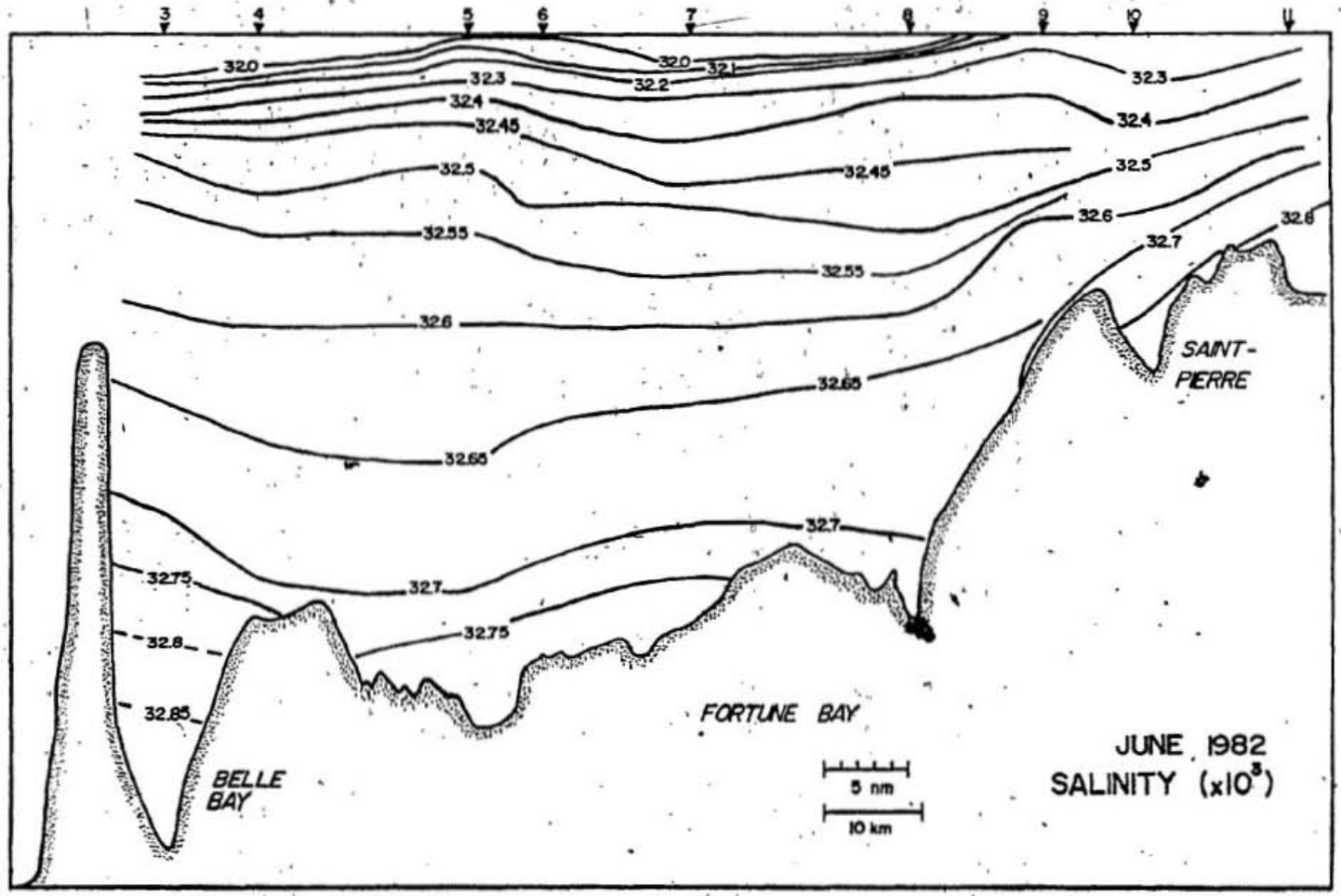


Figure A2.20 Salinity along Fortune Bay, June 1982.

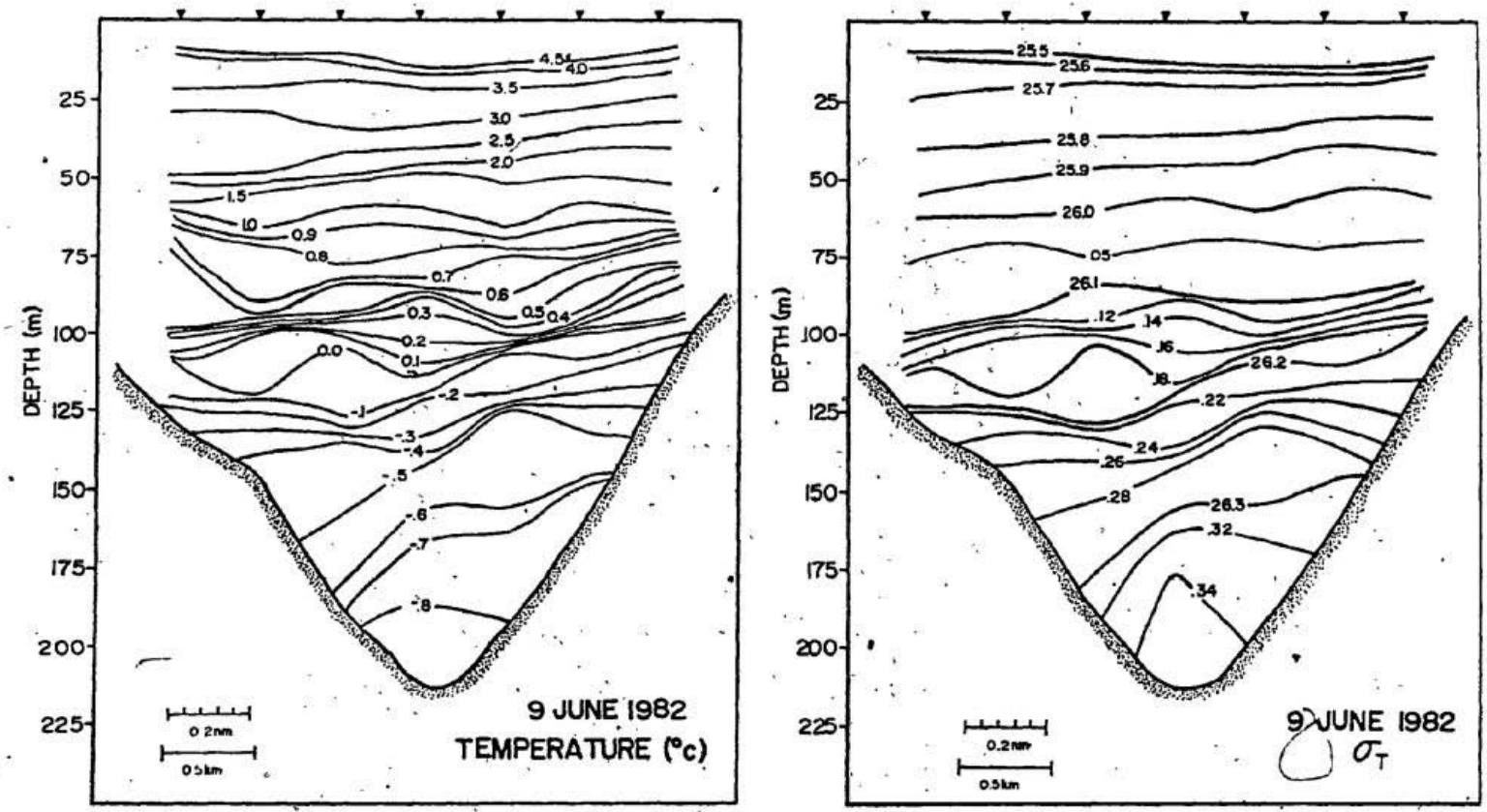


Figure A2.21 Temperature and density along T2 looking into the bay, 9 June 1982.

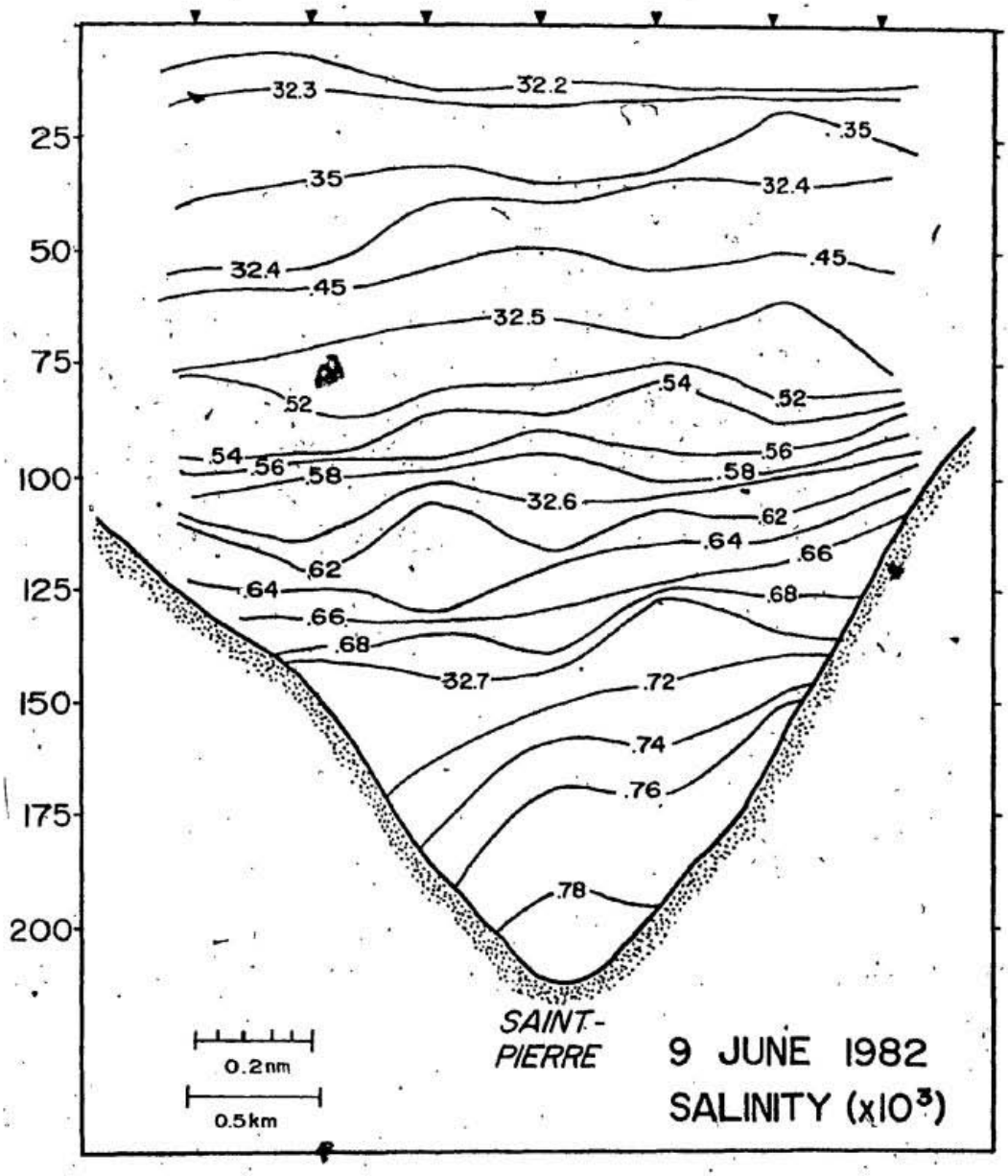


Figure A2.22 Salinity along T2 looking into the bay, 9 June 1982.

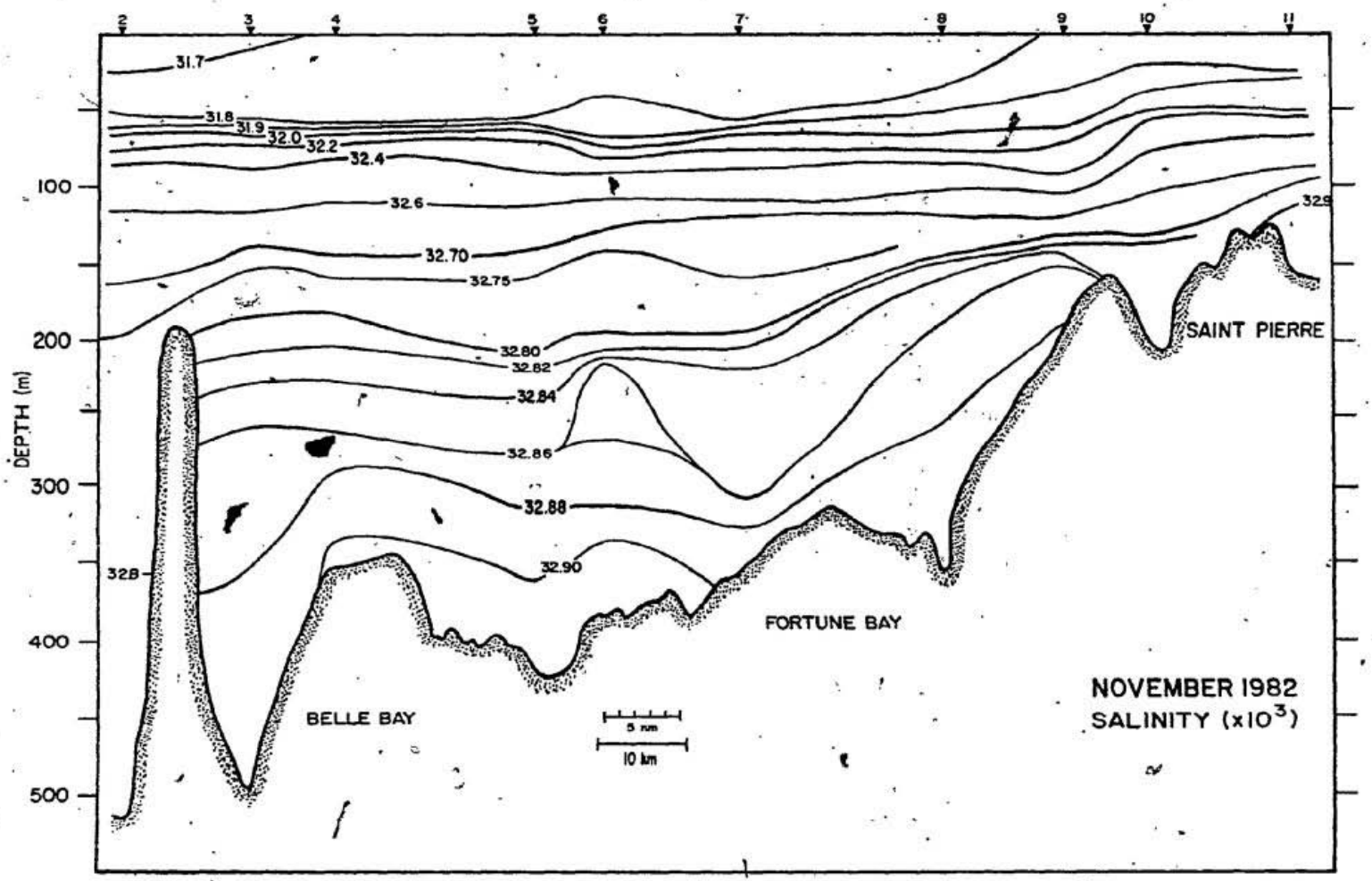


Figure A2.23 Salinity along Fortune Bay, November 1982.

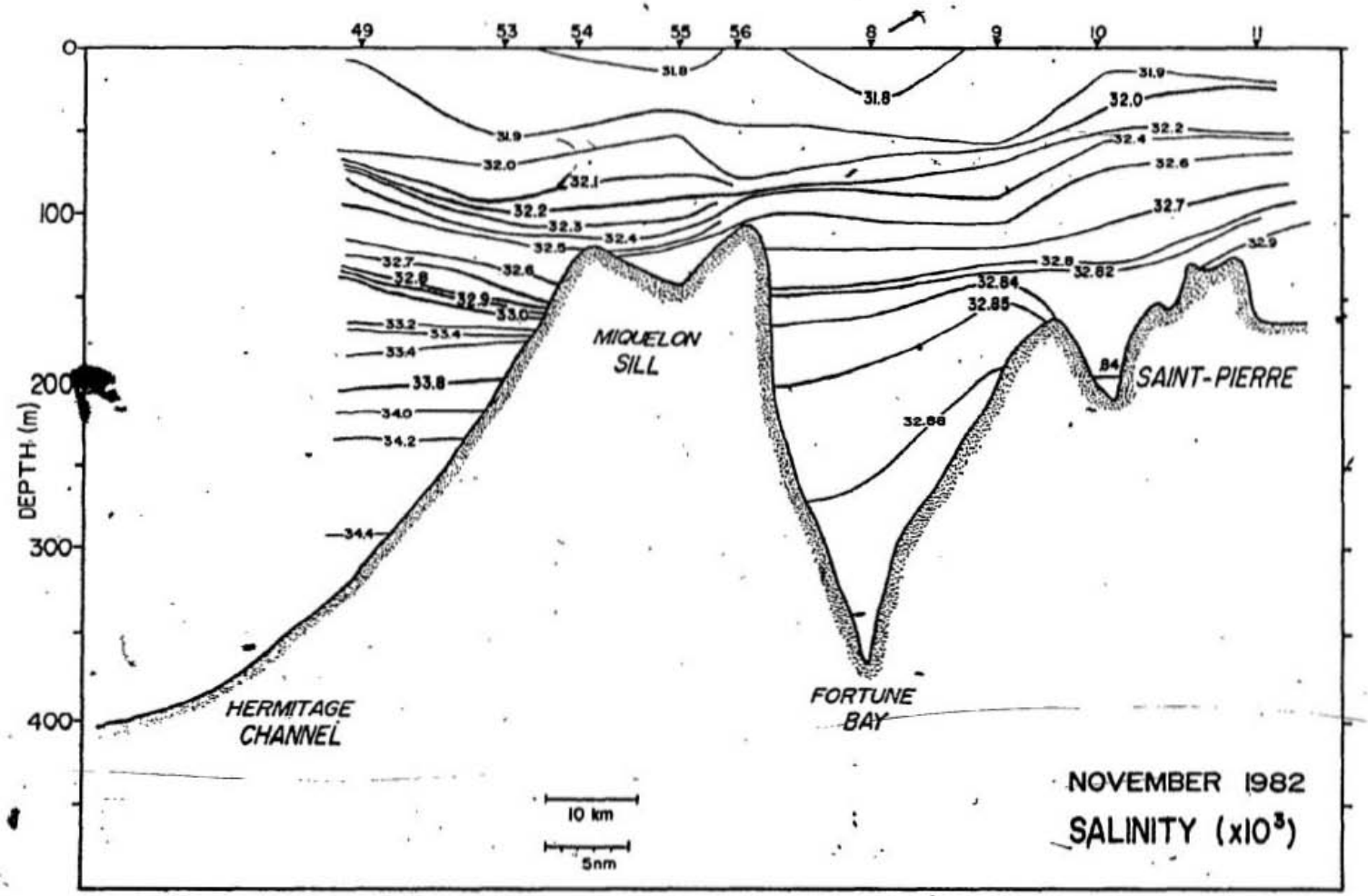


Figure A2.24 Salinity from Saint-Pierre to Hermitage Channel, November 1982.

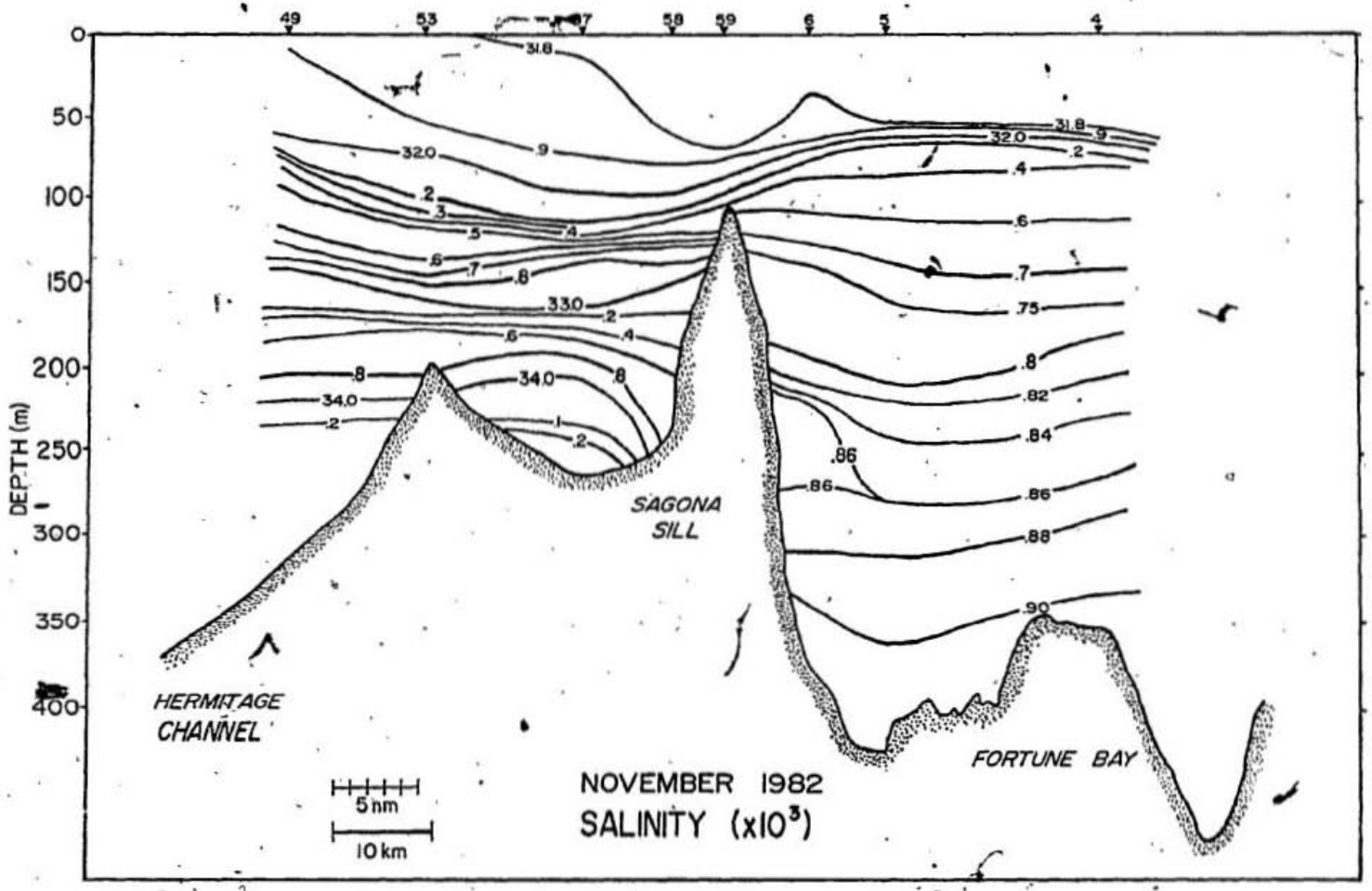


Figure A2.25 Salinity across Sagona sill, November 1982.

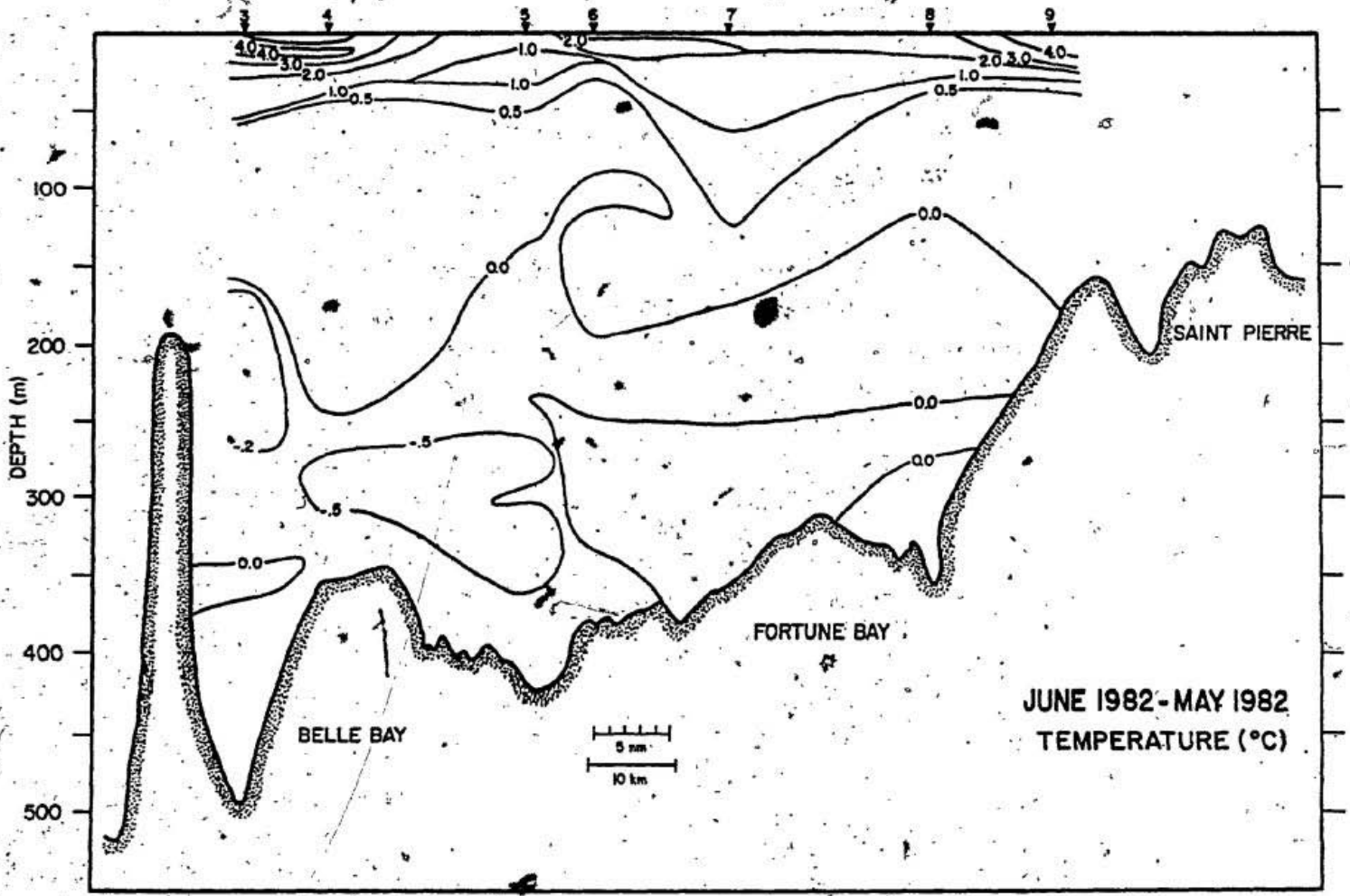
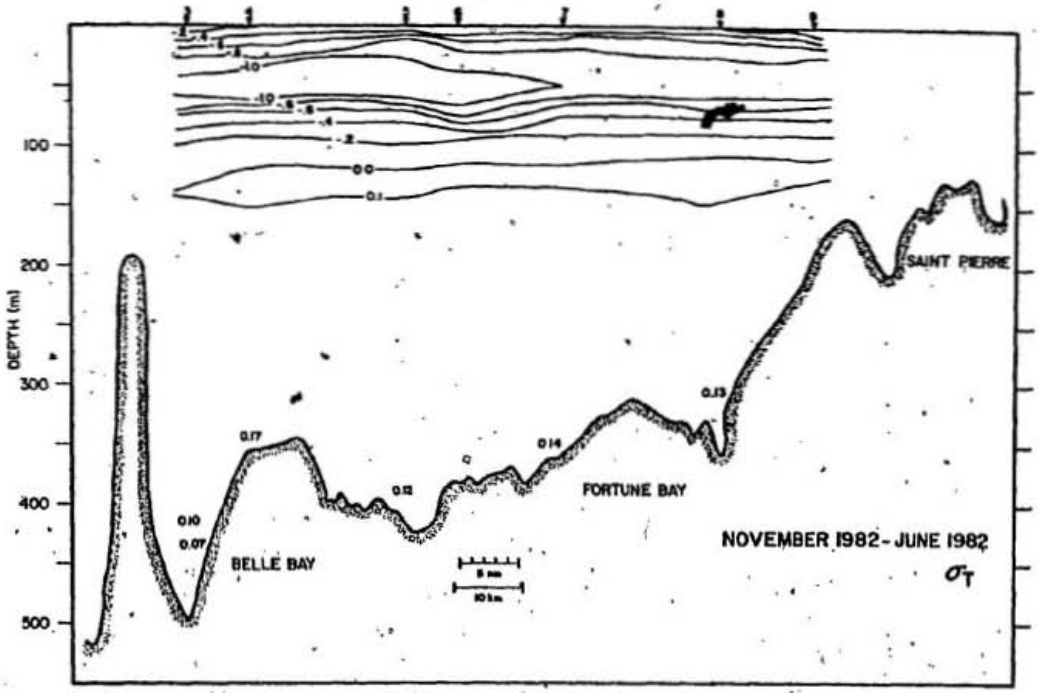


Figure A2.26 Temperature difference between May and June, in Fortune Bay; computed based upon 5m depth averages of temperatures at each station.



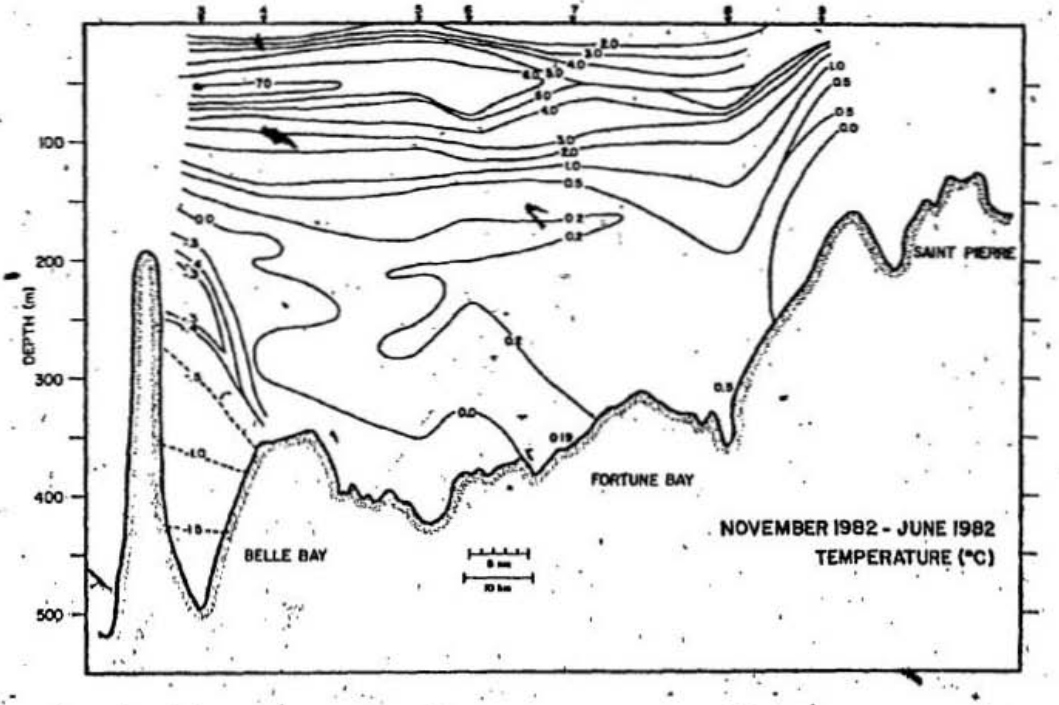


Figure A2.27 Temperature and density difference between November and June 1982, in Fortune Bay; computed based upon 5m depth averages at each station.

APPENDIX III

Along-channel variation in the Steady State Upwelling Model

In this section it will be shown that all $\frac{\partial}{\partial y}$ terms in the equations of motion presented in Section 7.3 are zero. The physical situation described here is that discussed at the start of Section 7.3. As discussed in the text, solutions should be such that $u = \frac{\partial u}{\partial x} = 0$ in the upper and lower layers. The equations to be solved in the upper layer then become:

$$(A.1) \quad fv = \frac{1}{\rho}\frac{\partial p}{\partial x}$$

$$(A.2) \quad 0 = \frac{-1}{\rho}\frac{\partial p}{\partial y} + \frac{1}{\rho}\frac{\partial \tau^y}{\partial z}$$

$$(A.3) \quad p = \rho g(\eta - z)$$

In the lower layer the equations become:

$$(A.5) \quad fv' = \frac{1}{\rho'}\frac{\partial p}{\partial x}$$

$$(A.6) \quad 0 = \frac{-1}{\rho'}\frac{\partial p'}{\partial y} + \frac{1}{\rho'}\frac{\partial \tau'^y}{\partial z}$$

$$(A.7) \quad p' = \rho g(\eta + h - \eta') + \rho' g\,(\eta' - h - z)$$

These equations can be vertically integrated, noting that $w(-H) = 0$ (where H is the total depth). The variables used are the same as those discussed in sections 7.2 and 7.3. The upper and lower layer equations become:

$$(A.9) \quad f\bar{v} = g\frac{\partial \eta}{\partial x}$$

$$(A.10) \quad 0 = -g\frac{\partial \eta}{\partial y} + \frac{(\tau_o^y - \tau_i^y)}{\rho(h + \eta - \eta')}$$

$$(A.11) \quad \frac{\partial}{\partial y}\left((h + \eta - \eta')\bar{v}\right) = 0$$

$$(A.12) \quad f\bar{v}' = g\frac{\partial \eta}{\partial x} + g'\frac{\partial \eta'}{\partial x}$$

$$(A.13)\quad 0 = -g\frac{\partial \eta}{\partial y} - g'\frac{\partial \eta'}{\partial y} + \frac{(\tau'^{y}_{i} - \tau'^{y}_{b})}{\rho'(h' + \eta')}$$

$$(A.14)\quad \frac{\partial}{\partial y}\left((h' + \eta')\,\overline{v'}\right) = 0$$

Here g' is the reduced gravitational acceleration $= \frac{\rho' - \rho}{\rho} g$, τ^{y}_{o} is the wind stress, τ^{y}_{i} is the interfacial stress, τ^{y}_{b} is the bottom stress, and $\bar{v}$ and $\overline{v'}$ are vertically averaged velocities.

By analogy with Gill's (1982, pp. 394-398) treatment of a storm surge along an infinite coastline, it is expected that the wind, blowing for a sufficiently long period of time, will generate a constant slope across the channel. The response of the interface will be similar but of opposite sign. It is thus expected that v and v' will be uniform across the channel and that $\frac{\partial \eta}{\partial x}$ and $\frac{\partial \eta'}{\partial x}$ will be independent of x, though, possibly still dependent on y. The x-derivative of (A.10) into (A.11) gives:

$$(A.15)\quad \frac{\partial^2 \eta}{\partial x \partial y}(h + \eta - \eta') + \frac{\partial \eta}{\partial y}\left(\frac{\partial \eta}{\partial x} - \frac{\partial \eta'}{\partial x}\right) = 0$$

Insertion of equation (A.10) into (A.11) gives:

$$(A.16)\quad \left(\frac{\partial \eta}{\partial y} - \frac{\partial \eta'}{\partial y}\right)\frac{\partial \eta}{\partial x} + (h + \eta - \eta')\frac{\partial^2 \eta}{\partial x \partial y} = 0$$

Upon similar treatment the lower layer equations (A.13) and (A.14) become:

$$(A.17)\quad \left(\frac{\partial^2 \eta}{\partial x \partial y} + \frac{\Delta\rho}{\rho}\frac{\partial^2 \eta'}{\partial x \partial y}\right)(h' + \eta') + \left(\frac{\partial \eta}{\partial y} + \frac{\Delta\rho}{\rho}\frac{\partial \eta'}{y}\right)\frac{\partial \eta'}{\partial x} = 0$$

$$(A.18)\quad \left(\frac{\partial \eta'}{\partial y}\right)\left(\frac{\partial \eta}{\partial x} + \frac{\Delta\rho}{\rho}\frac{\partial \eta'}{\partial x}\right) + (h' + \eta')\left(\frac{\partial^2 \eta}{\partial x \partial y} + \frac{\Delta\rho}{\rho}\frac{\partial^2 \eta'}{\partial x \partial y}\right) = 0$$

Equations (A.15) and (A.16) can be combined to give:

$$(A.20)\quad \frac{\partial \eta}{\partial x}\frac{\partial \eta'}{\partial y} - \frac{\partial \eta}{\partial y}\frac{\partial \eta'}{\partial x} = 0$$

Recalling that $\frac{\partial \eta}{\partial x}$ and $\frac{\partial \eta'}{\partial x}$ are constant it is now possible to write:

$$(A.21)\quad \eta(x,y) = a(y)x + b(y)$$

$$(A.22)\quad \eta'(x,y) = a'(y)x + b'(y)$$

Explicitly allowing y-dependence of η and η' it will now be shown that $\frac{\partial}{\partial y}$ of these terms is zero.

Substitution of equations (A.22) into (A.16) and (A.17) and (A.19) produces:

$$(A.23)\quad x\left(2a\frac{da}{dy} - a\frac{da'}{dy} - a'\frac{da}{dy}\right) + \left(\frac{db}{dy} - \frac{db'}{dy}\right)a + (h + b - b')\frac{da}{dy} = 0$$

$$(A.24)\quad 2xa'\left(\frac{da}{dy} + \frac{\Delta\rho}{\rho}\frac{da'}{dy}\right) + (h' + b')\left(\frac{da}{dy} + \frac{\Delta\rho}{\rho}\frac{da'}{dy}\right) + a'\left(\frac{db}{dy} + \frac{\Delta\rho}{\rho}\frac{db'}{dy}\right) = 0$$

$$(A.25)\quad x\left(a\frac{da'}{dy} - a'\frac{da}{dy}\right) + a\frac{db'}{dy} - a'\frac{db}{dy} = 0$$

But these equations must hold for all x so all terms for which x is common in equations (A.23), (A.24) and (A.25) must vanish identically.

Noting this, allows the following equations to be written:

$$(A.26)\quad 2a\frac{da}{dy} - a\frac{da'}{dy} - a'\frac{da}{dy} = 0$$

$$(A.27)\quad \frac{da}{dy} + \frac{\Delta\rho}{\rho}\frac{da'}{dy} = 0$$

$$(A.28)\quad a\frac{da'}{dy} - a'\frac{da}{dy} = 0$$

Combining (A.26) and (A.28) gives:

$$(A.29)\quad \frac{da}{dy} - \frac{da'}{dy} = 0$$

For both equations (A.27) and (A.29) to be satisfied then $\frac{da}{dy} = \frac{da'}{dy} = 0$.

This means that equations (A.23), (A.24) and (A.25) become:

$$(A.30)\quad \frac{db}{dy} - \frac{db'}{dy} = 0$$

$$(A.31)\quad \frac{db}{dy} + \frac{\Delta\rho}{\rho}\frac{db'}{dy} = 0$$

$$(A.32)\quad a\frac{db'}{dy} - a'\frac{db}{dy} = 0$$

Again this implies $\frac{db}{dy} = \frac{db'}{dy} = 0$, as before for a. This, therefore, shows that there is no pressure gradient in the y-direction in the channel based upon the assumptions that there is no variation in $\frac{\partial}{\partial x}$ and that steady-state conditions hold.